Error Calibration on Five-axis Machine Tools by Relative Displacement Measurement between Spindle and Work Table

2012

Cefu Hong

Table of Contents

Chapter 1
Introduction

1.1 Direct and indirect measurement of error motions of machine tools

Machine tools with two rotary axes to tilt and rotate a tool with respect to a workpiece, in addition to three orthogonal linear axes, are collectively called *five-axis machine tools*. As a typical example of five-axis machine tool configuration in today's market, a tilting-rotary table type five-axis machine tool is shown in Fig. 2-5 in Section 2.3.1.2.

A five-axis machine tool is typically used in machining components with sculptured surface, such as an impeller, where it is indispensible to continuously change the tool orientation to the workpiece to generate the designed surface. A five-axis machine tool is also often used when conducting multi-surface machining, since the chuck of a workpiece could be simplified as it owns the ability to change the relative orientation between a tool and the workpiece, which potentially reduces non-cutting time and set-up time. Other potential advantage with the five-axis machining includes shorter tool extension, which reduces the tool deflection (in three-axis machining, a tool extension must be sometimes longer to avoid unintended interference to the workpiece). The introduction of five-axis machine tools could potentially lead to cost down, and higher efficiency for a machining workshop.

With an increasing need for machining components with geometric complexity in a high efficiency, five-axis machine tools are extensively used in various manufacturing applications requiring higher machining accuracy, e.g. die and mold making. However, the increased number of the controlled axes makes it more difficult to mechanically adjust the alignment of each axis. For example, it is a common practice for machine tool builders to mechanically adjust the squareness of two linear axes by modifying the alignment of mechanical parts, e.g. guide ways on the machine bed. It is often more difficult and

time-consuming, or sometimes not possible without re-machining structural parts, to mechanically adjust the squareness of an axis of rotation to a linear axis. Furthermore, error motions of each axis accumulate as the positioning error of the tool. For these reasons, it is generally harder to achieve higher accuracy on a five-axis machine tool compared to conventional three-axis machine tools. The improvement of their motion accuracies is a crucial demand in the market [Veldhuis, 1995, Khan, 2010]. Note that the term "*error motion*" is defined in ISO 230-7:2006 [ISO 230-7, 2006] as "unintended relative displacement in the sensitive direction between the tool and the workpiece".

The *geometric error* is defined as a change in the geometry of the machine's components present in the machine's structural loop from the nominal [Schwenke, 2008]. Note that a *structural loop* of a machine tool is defined as an assembly of mechanical components which maintain a relative position between the tool and the workpiece table. To improve the machine's overall accuracy, it is clearly crucial to first measure geometric errors of each axis.

In [Schwenke, 2008], measurement methodologies to detect geometric errors in machines are distinguished between *direct* and *indirect* methods. The *direct measurement* of geometric errors represents the analysis of single errors, such as linear positioning errors, straightness errors, and angular errors of each axis. For example, the linear positioning error of a linear axis is typically measured by using a laser interferometer [ISO 230-2, 2006]. One setup of this measurement measures only the linear positioning error of a single axis, while minimizing the influence of other error motions. A key is to set up the measuring instrument such that only the target error motion influences measurement results.

Many measurement methodologies accepted by machine tool builders are direct measurement [Sartori, 1995]. While it is easier to ensure the measurement accuracy of direct measurement, the efficiency of the direct measurement can be a critical issue. For example, for orthogonal three-axis machines, 3 linear displacement errors, 6 straightness errors, 3 squareness errors, and 6 angular errors must be measured by different setups to construct the machine's kinematic model (see Section 2.3 for further details).

On the other hand, the *indirect measurement* focuses on the tool tip location as the superposition of these single errors. A typical example of the indirect measurement is the circular test using the double ball bar (DBB) described in ISO 230-4 [ISO 230-4, 2005], as shown in Fig. 1-1. In the circular test, measured error profiles are influenced by many error motions of two linear axes, e.g. positioning errors, straightness errors of each axis, and the squareness error of two axes. By best-fitting the machine's kinematic model such that its simulated TCP (tool center position) trajectories coincide with measured trajectories, one can estimate many error motions by a single circular test [Kakino, 1993]. This example illustrates a strong advantage for indirect measurements.

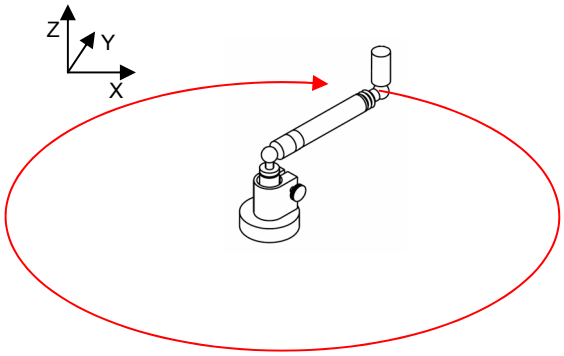

Fig. 1-1 Circular test in XY plane with the DBB (Double Ball Bar): X, Y-axes are commanded a circular interpolation, centered at the nominal ball position attached on the table. The change in the length of the telescoping bar connecting both balls is measured by a linear encoder installed in it. The contouring error motion of XY-axes in a circular can be measured.

For rotary axes in five-axis machine tools, many direct measurement methodologies are described in ISO 230-1 [ISO 230-1, 1996] and ISO 230-7 [ISO 230-7, 2006], and are also widely done by machine tool builders. For example, the measurement of angular positioning accuracy of a rotary axis by using an autocollimator and a reference polygon (or a reference indexing table) is one of direct measurements typically done by many machine tool builders.

However, these direct measurement methodologies only evaluate error

motions of a single rotary axis. When multiple rotary axes stacked to each other, it is in practice important to evaluate *how error motions of one axis changes with the rotation of the other axis*. It is difficult to apply direct measurements to such evaluation, since it requires many setup changes, and thus significant measuring time, effort, and cost.

The objective of this thesis is to propose an indirect measurement methodology to evaluate error motions of multiple rotary axes in five-axis machine tools.

1.2 Previous studies for indirect measurement for rotary axis

Recently, there have been many recent research works on the indirect measurement of geometric errors of rotary axes in the five-axis kinematics. This thesis studies the application of one of these approaches, the R-test, to the indirect measurement of a large class of error motions. To clarify the original contribution of this thesis, this subsection briefly reviews previous research works.

(1) DBB (double ball bar)

The DBB is a length measuring device to measure the distance between two spheres by using a linear encoder installed inside a telescoping bar connecting them, as shown in Fig. 1-1. As was discussed in the previous subsection, the circular test for linear axes by using the DBB is described in ISO 230-4 [ISO 230-4, 2005] and is widely accepted by machine tool builders. Many research efforts have been reported on its extension to calibrate location errors of rotary axes [Kakino, 1994, Sakamoto, 1997, Mahbubur, 1997, Abbaszaheh-Mir, 2002, Tsutsumi, 2003, Li, 2003, Zargarbashi, 2006, Lei, 2007, Uddin, 2009, Ibaraki(2), 2010]. ISO/TC39/SC2 has been lately discussing the inclusion of DBB in the revision of ISO 10791-6 [ISO/CD 10791-6, 2011].

For example, Fig. 1-2 illustrates a ball bar test described in BK2 of ISO/CD 10791-6 [ISO/CD 10791-6, 2011]. When there exists a squareness error of the C-axis average line to the X-axis average line, the measured displacement

profile in a polar plot (with respect to C-axis angular position) is shifted to the X-direction, as shown in Fig. 1-1(b).

A potentially critical issue with such a DBB-based approach is in its efficiency [Ibaraki(2), 2010]. Since the ball bar measurement is one-dimensional, it often requires at least a couple of different setups to identify all location errors (see Section 1.3 for the term "location errors"). It requires an experienced operator to be always with the measurement, and thus its full automation is difficult.

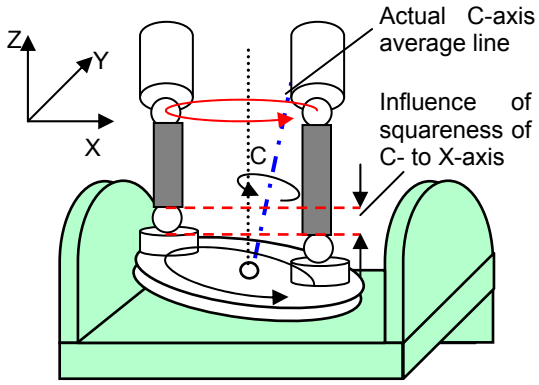

(a) Schematic of a ball bar test

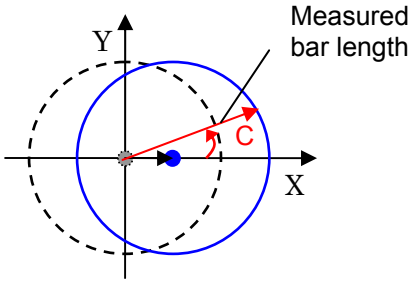

(b) Polar plot of the measured bar length with respect to C-axis angular position

Fig. 1-2 A ball bar test to calibrate the orientation of C-axis average line [Ibaraki, 2012].

(2) R-test

Weikert [Weikert, 2004], Bringmann and Knapp [Bringmann, 2006] presented the "R-Test", where the three-dimensional displacement of a sphere attached to the spindle is measured by three (or four in [Weikert, 2004, Bringmann, 2006]) linear displacement sensors installed on the table. While the

ball bar measures the sphere displacement only in one direction (i.e. the bar direction), the R-test measures a three-dimensional error trajectory in an automated measurement cycle. ISO TC39/SC2 has been also discussing the inclusion of R-test in the revision of ISO 10791-6 [ISO/CD 10791-6, 2011]. Commercial R-test devices are now available from IBS Precision Engineering [IBS] and Fidia [Fidia]. A similar measurement device composed of capacitance sensors, called "Capball", is proposed in [Zargarbashi, 2009].

In this thesis, we employ the R-test and study the extension of its application. More details on the R-test device itself will be presented in Chapter 2 and later.

(3) Probing of artifact

In recent years, high-accuracy touch-trigger probes for machine tools, are available in today's market (e.g. [Renishaw, Heidenhain]). From its nature, such a probe has a good communication capability with a CNC system, which potentially facilitates the automation of error calibration and compensation. Many tests by (1) the ball bar and (2) the R-test can be done by using such a probe, when the tests are quasi-static. ISO 10360-3:2000 [ISO 10360-3, 2000] describes such a test for CMMs with a rotary table as the fourth axis. Probing-based calibration of offset errors of rotary axis average line can be done in some commercial CNCs [US Patent, 2007, Yamamoto(3), 2011]. Its extension to a set of location errors of rotary axes has been reported in the literature [Erkan, 2010, Erkan, 2011, Iritani, 2010, Matsushita, 2010]. (see Section 1.3 for the term "location errors")

(4) Machining tests

The NAS (National Aerospace Standard) 979 [NAS 979, 1969] describes a five-axis machining test of a cone frustum, which is widely accepted as a final performance test by machine tool builders. Its inclusion in ISO/CD 10791-7:2011 [ISO/CD 10701-7, 2011] is currently under discussion at ISO TC39/SC2. Some researchers in the literature [Bossoni, 2007, Yumiza, 2007, Matsushita, 2008,

Matsushita, 2011, Hong, 2011] have analyzed the sensitivity of location errors of rotary axes on the geometric accuracy of the machined cone frustum workpice. However, it is generally not possible to separately identify each location error by a single cone frustum machining test [Matsushita, 2011]. In other words, these research works clarified that a single cone frustum machining test cannot be used as an indirect method to calibrate all location errors.

Some researchers [Ibaraki(1), 2010, Yamamoto(1), 2011, Yamamoto(2), 2011] have presented new machining tests as an indirect measurement of the machine's geometric error parameters.

(5) Laser tracker

The tracking interferometer (the term in [ISO/FDIS 230-1, 2011]), or the laser tracker, is a laser interferometer with a steering mechanism to change the laser beam direction to track a target retroreflector (typically a cat's eye [Takatsuji, 1999]) [Lau, 1986, Kohama, 2008, Schwenke, 2005, Yano, 2006, Schwenke, 2009, Takeuchi, 2010]. Unlike many other indirect schemes reviewed in this subsection, the tracking interferometer can potentially be applied to direct measurement of rotary axis error motions at arbitrary locations, without synchronous motion of linear axes [Schwenke, 2009]. More studies will be need.

1.3 Objective and original contribution of this thesis

As was reviewed in the previous subsection, many measurement instruments have been proposed for motion error calibration of rotary axes. While using different measuring instruments, the majority of these previous works has a common objective: to identify location errors of rotary axes. In ISO 230-7 [ISO 230-7, 2006], *location errors* of a rotary axis are defined as axis shifts of the *axis average line*, i.e. the straight line segment located with respect to the reference coordinate axes representing the mean location of the axis of rotation. In other words, location errors only represent the "average" error in the position and orientation of the axis of rotation. For example, previous works reviewed in the previous subsection on the R-test, [Weikert, 2004, Bringmann,

2006, Zargarbashi, 2009] only presented its application to the identification of location errors. In past works, reviewed in the previous subsection, ball bar tests [Kakino, 1994, Sakamoto, 1997, Mahbubur, 1997, Abbaszaheh-Mir, 2002, Tsutsumi, 2003, Li, 2003, Zargarbashi, 2006, Lei, 2007, Uddin, 2009, Ibaraki(2), 2010], probing tests [Erkan, 2010, Erkan, 2011, Iritani, 2010, Matsushita, 2010], machining tests [Ibaraki(1), 2010, Yamamoto(1), 2011, Yamamoto(2), 2011] all presented their application to location errors calibration only. Quasi-static tests for a rotary axis described in ISO 10791-1 to -3 [ISO 10791-1, 1998] also focus only on location errors.

Clearly, as is well understood by many machine tool manufacturers, location errors of rotary axes are one of the most fundamental error factors in the five-axis kinematics. From our experiences, however, many latest commercial small-sized five-axis machine tools have relatively small location errors of rotary axes due to recent technical advances in measurement and assembly adjustment schemes. In such a case, it is of more importance to observe and calibrate not only the average of error motions of a rotary axis, but also *how error motion changes with the rotation of a rotary axis*. Such an error motion as a function of the angular position of a rotary axis, is represented by "component errors" in ISO 230-7 [ISO 230-7, 2006], and is referred to as *position-dependent geometric errors* in this study.

The objective of this study is to propose an indirect measurement method to calibrate geometric errors (particularly position-dependent geometric errors) of multiple rotary axes on five-axis machine tools.

Compared to the ball bar test or touch-trigger probes, the R-test has a strong advantage in that it can measure the TCP displacement in all the three directions (X, Y, and Z directions) simultaneously. Therefore, by a single measurement cycle, the R-test can obtain significantly more "information" at various angular positions of rotary axes than other measuring instruments, without requiring setup changes. For this reason, R-test is chosen to be the measurement device in this thesis.

Compared to past researches reviewed in the previous subsection, the

original contribution of this thesis can be summarized as follows:

1. The R-test device itself was proposed in [Weikert, 2004]. Past researches on the R-test [Weikert, 2004, Bringmann, 2006, Zargarbashi, 2009] have focused on its application to the calibration of location errors of rotary axes. As will be described in details in Section 2.3, location errors are the most fundamental error motions. This thesis will present its extension to position-dependent geometric errors, or "error map", of rotary axes. Furthermore, the procedure to graphically present R-test results is also this thesis's original contribution, to help users' intuitive understanding of the machine's error motions. (Chapter 3)
2. The thermal influence can be one of dominant error factors in machine tool motion accuracies. As will be discussed in detail in Section 4.1, conventional thermal tests for machine tools in ISO standards only evaluate thermal influence on the positioning accuracy. This thesis will present a new test method to evaluate thermal influence on error motions of rotary axes by applying the R-test. (Chapter 4)
3. In all past R-test researches, the R-test device use contact-type linear displacement sensors with a flat-ended probe. For more accurate dynamic measurement, and safer measurement, this thesis will propose a non-contact type R-test with laser displacement sensors. It significantly complicates the algorithm to calculate the sphere displacement. This thesis will propose an algorithm to calculate it for the non-contact type R-test. (Chapter 5)
4. Past researches can be found on the analysis of the influence of the machine's error motions on the machining accuracy. For example, for the cone frustum machining test described in NAS979 standard [NAS 979, 1969], researchers [Yumiza, 2007, Matsushita, 2008, Uddin, 2009] analyzed how location errors of rotary axes affect the machining accuracy of the test piece. These past researches are, however, limited to location errors only. This thesis will present a numerical analysis of geometric errors (especially position-dependent geometric errors) of rotary axes on machining accuracy. (Chapter 6)

Chapter 2
R-test device and kinematic model of five-axis controlled machine tools

2.1 Introduction

As was reviewed in Section 1.2-(2), the R-test device itself was proposed by Weikert [Weikert, 2004] and its development is not a part of this thesis's original contribution. This chapter will first review the conventional contact-type R-test device itself, as well as its computation algorithm to measure the sphere displacement (Section 2.2).

Then, the last half of this chapter (Section 2.3) will review the kinematic model for a five-axis machine tool, as well as geometric error parameters included in it. The objective of the indirect measurement presented in this thesis is to identify the kinematic model from a set of measured TCP profiles measured by the R-test. The machine tool kinematic model is thus the fundamental of this thesis.

2.2 Contact-type R-test device

2.2.1 Measuring principle of contact-type R-test measuring instrument

Figure 2-1 shows the schematics of the conventional contact-type R-test device used in this study ([Weikert, 2004, Bringmann, 2006, Zargarbashi, 2009, Ibaraki, 2011]). A ceramic precision sphere of the radius R is attached to a machine spindle. Three contact-type linear displacement sensors with a flat-ended probe are attached on a fixture (named by "sensors nest") that is fixed on a rotary table. Using the pre-calibrated direction vector of each displacement sensor, the displacements of the three probes can be directly transferred to the displacement of the sphere center. More detailed algorithm to measure the sphere center displacement will follow.

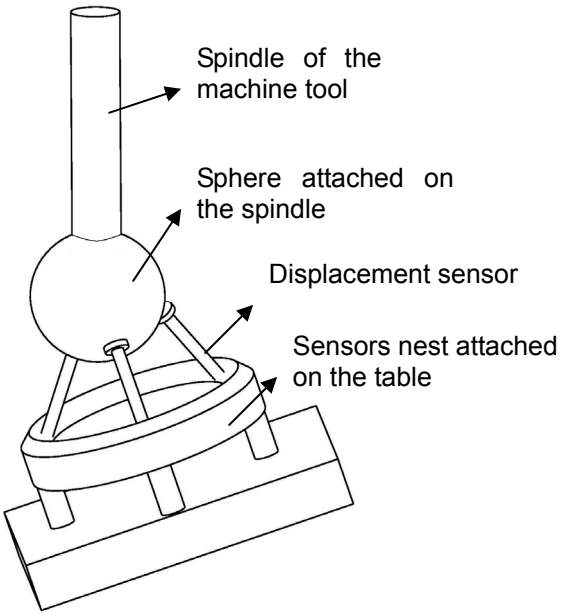

Fig. 2-1 Schematics of the R-test device.

2.2.2 Procedure to measure three-dimensional displacement by contact-type R-test

(1) Basic relationship of sphere displacement and sensor outputs

The relationship of sphere displacement and sensor outputs with contact-type R-test was presented in [Bringmann, 2007, Ibaraki, 2009, Oyama, 2009]. As the fundamental in this thesis, it will be briefly reviewed in this subsection.

To transfer the displacements measured with three linear displacement sensors to the three-dimensional displacement of the sphere center, the unit direction vectors of three probes, denoted by $V_i = (u_i, v_i, w_i)^T$ (i = 1, 2, 3), are necessary. Figure 2-2 shows the relation between the displacement of sphere center and the i-th sensor displacement. The origin of the coordinate system, $O_0 = (0, 0, 0)^T$, is defined at the sphere center in its initial position; the orientation of the coordinate system is defined based on the machine coordinate system [Schwenke, 2008]. When the sphere center is at O_0, the sphere and the i-th probe contacts at P_0. After the sphere center moves to $O_j = (x_j, y_j, z_j)^T$ (j = 1, ..., N), they contacts at P'. Denote the intersection of the line O_0P_0 and the probe surface by

P'_0. By this movement, suppose that this i-th sensor is displaced by the distance d_{ij}. The distance between O_j and $P'_0 = (P_x, P_y, P_z)^T$, the distance between P' and P'_0 (denoted by e), the displacement of the i-th sensor (denoted by d_{ij}), and the radius of the sphere, R, are related as follows:

$$\begin{cases} \left(\overline{O_j P'_0}\right)^2 = \left(P_x - x_j\right)^2 + \left(P_y - y_j\right)^2 + \left(P_z - z_j\right)^2 = R^2 + e^2 \\ d_{ij}{}^2 + e^2 = (x_j{}^2 + y_j{}^2 + z_j{}^2) \end{cases} \tag{2-1}$$

The vector $O_0 P'_0$ satisfies:

$$\begin{cases} \overline{O_0 P'_0} = [P_x, P_y, P_z]^T = (R + d_{ij})[u_i, v_i, w_i]^T \\ \left|\overline{O_0 P'_0}\right|^2 = P_x{}^2 + P_y{}^2 + P_z{}^2 = \left(R + d_{ij}\right)^2 \end{cases} \tag{2-2}$$

From Eq. (2-1) and Eq. (2-2), the following equation can be obtained:

$$x_j u_i + y_j v_i + z_j w_i = d_{ij} \tag{2-3}$$

Applying Eq. (2-3) to all the three sensors, the displacements of three sensors are related to the sphere displacement as follows:

$$\left[d_{1j}, d_{2j}, d_{3j}\right] = \left[x_j, y_j, z_j\right] \cdot \begin{bmatrix} u_1 & u_2 & u_3 \\ v_1 & v_2 & v_3 \\ w_1 & w_2 & w_3 \end{bmatrix} \tag{2-4}$$

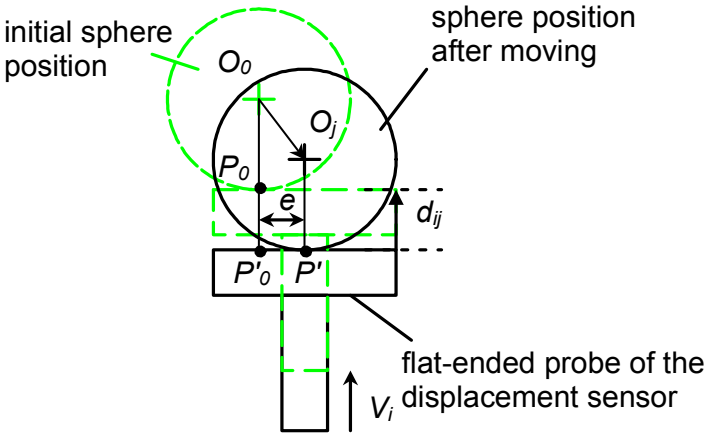

Fig. 2-2 Relation between the displacement of sphere center and the i-th sensor displacement.

(2) Calibration of unit direction vector of each sensor

To calculate the sphere displacement by the R-test, the unit direction

vector of each sensor, V_i (i = 1, 2, 3), must be pre-calibrated. In different installation of the R-test device on the machine's work table (with different orientation of the R-test device in the workpiece coordinate sysetm), direction vectors become different in the machine coordinate system. Therefore, unit direction vectors (denoted by V_i (i = 1, 2, 3)), must be calibrated with each R-test setup. Similarly as all the previous R-test works (e.g. [Weikert, 2004]), they are identified by using the machine tool's positioning as the reference. Their calibration procedure is as follows:

To calibrate the unit direction vector of each sensor, the spindle-side sphere center, denoted by (x, y, z), is commanded in this study as follows:

a. Initial position is set to be (x, y, z) = (0, 0, 0);
b. (x, y, z) = (+l, 0, 0), where $l \in \Re$;
c. (x, y, z) = (-l, 0, 0);
d. (x, y, z) = (0, 0, 0)
e. (x, y, z) = (0, +l, 0);
f. (x, y, z) = (0, -l, 0);
g. (x, y, z) = (0, 0, 0)
h. (x, y, z) = (0, 0, +l);
i. (x, y, z) = (0, 0, -l);
j. Repeat *a* to *i* by three times;
k. Command the sphere center to its initial position, (x, y, z) = (0, 0, 0).

Total 28 positions are commanded. At each commanded position (x_j, y_j, z_j) (j = 1, …, N = 28), the sphere center is stopped, and the displacement of the sensors, $[d_{1j}, d_{2j}, d_{3j}]^T$ (j = 1, …, N = 28), are logged.

In the calibration, the machine's positioning error is assumed to be sufficiently small compared to the measurement uncertainty. In typical commercial machine tools, the positioning error within the operation above is expectedly a couple of micrometers at most, when l = 1mm (as in case studies presented in this thesis). In actual R-test cycles to be presented in this thesis, the sensor displacement is usually much smaller than l = 1mm (typically several ten micrometers at most). For the measurement uncertainty proportional to the

displacement, it can be said that the influence of the machine's positioning error in the calibration procedure is negligibly small.

When the sphere center displacement, $[x_j, y_j, z_j]^{\mathrm{T}}$ (j = 1, …, N), is known, the unit direction vectors (i.e. $[u_i, v_i, w_i]^T$ (i = 1, 2, 3)) can be identified with solving the following problem by the least square method:

$$\min_{u_i, v_i, w_i} \sum_{j=1}^{N} \left\| \begin{bmatrix} d_{1j}, d_{2j}, d_{3j} \end{bmatrix} - \begin{bmatrix} x_j, y_j, z_j \end{bmatrix} \cdot \begin{bmatrix} u_1 & u_2 & u_3 \\ v_1 & v_2 & v_3 \\ w_1 & w_2 & w_3 \end{bmatrix} \right\|^2 \tag{2-5}$$

where ||*|| represents the two-norm of a vector.

(3) Measurement of three-dimensional displacements of sphere center

In R-test measurement cycles, the objective of R-test device is to measure the sphere center displacement. When displacement sensors' readouts, d_{ij} (i = 1, 2, 3), are given, the displacement of sphere center, $O_j = (x_j, y_j, z_j)^{\mathrm{T}}$ (j = 1, ..., N), can be calculated from Eq.(2-4) as follows:

$$\begin{bmatrix} x_j & y_j & z_j \end{bmatrix} = \begin{bmatrix} d_{1j} & d_{2j} & d_{3j} \end{bmatrix} \cdot \begin{bmatrix} u_1 & u_2 & u_3 \\ v_1 & v_2 & v_3 \\ w_1 & w_2 & w_3 \end{bmatrix}^{-1} \tag{2-6}$$

(4) Calibration of offset of the sphere center from rotation center of the spindle

When the precision sphere is attached to the spindle, there may be an offset of the sphere center from the axis of spindle rotation, as shown in Fig. 2-3(a). It is favorable to mechanically remove this offset by using e.g. a fixture to minutely move the sphere. Instead, in our experiments, this offset is measured by using the R-test device in the following procedure, and its influence is removed numerically:

a. After calibrating unit direction vectors of three displacement sensors with the procedure described in Section 2.2.2-(2), the spindle is rotated for more than 360°. The displacements of the sensors are logged and a profile of the sphere center displacement (x_j, y_j) (j = 1, …, N) is calculated with Eq. (2.6).

Figure 2-3(b) illustrates a trajectory of the sphere center when the spindle rotates. Due to the sphere offset from the spindle axis average line, the trajectory of the sphere center will be a circle when the spindle rotates.

b. From the measured trajectory, the center of the trajectory $P_S(p_{Sx}, p_{Sy})$ can be identified with solving the following problem by the least square method:

$$\min_{p_{sx}, p_{sy}, R_S} \sum_{j=1}^{N} \left\| \sqrt{(x_j - p_{Sx})^2 + (y_j - p_{Sy})^2} - R_S \right\|^2 \tag{2-7}$$

where R_S is the identified radius of the measured trajectory.

Since the offset of the sphere center is not the inherent error from the machine, the influence of the sphere center offset from the rotation center of spindle is numerically eliminated from the R-test measurement result. The details of the algorithm will be presented in Section 2.3.2.

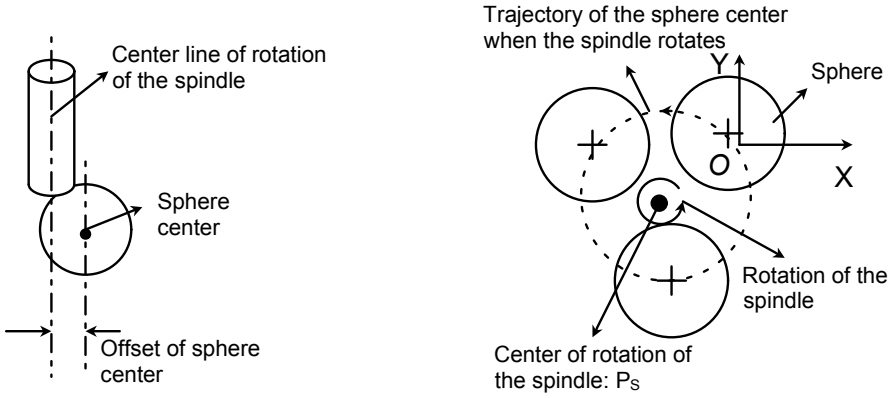

(a) Offset of the sphere center (b) Calibration of the offset

Fig. 2-3 Calibration of the sphere center offset from the rotation center of the spindle.

2.2.3 Contact-type R-test prototype developed in this study

The developed contact-type R-test prototype is shown in Fig. 2-4. A ceramic precision sphere of the diameter 25.4 mm (its major specifications are shown in Table 2-2) is attached to a machine spindle. Three contact-type linear displacement sensors with flat-ended probes (MT1281 from Heidenhain) are installed on a fixture (named by “sensors nest”) that is fixed on the table. The

main specifications of the sensors are listed in Table 2-1.

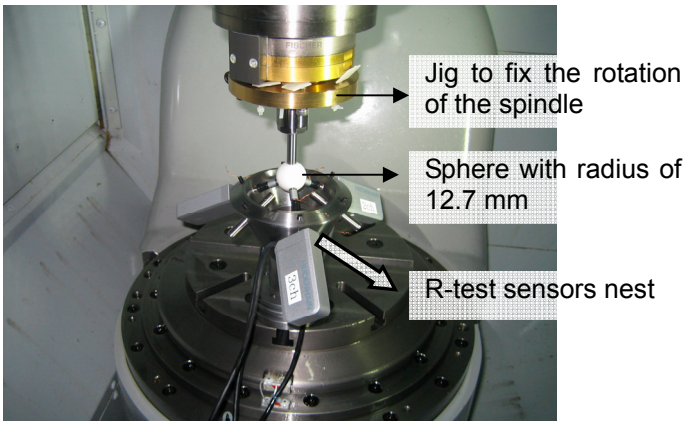

(a) External view (1)

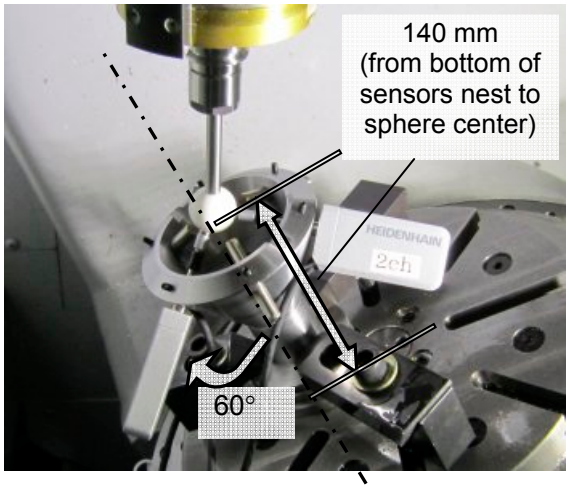

(b) External view (2)

Fig. 2-4 Contact-type R-test prototype used in this thesis.

Table 2-1 Specifications of the linear displacement sensor (MT1281 from Heidenhain).

Measuring principle	Photo-electric scanning of an incremental scale with spring-tensioned plunger
Measurement range	12 mm
System accuracy	± 0.2 μm
Gauging force (vertically upward)	0.35 to 0.6 N
Signal period	2 μm
Mechanically permissible traversing speed	30 m/min

Table 2-2 Configuration of the reference ball (from Moritex Co., Ltd)

Diameter	25.4 mm (±1.25μm)
Sphericity	1 μm
Material	AL203
Accuracy grade	AFBMA Grade 5 (with sphericity tolerance of 0.13μm)

The sphere attached on the spindle should be fixed during a five-axis measurement cycle. Throughout this study, we use a fixing jig attached between the tool holder and the spindle, as shown in Fig. 2-4(a).

The detailed analysis of R-test measurement uncertainty is ignored in this research, since it can be found in [Weikert, 2004].

2.3 Kinematic model of five-axis controlled machine tools

2.3.1 Geometric errors

2.3.1.1 Sources of geometric errors

In [Schwenke, 2008], sources of geometric errors in a machine tool are summarized. Here, its brief review will be presented.

The accuracy of machine tools is affected by many error sources. Due to a change in geometry of the structural loop components, the actual position and orientation of the representative tool center line relative to the workpiece differs from its nominal position and orientation.

The following major error sources affect the accuracy of the relative end-effected position and orientation:

(1) Kinematic errors:

Kinematic errors are errors due to imperfect geometry and dimensions of machine components as well as their configuration in the machine's structural loop, axis misalignment and static errors of the machine's measuring systems.

(2) Thermal-mechanical errors:

Thermal-mechanical errors are errors due to the presence or changing of internal and external heat/cold sources in machine tools, and very often significant expansion coefficients and expansion coefficient differences of

machine part materials. Among many error sources in machine tool kinematics, thermal-mechanical errors can be one of dominant error factors under extended usage of the machine [Ramesh, 2000, Schwenke, 2008].

(3) Dynamic errors:

Dynamic errors are errors caused by motion control, acceleration or deceleration. In the analysis, they are often distinguishable from the errors caused by other error sources by applying different feed speeds and/or accelerations for the same motion path.

This thesis will present the methodology to calibrate (1) kinematic errors (in Chapter 3), (2) thermal-mechanical errors (in Chapter 4), and (3) dynamic errors (in Chapter 5).

Other error sources, such as errors caused by machining forces or loads could be critical [Schwenke, 2008]. However, this study does not cover them.

All of these error sources influence the relative error motions between the tool and the workpiece on the machine's kinematics, and are modeled as geometric errors of the machine in this thesis.

2.3.1.2 Position-independent and position-dependent geometric errors of rotary axes

The objective of the measurement schemes to be presented in this thesis is to numerically identify geometric errors representing various error motions described above. In this thesis, geometric errors are categorized into two sub-categories, i.e. position-independent geometric errors and position-dependent geometric errors. Their definition will be given in this subsection.

(1) Machine configuration

First, this thesis considers the five-axis machine configuration with a tilting rotary table as shown in Fig. 2-5. The machine has three linear axes (X-, Y-, and Z-axis) and two rotary axes (B-, and C-axis). It must to be emphasized that the basic idea of this thesis can be straightforwardly extended to any configurations of five-axis machines.

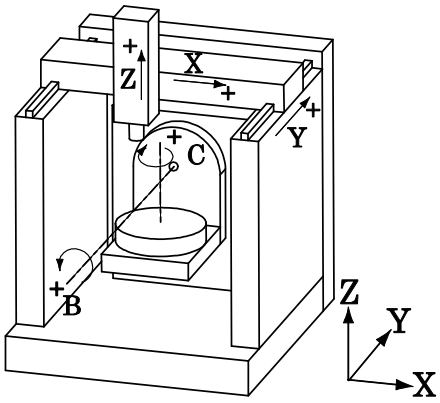

Fig. 2-5 Configuration of the five-axis machine tool considered in this study.

(2) Definition of coordinate systems

In this study, the coordinate system fixed to the machine frame or bed is called *the reference coordinate system*. The coordinate system attached to the rotary table is referred as *the workpiece coordinate system*. The origin of both coordinate systems is set to be the intersection of nominal B-axis and C-axis.

The B-coordinate system is defined as the coordinate system fixed on the B-axis. In other words, the B-coordinate system is given by rotating the reference coordinate system around its Y-axis by the nominal B-axis angular position, B^*.

(3) Position-independent geometric errors

For a rotary axis, as illustrated in Fig. 2-6, its *axis of rotation* is represented by a line with two orientation parameters and two position parameters. In ISO 230-6:2006 [ISO 230-6, 2006], the *axis average line is* defined by "a straight line segment located with respect to the reference coordinate axes representing the mean location of the axis of rotation." *Location errors* associated with this rotary axis [ISO 230-7, 2006] are defined as the position and the orientation of the axis average line of the rotary axis. In the example shown in Fig. 2-6, location errors E_{A0C} and E_{B0C} represent the tilt angle of the axis average line around the X- and Y-axis from its nominal orientation, respectively, and E_{X0C} and E_{Y0C} represent its offset in the X- and Y-direction, from its nominal position, respectively. Since location errors represent *average* orientation and position, and thus not dependent on its rotation, location errors

are sometimes called *position-independent geometric errors* in this thesis. For the machine configuration shown in Fig. 2-5, total eight location errors of rotary axes and three location errors of linear axes, shown in Table 2-3, are sufficient [Tsutsumi, 2003, Inasaki, 1997, Abbaszaheh-Mir, 2002].

Table 2-3 also presents the notation of location errors used throughout this thesis, as well as their brief description. In this thesis' notation (for example δx^0_{BY} in Table 2-3), the first (set of) characters represents the direction of deviation (δx, δy, and δz for linear deviations, and α, β, and γ for angular deviations). The first character in the subscript (the "B-axis" for δx^0_{BY}) represents the axis concerned (strictly, the coordinate system attached to this axis). The deviation is defined in reference to the coordinate system attached to the axis represented by the last character in the subscript (the "Y-axis" for δx^0_{BY}). The upper-script "0" represents location errors in this thesis.

It is to be noted that the notation in ISO 230-7 [ISO 230-7, 2006, Schwenke, 2008] defines each geometric error with respect to the single machine (reference) coordinate system. In our model, geometric errors of each axis are defined in a relative sense with respect to the axis on which it is mounted. Table 2-3 also shows the correspondence of our notation of error parameters with that in ISO/FIDS 230-1:2011 [ISO/FIDS 230-1, 2011].

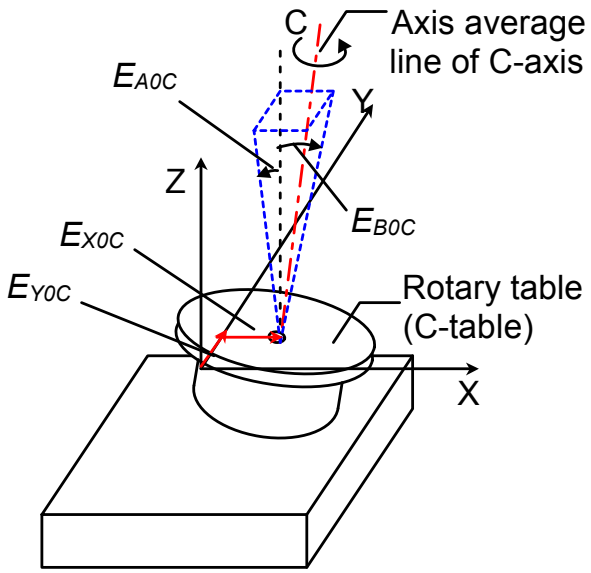

Fig. 2-6 Location errors of a rotary axis (C-axis) [ISO 230-6, 2007].

Table 2-3 Position-independent geometric errors

Symbol [Inasaki, 1997]	Symbol [ISO/FIDS 230-1, 2011]	Description
Location errors associated with rotary axes		
δx^0_{BY}	$E_{X(0Y)B}$	Linear offset of B-axis average line in X-direction.
δy^0_{BY}	$E_{Y(0Y)B}$	Linear offset of the B-coordinate system in Y-direction, which is equivalent to the linear offset of C-axis average line in Y-direction.
δz^0_{BY}	$E_{Z(0Y)B}$	Linear offset of B-axis average line in Z-direction.
α^0_{BY}	$E_{A(0Y)B}$	Parallelism error of B-axis to Y-axis around X-axis.
β^0_{BY}	$E_{B(0Y)B}$	Initial angular positioning error of B-axis.
γ^0_{BY}	$E_{C(0Y)B}$	Parallelism error of B-axis to Y-axis around Z-axis.
δx^0_{CB}	$E_{X(0B)C}$	Linear offset of C-axis average line from B-axis average line in X-direction.
α^0_{CB}	$E_{A(0B)C}$	Squareness error of C-axis to B-axis.
Location errors associated with linear axes		
α^0_{YZ}	$E_{A(0Y)Z}$	Squareness error of Z-axis to Y-axis.
β^0_{XZ}	$E_{B(0X)Z}$	Squareness error of Z-axis to X-axis.
γ^0_{YX}	$E_{C(0Y)X}$	Squareness error of X-axis to Y-axis.

(4) Position-dependent geometric errors of rotary axes

It is to be emphasized that location errors only represent *mean* location and orientation of axis of rotation. The location and the orientation may vary due to its rotation (described by the term "axis of rotation error motion" in ISO230-7 [ISO 230-7, 2006]). A large class of error motions can be modeled as geometric errors that vary depending on the angular position of a rotary axis. They are referred to as *position-dependent geometric errors* [Lee, 2009] in this study.

For example, as is shown in Fig. 2-7(a), geometric errors δx^0_{CB} and δy^0_{CB}, which are defined as linear offset of the C-axis *average line* with respect to the B-coordinate system, are constant and independent on the rotation of C-axis by definition. On the other hand, when they are parameterized dependent on C-axis angular position, denoted by $\delta x_{CB}(C)$ and $\delta y_{CB}(C)$, they can model a periodic pure radial error motion [ISO 230-7, 2006], or "run-out" of C-axis, as is shown in Fig.

2-7(b). Similarly, a periodic tilt error motion [ISO 230-7, 2006] of C-axis, often called “angular motion” or “coning” [Schwenke, 2008] in the industry, can be modeled by $\alpha_{CB}(C)$ and $\beta_{CB}(C)$, as shown in Fig. 2-7(c).

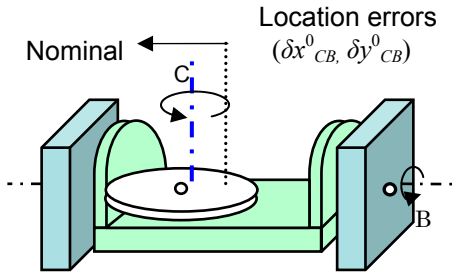

(a) Position-independent geometric errors

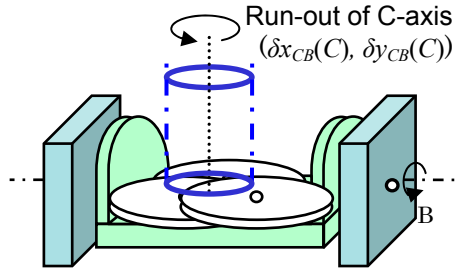

(b) Periodic pure radial error motion (run-out) of C-axis

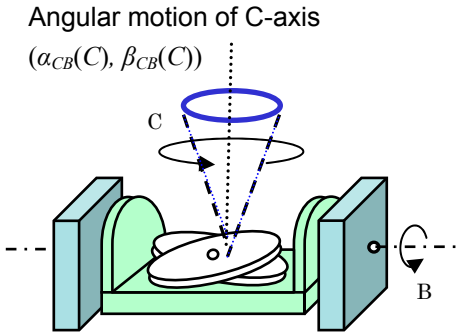

(c) Periodic conical tilt error motion (angular motion) of C-axis

Fig. 2-7 Examples of position-independent and position-dependent geometric errors.

Table 2-4 shows position-dependent geometric errors associated with rotary axes for the machine configuration in Fig. 2-5. It is to be noted that parameters associated with B-axis are dependent only on the angular position of B-axis, while those associated with C-axis are dependent on both B- and C-axes angular positions. This is because that an error motion of C-axis may be affected

by B-axis angular position (its typical causes include gravity-induced deformation of bearings or mechanical structure).

In this study, we represent position-dependent geometric errors as follows:

$$\delta x_{BY}(B) = \delta x^{0}{}_{BY} + \delta \tilde{x}_{BY}(B) \tag{2-8}$$

where $\delta x^{0}{}_{BY}$ represents a constant term, i.e. a location error. The symbol ~ represents a position-dependent term. All the error parameters of B-axis (i.e. $\delta x_{BY}(B)$, $\delta y_{BY}(B)$, $\delta z_{BY}(B)$, $\alpha_{BY}(B)$, $\beta_{BY}(B)$, and $\gamma_{BY}(B)$) are composed of a position-independent term (see Table 2-3) and a position-dependent term, analogous to Eq. (2-8).

Table 2-4 Descriptions of position-dependent geometric errors of rotary axes

Symbol	Symbol [ISO/FIDS 230-1, 2011]	Description
$\delta x_{BY}(B)$	$E_{X(Y)B}$	Radial error motion of B-axis of rotation in X-direction with B rotation
$\delta y_{BY}(B)$	$E_{Y(Y)B}$	Axial error motion of B-axis of rotation in Y-direction with B rotation
$\delta z_{BY}(B)$	$E_{Z(Y)B}$	Radial error motion of B-axis of rotation in Z-direction with B rotation
$\delta x_{CB}(C, B)$	$E_{X(B)C}$	Radial error motion of C-axis of rotation in X-direction with C, B rotation
$\delta y_{CB}(C, B)$	$E_{Y(B)C}$	Radial error motion of C-axis of rotation in Y-direction with C, B rotation
$\delta z_{CB}(C, B)$	$E_{Z(B)C}$	Axial error motion of C-axis of rotation in Z-direction with C, B rotation
$\alpha_{BY}(B)$	$E_{A(Y)B}$	Tilt error motion of B-axis around X-axis with B rotation
$\beta_{BY}(B)$	$E_{B(Y)B}$	Angular positioning error of B-axis rotation
$\gamma_{BY}(B)$	$E_{C(Y)B}$	Tilt error motion of B-axis around Z-axis with B rotation
$\alpha_{CB}(C, B)$	$E_{A(Y)C}$	Tilt error motion of C-axis around X-axis with C, B rotation
$\beta_{CB}(C, B)$	$E_{B(B)C}$	Tilt error motion of C-axis around Y-axis with C, B rotation
$\gamma_{CB}(C, B)$	$E_{C(B)C}$	Angular positioning error of C-axis rotation

2.3.2 Kinematic model of five-axis controlled machine tools

The kinematic model to compute the tool center position (TCP) in relative to the workpiece is the basis of error calibration schemes presented in this thesis. Although its derivation can be found in many previous publications [Abbaszaheh-Mir, 2002, Inasaki, 1997, Soons, 1992, Srivastava, 1995], this subsection only briefly reviews it.

Assuming the machine configuration shown in Fig. 2-5, the TCP in the reference coordinate system is calculated as follows:

$$\begin{bmatrix} {}^{r}q \\ 1 \end{bmatrix} = {}^{r}T_{t} \begin{bmatrix} 0 & 0 & 0 & 1 \end{bmatrix}^{T} \tag{2-9}$$

$$\begin{cases} {}^{r}T_{t} = {}^{r}T_{y}\,{}^{y}T_{x}\,{}^{x}T_{t} \\ {}^{x}T_{t} = D_{a}(\alpha^{0}{}_{YZ})D_{b}(\beta^{0}{}_{XZ})D_{z}(Z^{*}) \\ {}^{y}T_{x} = D_{c}(\gamma^{0}{}_{XY})D_{x}(X^{*} + p_{sx}) \\ {}^{r}T_{y} = D_{y}(Y^{*} + p_{sy}) \end{cases} \tag{2-10}$$

where ${}^{r}T_{t} \in \Re^{4\times4}$ denotes a HTM (Homogeneous Transformation Matrix) representing the transformation of the TCP in the tool coordinate system to the reference coordinate system. In the formulation above, the tool coordinate system is attached to the TCP. To simplify the formulation, Eq. (2-10) only contains the influence of squareness errors of linear axes shown in Table 2-3. Throughout this thesis, the left-side superscript *r* represents a vector in the reference coordinate system, and *t* represents a vector in the tool coordinate system. $D_x(x)$, $D_y(y)$, $D_z(z) \in \Re^{4\times4}$ represent the HTMs for linear motions in X-, Y-, and Z-directions respectively, and $D_a(a)$, $D_b(b)$, $D_c(c) \in \Re^{4\times4}$ represent the HTMs for angular motions about X-, Y-, and Z-directions respectively (see Eq. (2-15)). Command positions of X-, Y-, Z-, B-, and C-axes are given by X^*, Y^*, Z^*, B^*, and $C^* \in \Re$, respectively. Note that (p_{sx}, p_{sy}) is the center offset of the sphere center with respect to the spindle axis average line.

Then, define the workpiece coordinate system attached on the rotary table (C-axis). The TCP in this workpiece coordinate system, denoted by ${}^{w}q$, is calculated as follows:

$$\begin{bmatrix} {}^{w}q \\ 1 \end{bmatrix} = {}^{w}T_{r} \begin{bmatrix} {}^{r}q \\ 1 \end{bmatrix} = ({}^{r}T_{w})^{-1} \begin{bmatrix} {}^{r}q \\ 1 \end{bmatrix} \tag{2-11}$$

$${}^{r}T_{w} = {}^{r}T_{b}\,{}^{b}T_{c} \tag{2-12}$$

$$\begin{aligned} {}^{r}T_{b} = {} & D_{a}(\alpha_{BY}(B^{*}))D_{b}(\beta_{BY}(B^{*}))D_{c}(\gamma_{BY}(B^{*}))\cdot \\ & D_{x}(\delta x_{BY}(B^{*}))D_{y}(\delta y_{BY}(B^{*}))D_{z}(\delta z_{BY}(B^{*}))D_{b}(B^{*}) \end{aligned} \tag{2-13}$$

$$\begin{aligned} {}^{b}T_{c} = {} & D_{a}(\alpha_{CB}(C^{*},B^{*}))D_{b}(\beta_{CB}(C^{*},B^{*}))D_{c}(\gamma_{CB}(C^{*},B^{*}))\cdot \\ & D_{x}(\delta x_{CB}(C^{*},B^{*}))D_{y}(\delta y_{CB}(C^{*},B^{*}))D_{z}(\delta z_{CB}(C^{*},B^{*}))D_{c}(C^{*}) \end{aligned} \tag{2-14}$$

Throughout this thesis, the left-side superscript *w* represents a vector in the workpiece coordinate system. The HTMs of linear motions and angular motions (i.e. $D_x(x)$, $D_y(y)$, $D_z(z)$, $D_a(a)$, $D_b(b)$, and $D_c(c)$) are given in e.g. [Inasaki, 1997, Soons, 1992, Srivastava, 1995, Slocum, 1992]:

$$D_{x}(x) = \begin{bmatrix} 1 & 0 & 0 & x \\ 0 & 1 & 0 & 0 \\ 0 & 0 & 1 & 0 \\ 0 & 0 & 0 & 1 \end{bmatrix}, \qquad D_{y}(y) = \begin{bmatrix} 1 & 0 & 0 & 0 \\ 0 & 1 & 0 & y \\ 0 & 0 & 1 & 0 \\ 0 & 0 & 0 & 1 \end{bmatrix},$$

$$D_{z}(z) = \begin{bmatrix} 1 & 0 & 0 & 0 \\ 0 & 1 & 0 & 0 \\ 0 & 0 & 1 & z \\ 0 & 0 & 0 & 1 \end{bmatrix}, \qquad D_{a}(a) = \begin{bmatrix} 1 & 0 & 0 & 0 \\ 0 & \cos a & -\sin a & 0 \\ 0 & \sin a & \cos a & 0 \\ 0 & 0 & 0 & 1 \end{bmatrix},$$

$$D_{b}(b) = \begin{bmatrix} \cos b & 0 & \sin b & 0 \\ 0 & 1 & 0 & 0 \\ -\sin b & 0 & \cos b & 0 \\ 0 & 0 & 0 & 1 \end{bmatrix}, \quad D_{c}(c) = \begin{bmatrix} \cos c & -\sin c & 0 & 0 \\ \sin c & \cos c & 0 & 0 \\ 0 & 0 & 1 & 0 \\ 0 & 0 & 0 & 1 \end{bmatrix} \tag{2-15}$$

Equation (2-11) formulates how error motions of each axis are related to the TCP in the workpiece coordinate system. Since the R-test device measures the sphere displacement relative to the work table, i.e. the TCP in the workpiece coordinate system, this equation is the basis of calibration schemes to be presented in this thesis.

It should be emphasized that the formulation presented in this subsection assumes that all the axes have a *rigid-body* behavior. Error motions of each axis caused by non-rigid body behaviors, e.g. elastic deformation caused by various loads, are beyond the scope of this thesis.

Chapter 3
Calibration of position-dependent and position-independent geometric errors of rotary axes by static R-test measurement

3.1 Introduction

As was reviewed in Chapter 1, all the previous works on the R-test in the literature [Weikert, 2004, Bringmann, 2006, Zargarbashi, 2009] only presented its application to the calibration of location errors of rotary axes. Location errors only represent "average" position and orientation of rotary axes. A strong advantage of the R-test is in its efficiency to collect a large set of sphere displacement data at various positions of rotary axes. The collected data can be used to observe not only "average" error motions of rotary axes, but also how error motions of rotary axes change with their rotation.

The objective of this chapter is to propose a new algorithm to analyze a profile of sphere displacement measured by the R-test to numerically calibrate error motions of two rotary axes at various angular positions. As was discussed in Section 2.3, such a change in error motions can be parameterized by position-dependent geometric errors.

3.2 Objective and original contribution of this chapter

Compared to previous R-test works reviewed in Section 1.2, original contributions of this chapter can be summarized as follows:

(1) While previous R-test studies focused on numerical parameterization of location errors from R-test results, it is difficult for users to *intuitively* understand error motions of rotary axes with "raw" R-test trajectories. The first contribution in this chapter is on the demonstration of an intuitive, graphical presentation method of R-test measurements to understand how error motions of rotary table changes in three-dimensional space depending

on the swiveling angle (Section 3.4).

(2) All the previous R-test studies in the literature require that error motions of linear axes must be sufficiently small as a prerequisite to calibrate error motions of rotary axes. When this assumption is not met, their approaches are subjected to potentially a significant identification error [Bringmann, 2009]. To partially address this issue, Section 3.5 proposes a scheme to separate squareness errors of linear axes by performing a set of R-test measurement cycles with different sphere positions.

(3) By extending previous works on location errors identification, Section 3.6 proposes the application of R-test to the identification of position-dependent geometric errors of a rotary axis.

Experimental case studies will be conducted on the five-axis machine tool to demonstrate these three contributions.

3.3 Measurement procedure

3.3.1 R-test measurement cycle

This section first presents the R-test static measurement procedure. This procedure is basically the same as the one presented in previous R-test studies (e.g. [Bringmann, 2006, Ibaraki, 2011, Zargarbashi, 2009]).

In a R-test measurement cycle, the machine table is indexed at each combination of given B- and C-angular positions, B_i^* (i=1, …, N_b) and C_j^* (j=1, …, N_c). Measurement poses, B_i^* and C_j^*, must be distributed over the entire workspace of each rotary axis. The X, Y, and Z axes are positioned such that there is nominally no relative displacement of the sphere to the sensors nest. The nominal sphere position in the reference coordinate system, denoted by ${}^{r}q^*(B_i^*, C_j^*) \in \Re^{3\times 1}$, is given by:

$$\begin{bmatrix} {}^{r}q^*(B_i^*, C_j^*) \\ 1 \end{bmatrix} = D_b(-B_i^*) D_c(-C_j^*) \begin{bmatrix} {}^{w}q^* \\ 1 \end{bmatrix} \tag{3-1}$$

where ${}^{w}q^* \in \Re^{3\times 1}$ represents the nominal position of the sphere in the workpiece coordinate system. D*(*) denotes the HTM, see Section 2.3.2. The right-side superscript * represents the commanded position. X-, Y- and Z-axes are

positioned at ${}^{r}q^{*}(B_i^{*},C_j^{*})$ for each B_i^{*} and C_j^{*}. An example of R-test measurement cycle is illustrated in Fig. 3-1.

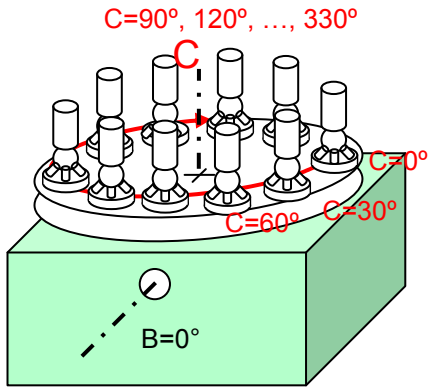

- At B=0°, C axis is indexed by e.g. every 30°.
- The spindle-side sphere is positioned by XY axes such that its relative displacement to the R-test sensors nest is nominally zero.
- Actual displacement is statically measured at each angle.

(a) When B = 0°

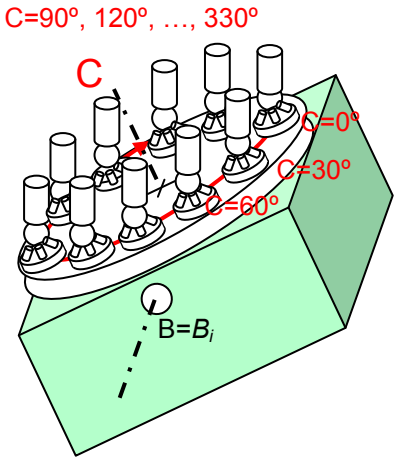

- Analogous measurement is done at various B angles (e.g. B=-90°, -60°, …, 90°).

(b) When B-axis is positioned at B_i

Fig. 3-1 An example of R-test measurement cycle.

3.3.2 Sphere position

All the previous R-test studies [Weikert, 2004, Bringmann, 2006, Zargarbashi, 2009, Ibaraki, 2011, Slamini, 2010] suggested a setup where the sphere is located away from the axis average line of C-axis rotation. The basic R-test setup [ISO/CD 10791-6.2, 2010, Weikert, 2004, Bringmann, 2006] performs a single measurement cycle as illustrated by Setup 1-a (outer low) in Fig. 3-2(a) (For the simplicity, Fig. 3-2(a) only shows a measurement cycle at B_i^{*} = 0°. Analogous cycles are performed at given B_i^{*}'s).

When a single sphere is used, it is not possible to find the orientation of

the rotation axis of C-axis at each C_j^*. To observe C-axis tilt error motions, the R-test measurement cycle must be repeated at two different sphere positions, as depicted in Setups 1-a (outer low) and 1-b (outer high) in Fig. 3-2(a).

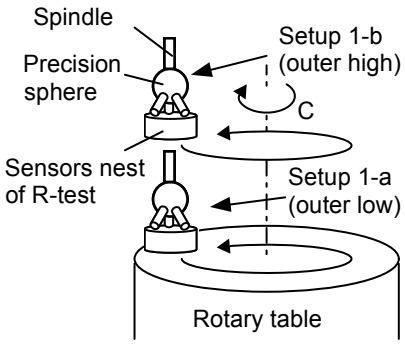

(a) Setups 1-a (outer low) and 1-b (outer high)

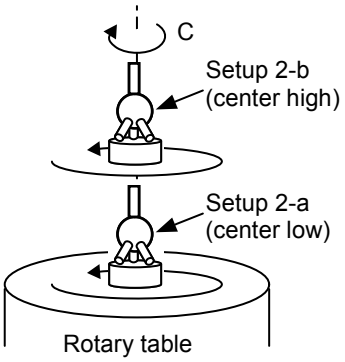

(b) Setups 2-a (center low) and 2-b (center high)

Fig. 3-2 Setups for R-test measurement.

These R-test measurement cycles require the synchronous motion of linear axes and a rotary axis. Therefore, the measured displacement profile is influenced by not only error motions of a rotary axis, but also those of linear axes, as was quantitatively discussed in [Bringmann, 2009]. When the sphere is located on the nominal C-axis average line (see Fig. 3-2(b)), no linear axis moves with C-axis rotation at given B_i^*. In many machines, it is often difficult, or not possible, to place the sphere at the intersection of B- and C-axes. Thus, when the cycle in Figs. 3-2(a) and (b) is performed at different B_i^*, linear axes (X and Z-axes) must move to place the sphere on the nominal C-axis average line. In Setup 2-a (center low) and 2-b (center high) in Fig. 3-2(b), the positioning error with this operation is only influence of error motions of linear axes on measured

profiles.

By combining Setups 2-a (center low) and 2-b (center high) in Fig. 3-2(b), all the tilt and linear error motions of B- and C-axes can be observed, except for the angular positioning error of C-axis. To simplify the measurement procedure, this thesis assumes that the angular positioning error of C-axis is pre-calibrated by a different measuring instrument and needs not to be measured by R-test. Note that the combination of Setups 2-a (center low) and 2-b (center high) is in principle equivalent to the test described in ISO 230-7 [ISO 230-7, 2006].

3.4 Graphical presentation of R-test profiles

(1) Background and objective

By graphically presenting measured three-dimensional trajectories, an experienced user can make many intuitive observations on error motions of rotary axes, and possibly their potential causes. Previous R-test works in the literature, reviewed in Section 1.2-(2), focused only on numerical parameterization of location errors from R-test results. No work has been reported on graphical presentation of R-test results. This section will present a procedure to graphically present displacement profiles measured by the R-test.

At each stop position with B_i^* (i=1, …, N_b) and C_j^* (j=1, …, N_c), denote the measured sphere displacement in the workpiece coordinate system by ${}^w\overline{q}(B_i^*, C_j^*)$. Note that $-{}^w\overline{q}(B_i^*, C_j^*)$ represents the displacement of the R-test sensors nest relative to the spindle-side sphere. It is hereby referred to as the measured sensors nest displacement. We display the sensors nest displacement $-{}^w\overline{q}(B_i^*, C_j^*)$, instead of the sphere displacement, ${}^w\overline{q}(B_i^*, C_j^*)$, since the main scope is in evaluating error motions of rotary axes. The symbol with the bar "¯" represents the measured displacement by the R-test.

Note that, since incremental linear displacement sensors are used for the R-test probes, the measured displacement must be reset at the initial position (i.e. ${}^w\overline{q}(B_i^*, C_j^*) = 0$ at $B_i^* = C_j^* = 0$º), which is called "initial resetting" in [Ibaraki, 2011]. After the initial resetting, the sphere displacement measured by R-test

probes is represented by:

$$ {}^{w}\overline{q}(B_i^*, C_j^*) = {}^{w}q(B_i^*, C_j^*) - {}^{w}q(0^\circ, 0^\circ) \tag{3-2} $$

where ${}^{w}q(B_i^*, C_j^*)$ represents the sphere displacement given by the kinematic model, Eq. (2-11) in Section 2.3.2. In other words, the symbol with the bar"¯" represents the sphere displacement under the influence of initial resetting.

It is difficult to intuitively understand rotary axes error motions from a "raw" R-test profile in the workpiece coordinate system (see experimental data in Fig. 3-8 in Section 3.7.1.2). By converting it to the reference coordinate system, its intuitive understanding becomes much easier. Furthermore, measured R-test profiles are influenced by not only the machine's error motions, but also many factors such as the "initial resetting" or a calibration error of the tool length. For more intuitive understanding of rotary axes error motions, the influence of such factors must be removed. This is the basic idea of the graphical presentation scheme presented in this section.

(2) Proposed analysis procedure

This section proposes the following procedure for the display of measured R-test profile, ${}^{w}\overline{q}(B_i^*, C_j^*)$.

a. Transformation to the reference coordinate system:

The measured sensor displacement in the workpiece coordinate system, denoted by $-{}^{w}\overline{q}(B_i^*, C_j^*)$, is transformed to the position in the reference coordinate system, denoted by ${}^{r}\overline{q}(B_i^*, C_j^*)$ by using nominal angular positions of B- and C-axes as follows:

$$ \begin{bmatrix} {}^{r}\overline{q}(B_i^*, C_j^*) \\ 1 \end{bmatrix} = D_b(-B_i^*) D_c(-C_j^*) \begin{bmatrix} -{}^{w}\overline{q}(B_i^*, C_j^*) \\ 1 \end{bmatrix} \tag{3-3} $$

b. Compensation of initial resetting:

The "initial resetting" of displacement sensors (see Eq. (3-2)) makes it more difficult to intuitively understand the influence of an offset of the axis average line of rotary axes. For example, when there exists an offset in the C-axis

average line from its nominal position in the X-direction, denoted by δx^0_{CY} (= $\delta x^0_{CB} + \delta x^0_{BY}$ at $B_i^* = 0°$ in Table 2-3), and in the Y-direction, denoted by δy^0_{CY} (= δy^0_{BY} in Table 2-3), its influence on the R-test profile, ${}^w\hat{\bar{q}}(B_i^*, C_j^*)$, is given by:

$$\begin{bmatrix} {}^w\hat{\bar{q}}(B_i^*, C_j^*) \\ 1 \end{bmatrix} = D_b(B_i^*) D_c(C_j^*) \begin{pmatrix} \delta x^0_{CY} \\ \delta y^0_{CY} \\ 0 \\ 1 \end{pmatrix} - \begin{pmatrix} \delta x^0_{CY} \\ \delta y^0_{CY} \\ 0 \\ 0 \end{pmatrix} \tag{3-4}$$

The symbol with the hat "^" represents the estimate. The last term of Eq. (3-4) represents the initial resetting, making ${}^w\hat{\bar{q}}(B_i^* = 0°, C_j^* = 0°) = [0,0,0]^T$. By substituting Eq. (3-4) into Eq. (3-3), the influence of δx^0_{CY} and δy^0_{CY} to the sphere position in the reference coordinate system, ${}^r\bar{q}(B_i^*, C_j^*)$, is illustrated in Fig. 3-3(a) (at B_i^* = 0º, C_j^* = 0º~360º). This suggests that the offset of C-axis average line is represented by constant expansion or shrinkage of the R-test trajectory.

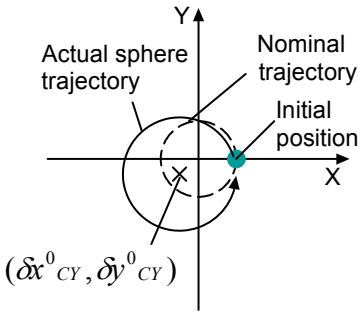

(a) With resetting at initial position, ${}^r\bar{q}(B_i^*, C_j^*)$

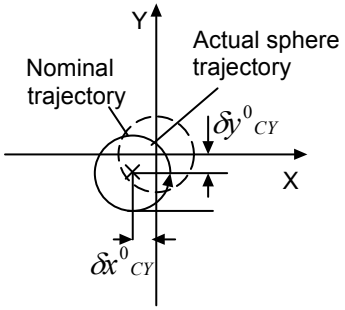

(b) With compensating initial resetting, ${}^rq(B_i^*, C_j^*)$

Fig. 3-3 An illustrative example of the influence of axis shift of C-axis average line in X-direction to the sphere position in the reference coordinate system, ${}^r\bar{q}(B_i^*, C_j^*)$, at $B_i^* = 0°$, $C_j^* = 0°$~360°.

The influence of the initial resetting can be numerically removed from R-test error profiles by:

$$\begin{bmatrix} {}^{r}q(B_i^*, C_j^*) \\ 1 \end{bmatrix} = D_b(-B_i^*) D_c(-C_j^*) \left(-{}^{w}\overline{q}(B_i^*, C_j^*) - \begin{pmatrix} \delta\hat{x}^0{}_{CY} \\ \delta\hat{y}^0{}_{CY} \\ 0 \\ 0 \end{pmatrix} \right) \tag{3-5}$$

The symbol ${}^{r}q(B_i^*, C_j^*)$ is without the bar "¯", indicating that the influence of initial resetting is removed. After the compensation of "initial resetting", the trajectory would be shown as in Fig. 3-3(b), where the existence of the center offset is easier to be intuitively understood (the circular trajectory is "shifted" by the distance and the direction equal to the center offset of C-axis).

In Eq. (3-5), $\delta\hat{x}^0{}_{CY}$ and $\delta\hat{y}^0{}_{CY}$ represent the estimate of $\delta x^0{}_{CY}$ and $\delta y^0{}_{CY}$. They can be obtained by best-fitting the "raw" measured trajectory, ${}^{w}\overline{q}(B_i^*, C_j^*)$, to the model described in Eq. (3-4) for $B_i^* = 0°$ and $C_j^* = 0°$~$360°$. This can be done in an analogous manner as the algorithm to be presented in Section 3.6.

c. Elimination of influence of offset errors of rotary axis:

For example, the center offset of B-axis in the Z-direction, denoted by $\delta z^0{}_{BY}$ (see Section 2.3.1), is often caused by a calibration error of the tool length (i.e. the distance from the spindle gauge line to the sphere center). This should be regarded as a setup error, not the machine's inherent error. Similarly, an offset error of the axis average line of C-axis in X- and Y-directions, denoted by $\delta x^0{}_{BY}$ and $\delta y^0{}_{BY}$ (note that $\delta y^0{}_{BY}$ equivalently represents the offset of C-axis average line in the Y-direction, and $\delta x^0{}_{BY} + \delta x^0{}_{CB}$ represent the offset of C-axis average line in the X-direction at B = 0°), can be easily eliminated by properly tuning CNC control parameters, and thus are typically regarded as setup errors. In our study, their influence is numerically eliminated from measured R-test profiles to more clearly present the machine's inherent error motions only.

It must be emphasized that this operation only eliminates the influence of "average" center offset, i.e. location errors, and their change with the B-rotation are shown. These parameters are also estimated by best-fitting the "raw"

measured trajectory, ${}^{w}\bar{q}(B_i^*, C_j^*)$, to the machine's kinematic model (for its detailed identification algorithm, see Section 3.6). Denote the sensors nest's displacement profile after eliminating the influence of estimated offset errors of C- and B-axes (i.e. $\delta\hat{x}^0{}_{CY}$, $\delta\hat{y}^0{}_{CY}$ and $\delta\hat{z}^0{}_{BY}$) by ${}^{r}p(B_i^*, C_j^*)$. ${}^{r}p(B_i^*, C_j^*) \in \Re^3$ is given by:

$$\begin{bmatrix} {}^{r}p(B_i^*, C_j^*) \\ 1 \end{bmatrix} = \begin{bmatrix} {}^{r}q(B_i^*, C_j^*) \\ 1 \end{bmatrix} - \begin{pmatrix} \delta\hat{x}^0{}_{CY} \\ \delta\hat{y}^0{}_{CY} \\ \delta\hat{z}^0{}_{BY} \\ 0 \end{pmatrix} \tag{3-6}$$

The symbol, "p", instead of "q", represents the sensors displacement where the influence of offset errors is removed.

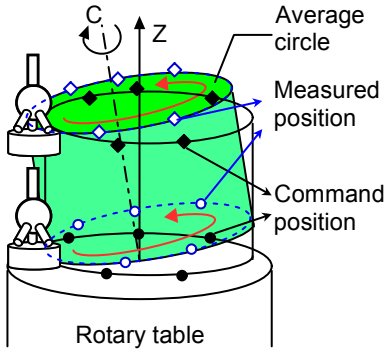

(a) Example 1: With squareness error of C- to X-axis

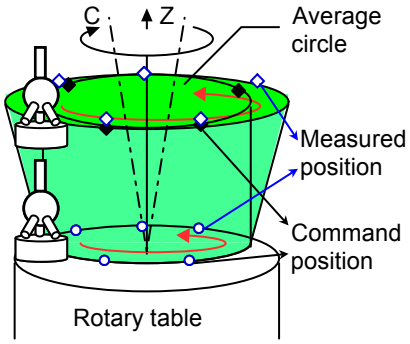

(b) Example 2: With tilt error motion ("coning") of C-axis

Fig. 3-4 Average circles with R-test plot.

d. Displaying average circles:

When the sphere is located away from the C-axis (i.e. in Setups 1-a (outer

low) and 1-b (outer high) in Fig. 3-2(a)), measured trajectories are plotted with "average circles", to more clearly observe average error motions at each B-angle. Two typical examples of C-axis error motions are illustrated in Figs. 3-4(a) and (b). For calculating "average circles", the center and orientations of a circle are best-fit to measured position trajectory of the sensors nest, ${}^{r}p(B_i^*, C_j^*)$ at each B_i^*, by the non-linear least square method.

3.5 Separation of squareness error of linear axes

(1) Background and objective

All the previous R-test studies [Weikert, 2004, Bringmann, 2006, Zargarbashi, 2009, Slamini, 2010, Ibaraki, 2011] assumed error motions of linear axes to be sufficiently small, in order to calibrate error motions of rotary axes. When this assumption is not met, it may cause significant calibration error. This section proposes that a part of error motions of linear axes can be separately identified by performing three R-test cycles illustrated in Fig. 3-2 (Setups 1-a ,2-a, and 2-b).

(2) Proposed analysis procedure

In Setups 2-a (center low) and 2-b (center high), the R-test measurement cycle only requires C-axis rotation at each B_i^* (i=1, …, N_b). Therefore, error motions of linear axes do not affect the R-test measurement, except for the positioning error at the sphere's nominal position. When the sphere are located on the C-axis average line, combining Setups 2-a (center low) and 2-b (center high), the orientation of lines connecting these two setups represents the parallelism error of the C-axis average line to the Z-axis. On the other hand, when the sphere is located away from the C-axis (i.e. Setup 1-a (outer low) or Setup 1-b (outer high)), the average orientation of the measured trajectory at B_i^* = 0° represents the squareness of the C-axis average line to X- and Y-axes.

Therefore, by combining all measured profiles (i.e. Setups 1(outer) and Setups 2(center)), one can observe squareness errors of Z-axis to X- and Y-axes at B_i^* = 0°. Analogous observation applies at different B_i^*. This is the basic idea

of the discussion presented in this section. The procedure to separate squareness errors of linear axes is presented as follows:

a. Squareness of C-axis to X- and Y-axes of the B-coordinate system:

In Setups 1-a (outer low), denote the measured sensor position by ${}^{r}p_{1a}(B_i^*, C_j^*)$. At each B_i^*, denote the unit normal vector of the average circle of ${}^{r}p_{1a}(B_i^*, C_j^*)$ (j=1, …, N_c) by ${}^{r}n_{1a}(B_i^*) \in \Re^3$. Then, the orientation of ${}^{r}n_{1a}(B_i^*)$ from its nominal direction represents the squareness error of the C-axis average line and the X-axis (or Y-axis) average line in the B-coordinate system (see Fig. 3-10(c) as an illustrating example). The angular error of ${}^{r}n_{1a}(B_i^*)$ to the Y-axis of the B-coordinate system around its X-axis is denoted by ${}^{B}\alpha_{CY}(B_i^*) \in \Re$, and that to the X-axis of the B-coordinate system around its Y-axis is denoted by ${}^{B}\beta_{CX}(B_i^*) \in \Re$. Note that the B-coordinate system is defined as the coordinate system attached to the B-axis (see Section 2.3.1.2-(2) for more details). The left-side superscript "*B*" represents the quantity defined in the B-coordinate system.

b. Parallelism of C-axis to Z-axis of the B-coordinate system:

Denote the measured sensors nest position at B_i^* (i=1, …, N_b) and C_j^* (j=1, …, N_c) in Setups 2-a (center low) and 2-b (center high) respectively by ${}^{r}p_{2a}(B_i^*, C_j^*)$ and ${}^{r}p_{2b}(B_i^*, C_j^*)$ in the reference coordinate system. At each B_i^*, denote the center of gravity of ${}^{r}p_{2a}(B_i^*, C_j^*)$ and ${}^{r}p_{2b}(B_i^*, C_j^*)$ (j=1, …, N_c) by ${}^{r}g_{2a}(B_i^*) \in \Re^3$ and ${}^{r}g_{2b}(B_i^*) \in \Re^3$, respectively.

Then, the unit orientation vector of the line connecting ${}^{r}g_{2a}(B_i^*)$ and ${}^{r}g_{2b}(B_i^*)$ is denoted by ${}^{r}n_{2a}(B_i^*)$. The orientation of ${}^{r}n_{2a}(B_i^*)$ from its nominal direction represents the parallelism error of the C-axis average line and the line connecting actual higher and lower sphere positions, which can be seen as the Z-axis representative line in the B-coordinate system (see Fig. 3-11(c) as an illustrating example). The angular error of ${}^{r}n_{2a}(B_i^*)$ to the Z-axis of the

B-coordinate system around its X-axis is denoted by ${}^{B}\alpha_{CZ}(B_i^*) \in \Re$, and that around its Y-axis is denoted by ${}^{B}\beta_{CZ}(B_i^*) \in \Re$.

c. Squareness errors of Z-axis to X- and Y-axes of the B-coordinate system:

By combining (1) and (2), the squareness of Z-axis to X- (and Y-) axis of the B-coordinate system, denoted by ${}^{B}\beta_{ZX}(B_i^*)$ (and ${}^{B}\alpha_{ZY}(B_i^*)$), can be calculated at each B_i^* (i=1, …, N_b) as follows (see Fig. 3-5):

$${}^{B}\beta_{ZX}(B_i^*)={}^{B}\beta_{CX}(B_i^*)-{}^{B}\beta_{CZ}(B_i^*) \tag{3-7}$$

$${}^{B}\alpha_{ZY}(B_i^*)={}^{B}\alpha_{CY}(B_i^*)-{}^{B}\alpha_{CZ}(B_i^*) \tag{3-8}$$

It must be emphasized that ${}^{B}\beta_{ZX}(B_i^*)$ represents the Z-X squareness error in the B-coordinate system with B_i^*, not the Z-X squareness error in the reference coordinate system.

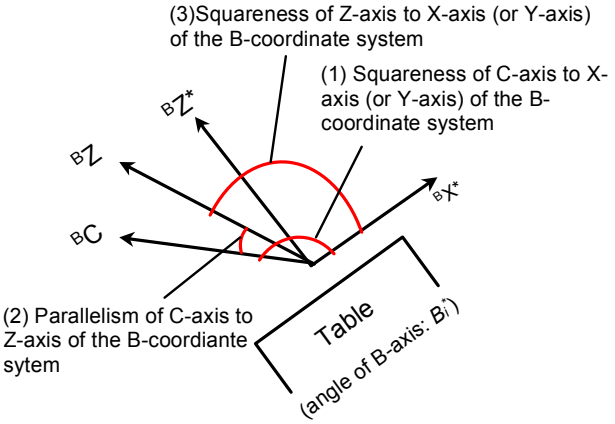

Fig. 3-5 Separation of the squareness errors of Z-axis to X- and Y-axes of the B-coordinate system. (${}^{B}X^*$ and ${}^{B}Z^*$ represent the nominal X-axis and Z-axis in the B-coordinate system; ${}^{B}Z$ represent the Z-axis of the B-coordinate system).

d. Squareness errors of linear axes:

The squareness errors of linear axes to be identified are squareness error of Z-axis to X-axis (denoted by ${}^{0}\beta_{XZ}$); squareness error of Z-axis to Y-axis (denoted by ${}^{0}\alpha_{YZ}$); and squareness error of X-axis to Y-axis (denoted by ${}^{0}\gamma_{YX}$), all in the reference coordinate system (see Table 2-3).

It is generally not possible to convert squareness errors in the B-coordinate system to those in the reference coordinate system. However, under an assumption that X-axis does not have significant angular errors and thus that squareness errors are the same at any X-positions in the measured volume, their relationship can be kinematically formulated as follows:

$$ {}^{B}\beta_{ZX}(B_i^*) = \beta^0{}_{ZX}\cos(2B_i^*) \tag{3-9} $$

$$ {}^{B}\alpha_{ZY}(B_i^*) = -\alpha^0{}_{ZY}\cos(B_i^*) + \gamma^0{}_{XY}\sin(B_i^*) \tag{3-10} $$

The squareness error of Z-axis to X-axis (i.e. $\hat{\beta}^0{}_{XZ}$) can be identified by best-fitting Eq. (3-9) to ${}^{B}\hat{\beta}_{ZX}(B_i^*)$ calculated in Eq. (3-7) by the least square method. Moreover, the squareness error of Z-axis to Y-axis (i.e. $\hat{\alpha}^0{}_{YZ}$) is calculated when $B_i^* = 0°$ from Eq. (3-10). After eliminating the influence of $\hat{\alpha}^0{}_{YZ}$ from Eq. (3-10), $\hat{\gamma}^0{}_{YX}$ is identified by best-fitting Eq. (3-10) to ${}^{B}\hat{\alpha}_{ZY}(B_i^*)$ calculated in Eq. (3-8) by the least square method.

The contribution of this subsection can be summarized as follows:

a. Z-X and Z-Y squareness errors can be estimated at each B-coordinate system. They can not be, however, straightforwardly converted to squareness errors of linear axes in the reference coordinate system.
b. When the following assumption is met, squareness errors of linear axes can be estimated in the reference coordinate system:
   squareness errors in the reference coordinate system are the same at any X positions. This assumption can not be met when, for example, the X-axis has significant angular errors.
c. When the assumptions above are met, the influence of squareness errors of linear axes can be removed from R-test profile (see Section 3.6.2).

3.6 Identification of position-independent and position-dependent geometric errors of a rotary axis

3.6.1 Objective

While the graphical presentation of R-test results, presented in Section 3.4, is important to intuitively understand error motions of rotary axes, it is also

important to numerically parameterize error motions as an “error map” of rotary axes, particularly when its numerical compensation is intended to apply. As was discussed in Section 2.3, an “error map” of rotary axes can be parameterized as position-dependent geometric errors.

We will first present an algorithm to identify location errors, or position-independent geometric errors, listed in Table 2-3, from R-test results, in Section 3.6.3. Although the identification of location errors has been already presented by some researchers in the literature [Bringmann, 2006, Ibaraki, 2011], we start from its brief review as the basis.

Then, in Section 3.6.4, it will be extended to position-dependent geometric errors. An algorithm to numerically parameterize position-dependent geometric errors of B-axis is proposed. This part is an original contribution of this thesis.

3.6.2 Separation of the influence of squareness errors of linear axes

The R-test measurement result of Setup 1-a (in Fig. 3-2(a)) is used for the identification. The influence of squareness errors of linear axes on the TCP in the reference coordinate system, ${}^{r}\hat{q}^{s} \in \Re^3$, is derived from Eqs. (2-9) and (2-10) in Section 2.3.2:

$$\begin{bmatrix} {}^{r}\hat{q}^{s} \\ 1 \end{bmatrix} = {}^{r}T_{t} \begin{bmatrix} 0 & 0 & 0 & 1 \end{bmatrix}^{T} \tag{3-11}$$

$$\begin{cases} {}^{r}T_{t} = {}^{r}T_{y}\,{}^{y}T_{x}\,{}^{x}T_{t} \\ {}^{x}T_{t} = D_{a}(\alpha^{0}{}_{YZ})D_{b}(\beta^{0}{}_{XZ})D_{z}(Z^{*}) \\ {}^{y}T_{x} = D_{c}(\gamma^{0}{}_{XY})D_{x}(X^{*}) \\ {}^{r}T_{y} = D_{y}(Y^{*}) \end{cases} \tag{3-12}$$

The definition of squareness errors of linear axes is presented in Table 2-3 in Section 2.3.1. In ${}^{r}\hat{q}^{s}$, the “^” represents the displacement calculated with the kinematic model. The right-side superscript “s” denotes the influence of linear axes squareness errors.

The R-test measures the TCP displacement in the workpiece coordinate system. The influence of squareness errors of linear axes on the R-test measurement result, ${}^{w}\hat{\bar{q}}^{s}(B_i^{*}, C_j^{*}) \in \Re^3$, is given by:

$$\begin{bmatrix} {}^{w}\hat{q}^{s}(B_i^*, C_j^*) \\ 1 \end{bmatrix} = {}^{w}T_r \begin{bmatrix} {}^{r}\hat{q}^{s} \\ 1 \end{bmatrix} = (D_b(B^*)D_c(C^*))^{-1} \begin{bmatrix} {}^{r}\hat{q}^{s} \\ 1 \end{bmatrix} \tag{3-13}$$

$${}^{w}\hat{\bar{q}}^{s}(B_i^*, C_j^*) = {}^{w}\hat{q}^{s}(B_i^*, C_j^*) - {}^{w}\hat{q}^{s}(0^\circ, 0^\circ) \tag{3-14}$$

The squareness errors of linear axes estimated in Section 3.5 (i.e. ${\alpha^0}_{YZ}$, ${\beta^0}_{XZ}$, and ${\gamma^0}_{YX}$) are numerically removed from the R-test measurement profile before the identification of geometric errors of rotary axes.

3.6.3 Identification of position-independent geometric errors

It is important to note that R-test probes can only measure the displacement of sphere center from its initial positions (i.e. the position when $B_i^* = C_j^* = 0^\circ$). As was discussed in Section 3.4-(2), with considering the influence of this "initial resetting", the sphere displacement measured by R-test probes is represented by Eq. (3-2) in Section 3.4.

Denotes a set of location errors associated with the rotary table shown in Table 2-3 by:

$$\omega_0 = [\delta {x^0}_{BY}, \delta {y^0}_{BY}, \delta {z^0}_{BY}, {\alpha^0}_{BY}, {\beta^0}_{BY}, {\gamma^0}_{BY}, \delta {x^0}_{CB}, {\alpha^0}_{CB}]^T \tag{3-15}$$

The objective of the algorithm is to identify ω_0. When the sphere displacement, ${}^{w}\bar{q}(B_i^*, C_j^*)$, is measured by R-test probes, ω_0 is identified by solving the following problem:

$$\min_{\hat{\omega}_0} \sum_{i,j} \left\| ({}^{w}\bar{q}(B_i^*, C_j^*) - {}^{w}\hat{\bar{q}}^{s}(B_i^*, C_j^*)) - \left(\frac{\partial\left({}^{w}\hat{q}(B_i^*, C_j^*)\right)}{\partial \omega_0} - \frac{\partial\left({}^{w}\hat{q}(0^\circ, 0^\circ)\right)}{\partial \omega_0} \right) \omega_0 \right\|^2 \tag{3-16}$$

where $\|*\|$ represents the 2-norm. ${}^{w}\hat{\bar{q}}^{s}(B_i^*, C_j^*)$ represents the influence of squareness errors of linear axes, identified in Eq. (3-14). The analytical formulation of Jacobian matrices (i.e. $\partial\left({}^{w}\hat{q}(B_i^*, C_j^*)\right)/\partial\omega_0$) can be derived from the kinematic model given in Eq.(2-11), as is presented in [Ibaraki, 2011]. It can be also numerically computed [Bringmann, 2006]. The problem (3-16) can be solved by the least square method.

3.6.4 Identification of position-dependent geometric errors of a rotary axis

As was described in Section 2.3, location errors only represent "average" position and orientation of a rotary axis. The position and the orientation of a rotary axis may vary with its rotation. The objective of this subsection is to present an algorithm to numerically parameterize position-dependent geometric errors associate with B-axis (see Table 2-4 in Section 2.3.1.2), such that an "error map" of B-axis can be obtained to describe how position and orientation of B-axis changes with the B-rotation. This subsection does not consider position-dependent geometric errors of C-axis, since they can be directly observed from R-test results presented in Section 3.4.

The influence of estimated position-independent terms, $\hat{\omega}_0$, on the measured sphere displacement, ${}^w\hat{\bar{q}}^0(B_i^*, C_j^*)$, is derived from Eqs. (2-9) and (2-10) in Section 2.3.2:

$$\begin{bmatrix} {}^w\hat{q}^0(B_i^*, C_j^*) \\ 1 \end{bmatrix} = {}^wT_r \begin{bmatrix} {}^rq \\ 1 \end{bmatrix} = ({}^rT_w)^{-1} \begin{bmatrix} {}^rq \\ 1 \end{bmatrix} \tag{3-17}$$

$${}^rT_w = {}^rT_b\,{}^bT_c \tag{3-18}$$

$${}^rT_b = D_a(\hat{\alpha}^0{}_{BY})D_b(\hat{\beta}^0{}_{BY})D_c(\hat{\gamma}^0{}_{BY})D_x(\delta\hat{x}^0{}_{BY})D_y(\delta\hat{y}^0{}_{BY})D_z(\delta\hat{z}^0{}_{BY})D_b(B^*) \tag{3-19}$$

$${}^bT_c = D_a(\hat{\alpha}^0{}_{CB})D_x(\delta\hat{x}^0{}_{CB})D_c(C^*) \tag{3-20}$$

$${}^w\hat{\bar{q}}^0(B_i^*, C_j^*) = {}^w\hat{q}^0(B_i^*, C_j^*) - {}^w\hat{q}^0(0^\circ, 0^\circ) \tag{3-21}$$

Denotes a set of the position-dependent geometric errors associated with B-axis to be identified shown in Table 2-4 by:

$$\omega_B(B_i^*) = [\delta\tilde{x}_{BY}(B_i^*), \delta\tilde{y}_{CB}(B_i^*), \delta\tilde{z}_{BY}(B_i^*), \tilde{\alpha}_{BY}(B_i^*), \tilde{\beta}_{BY}(B_i^*), \tilde{\gamma}_{BY}(B_i^*)]^T \tag{3-22}$$

The objective of the algorithm is to identify $\omega_B(B_i^*)$ for all given B_i^*'s. When the sphere displacement, ${}^w\bar{q}(B_i^*, C_j^*)$, is measured by R-test probes, $\omega_B(B_i^*)$ is identified by solving the following problem with the least square method:

$$\min_{\hat{\omega}_B(B_i^*)} \sum_{i,j} \left\| ({}^w\bar{q}(B_i^*, C_j^*) - {}^w\hat{\bar{q}}^s(B_i^*, C_j^*) - {}^w\hat{\bar{q}}^0(B_i^*, C_j^*)) - \left(\frac{\partial\left({}^w\hat{q}(B_i^*, C_j^*)\right)}{\partial\omega_B(B_i^*)} - \frac{\partial\left({}^w\hat{q}(0^\circ, 0^\circ)\right)}{\partial\omega_B(B_i^*)} \right) \omega_B(B_i^*) \right\|^2 \tag{3-23}$$

Note that the Jacobian matrices (i.e. $\partial\left({}^{w}q(B_i^*, C_j^*)\right)/\partial\omega_B(B_i^*)$) in the formulation above can be analytically derived from Eq.(2-11) in an analogous manner as in Section 3.6.3.

3.7 Experimental case studies

3.7.1 Graphical presentation of R-test profiles

3.7.1.1 Experimental setup

The objective of the experimental case study to be presented in this section is to demonstrate the schemes proposed in this chapter: 1) graphical presentation of R-test results (Section 3.4); 2) separation of squareness errors of linear axes (Section 3.5); and 3) identification of position-dependent geometric errors of a rotary axis (Section 3.6).

The R-test measurement was experimentally conducted on a commercial small-sized five-axis machine tool of the configuration shown in Fig. 2-5 (NMV1500DCG by Mori Seiki Co., Ltd.). Table 3-1 shows the main specifications of NMV1500DCG. Figure 3-5 shows the experimental setups: Setups 1-a (outer low) and 1-b (outer high) (see Fig. 3-2(a)).

R-test measurement cycles are conducted in all of four setups in Figs. 3-2(a) and (b). Nominal sphere locations in the workpiece coordinate system are:

- Setup 1-a (outer low): ${}^{w}q_{1a}{}^{*}$ = [0, -90.0, 40.6] (mm)
- Setup 1-b (outer high): ${}^{w}q_{1b}{}^{*}$ = [0, -90.0, 140.6] (mm)
- Setup 2-a (center low): ${}^{w}q_{2a}{}^{*}$ = [0, 0, 40.6] (mm)
- Setup 2-b (center high): ${}^{w}q_{2b}{}^{*}$ = [0, 0, 140.6] (mm)

In each setup, the R-test measurement cycle is conducted with the following command B and C angular positions:

B_i^* = -75°, -50°, …, 75° (i = 1,…,7)

C_j^* = 0°, 30°, …, 330° (j = 1,…,12)

Total 7×12 = 84 points are measured.

The command trajectory of each axis (i.e. X, Y, Z, B, and C-axis) for Setup 1-a (outer low) and Setup 1-b (outer high), is shown in Fig. 3-7.

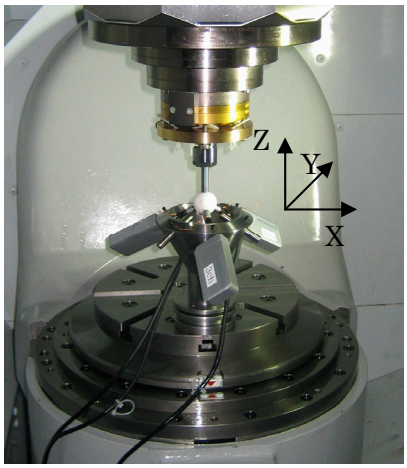

(a) Setup 1-a (outer low) in Fig. 3-2(a)

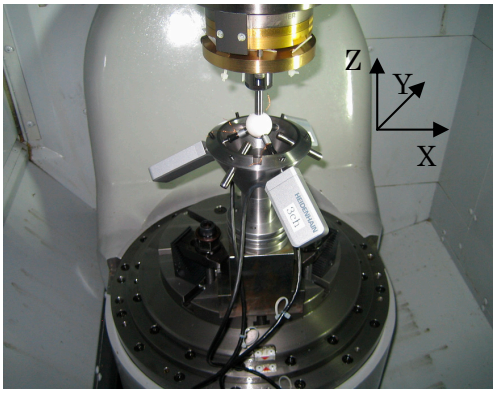

(b) Setup 1-b (outer high) in Fig. 3-2(a)

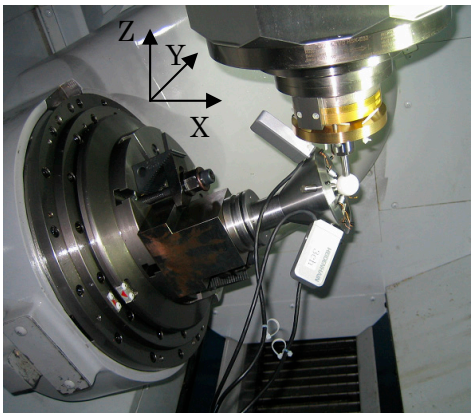

(c) Setup 1-b (outer high) at B = -75°

Fig. 3-6 R-test experimentation setups: Setup 1-a (outer low) and Setup 1-b (outer high) in Fig. 3-2(a).

Table 3-1 Specifications of NMV1500DVG from Mori Seiki [Mori Seiki]

	X	Y	Z	B	C
Stroke	420 mm	210 mm	400 mm	-180~160°	360°
Driven system	Ball screw and servo motor			Direct Drive motor	
Size of work table	Φ250 mm				

3.7.1.2 Measurement result

Figure 3-8 shows "raw" sphere displacements measured by the R-test sensors nest, ${}^{w}\overline{q}(B_i^*, C_j^*)$, in the workpiece coordinate system (only the measured profile in Setup 1-a (outer low) is shown).

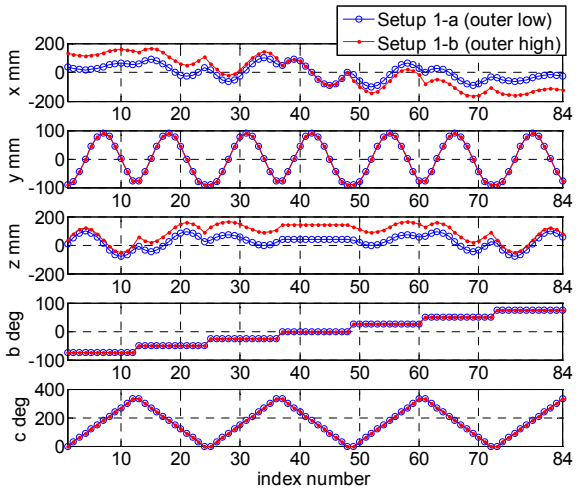

Fig. 3-7 Commanded X^*, Y^*, Z^*, B^*, and C^* trajectories for the Setup 1-a (outer low) and Setup 1-b (outer high).

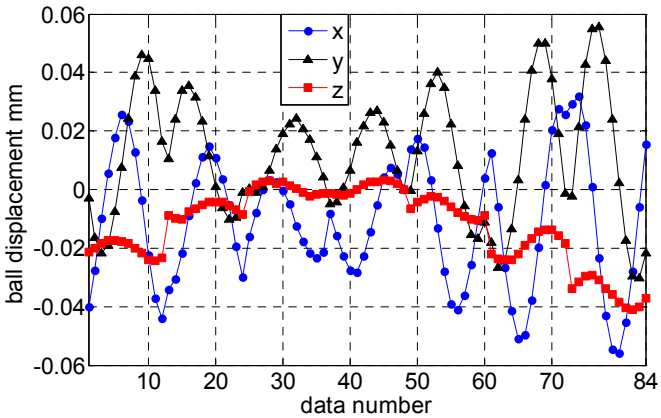

Fig. 3-8 "Raw" sphere displacements measured by the R-test in the workpiece coordinate system (Setup 1-a (outer low)).

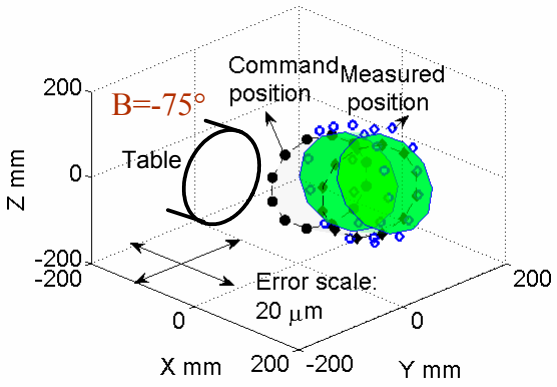

(a) At B_i^* = -75°

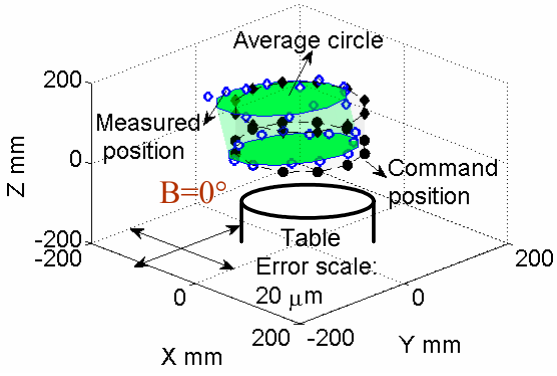

(b) At B_i^* = 0º

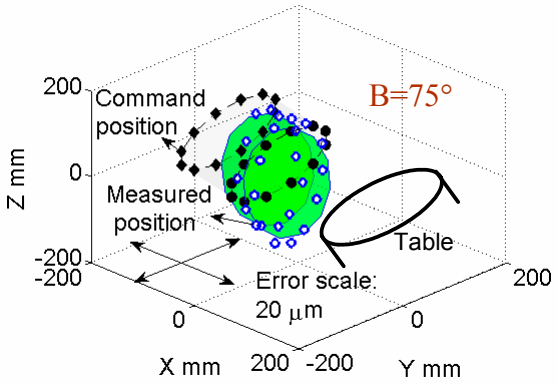

(c) At B_i^* = 75º

Fig. 3-9 Sensor positions measured by R-test with C-rotation at B_i^* = -75º, 0º, and 75º(3D view) in Setups 1-a (outer low) and 1-b (outer high). An error of measured position ("○" marks) from its command position ("●" marks) is magnified 10,000 times.

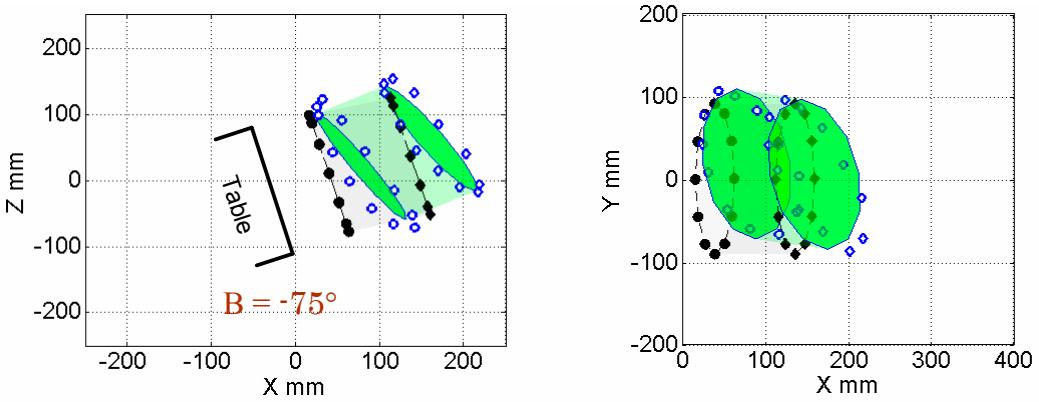

Projection onto XZ plane　　Projection onto XY plane

(a) At B_i^* = -75°

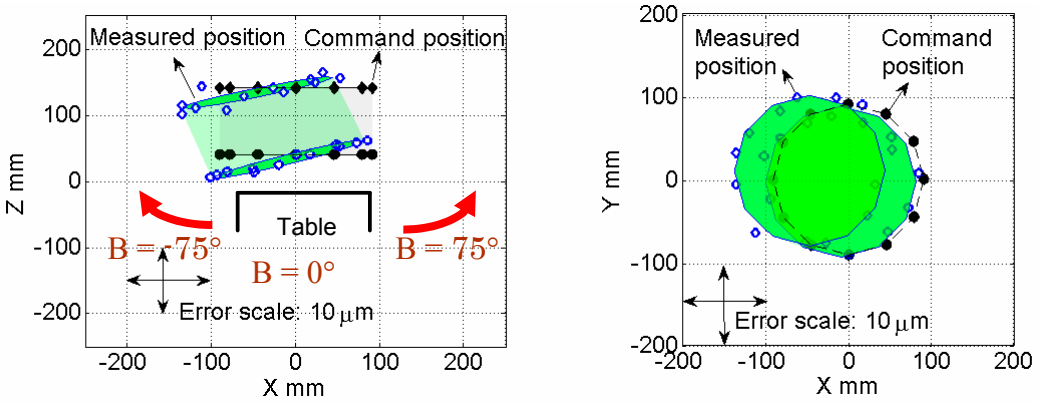

Projection onto XZ plane　　Projection onto XY plane

(b) At B_i^* = 0°

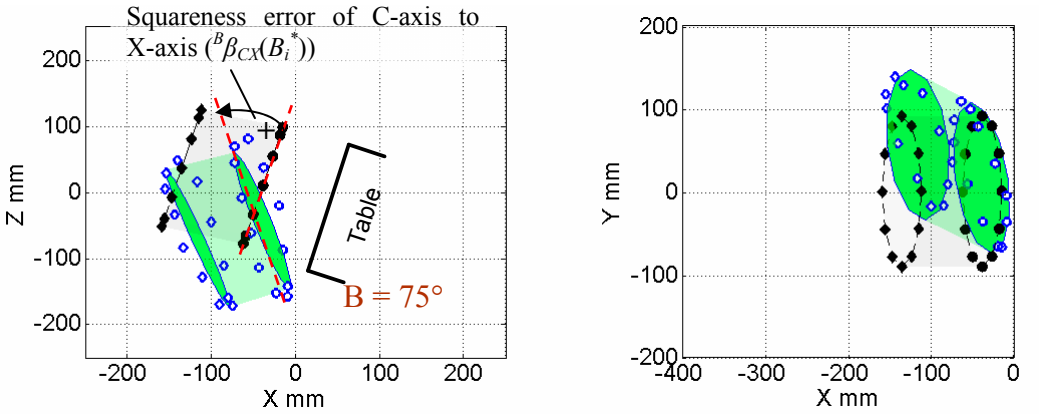

Projection onto XZ plane　　Projection onto XY plane

(c) At B_i^* = 75°

Fig. 3-10 Sensor positions measured by R-test with C-rotation at B_i^* = -75º, 0º, and 75º (3D view) in Setups 1-a (outer low) and 1-b (outer high) , projected onto XZ plane and XY plane.

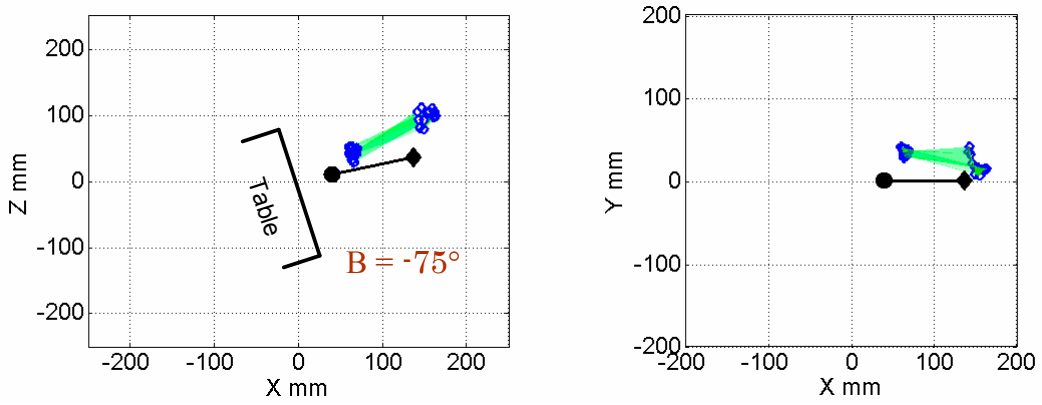

Projection onto XZ plane　　Projection onto XY plane

(a) At B_i^* = -75°

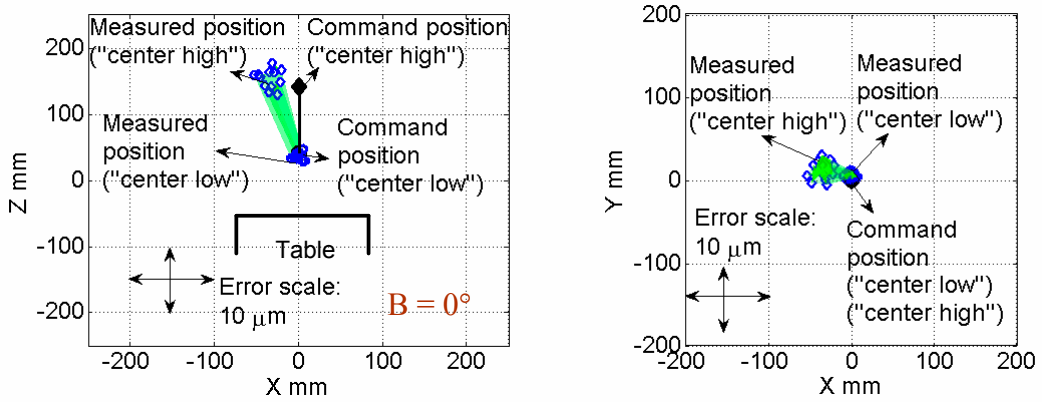

Projection onto XZ plane　　Projection onto XY plane

(b) At B_i^* = 0°

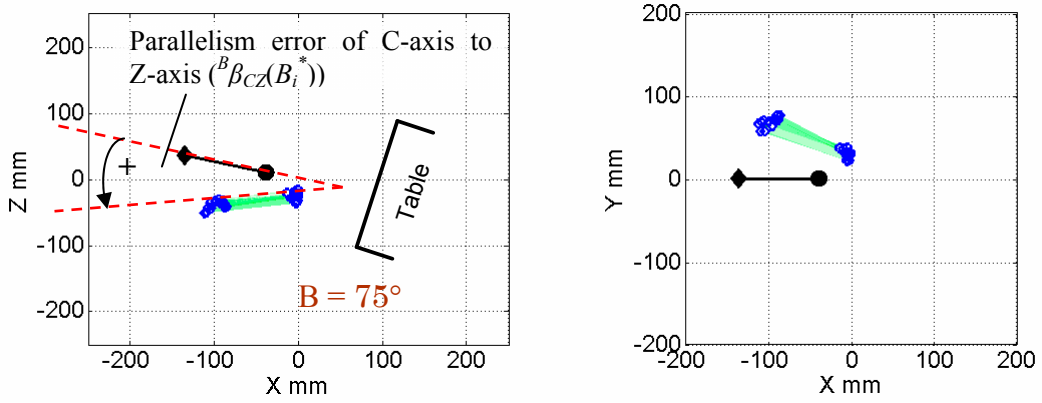

Projection onto XZ plane　　Projection onto XY plane

(c) At B_i^* = 75°

Fig. 3-11 Sensor positions measured by R-test in Setups 2-a (center low) and 2-b (center high), projected onto XZ plane and XY plane.

The measured profile is converted to the reference coordinate system with compensation of "initial resetting", as well as numerical elimination of the influence of offset errors of rotary axis (i.e. $\delta\tilde{x}^0_{CY}$, $\delta\tilde{y}^0_{CY}$ and $\delta\tilde{z}^0_{BY}$), as described in Section 3.3.

Figures 3-9(a) to (c) show measured ${}^r p(B_i^*, C_j^*)$ with full C-rotation (C_j^*=0°,…, 330°) at B_i^* = -75°, 0°, and 75° in Setups 1-a (outer low) and 1-b (outer high). Although an analogous profile is measured at total seven B angular positions (see Section 3.7.1), only three of them are shown. In Fig. 3-9, an error of the measured sensors nest position ("○" marks), ${}^r p(B_i^*, C_j^*)$, calculated by Eq. (3-6) from its command position ("●" marks), denoted by ${}^r q^*(B_i^*, C_j^*)$, given by Eq. (3-1), is magnified 10,000 times. Painted circles represent average circles presented in Section 3.4. "Table" indicates approximate position and orientation of rotary table. Figure 3-10 shows same measured sensors nest position trajectories projected onto the XZ plane and XY plane. Figure 3-11 shows measured sensors nest displacement profiles in Setups 2-a (center low) and 2-b (center high) projected on the XZ plane and XY plane.

3.7.1.3 Observation

The graphical presentation of R-test measurement results presented in Section 3.7.1.2 allows us to make many intuitive observations of error motions of rotary axes. This subsection particularly focuses on observing how error motions of the rotary table (C-axis) changes depending on the swiveling axis (B-axis). For example:

- In Fig. 3-10(b) at B_i^* = 0°, measured trajectories (both upper and lower trajectories) are inclined from their command trajectories around Y-axis. This represents the squareness error of the C-axis average line to the X-axis at B_i^* = 0°. At different B_i^*(see Figs. 3-10(a) to (c)), this squareness error slightly changes, especially at B_i^* = 75°. One of major contributors to these orientation errors is the angular positioning error of B-axis. See Section 3.5

and Section 3.7.2 for further discussion.

- In Fig. 3-11(b) at $B_i^* = 0°$, lines connecting higher and lower trajectories are tilted from the Z-axis around Y-axis. This represents the parallelism error of the C-axis average line to Z-axis at $B_i^* = 0°$ (see Section 3.5 and Section 3.7.2 for further discussion). The parallelism error does not change significantly at different B_i^*(see Figs. 3-11(a) to (c)).

3.7.2 Separation of squareness error of linear axes

By the procedure proposed in Section 3.5, squareness errors of linear axes are identified by comparing R-test results in three setups (i.e. Setups 1-a(outer low), 2-a(center low), and 2-b(center high) as shown in Fig. 3-2).

Figure 3-12(a) shows the squareness error of C-axis average line to the X-axis and Y-axis average line of the B-coordinate system, ${}^B\alpha_{CY}(B_i^*)$ and ${}^B\beta_{CX}(B_i^*)$, calculated at each B_i^* (i=1~7) from the orientation of the average circle of measured R-test profiles in Setup 1-a (outer low) shown in Fig. 3-10 (see Section 3.5(1)).

Figure 3-12(b) shows the orientation error of C-axis average line to the Z-axis average line of the B-coordinate system, ${}^B\alpha_{CZ}(B_i^*)$ and ${}^B\beta_{CZ}(B_i^*)$, calculated at each B_i^* (i=1~7) from the orientation of the line connecting the center gravity of the measured R-test profiles in Setup 2-a (center low) and that in Setup 2-b (center high) from its nominal direction, as is shown in Fig. 3-11 (see Section 3.5(2)).

By combining Fig. 3-12(a) and 3-12(b) (see Section 3.5(3)), the squareness error of Z-axis to X-axis and Y-axis of the B-coordinate system (denoted by ${}^B\beta_{ZX}(B_i^*)$ and ${}^B\alpha_{ZY}(B_i^*)$ (i=1, …, N_b)) can be calculated, and is shown in Fig. 3-12(c) (lines with ♦ and ● marks, respectively).

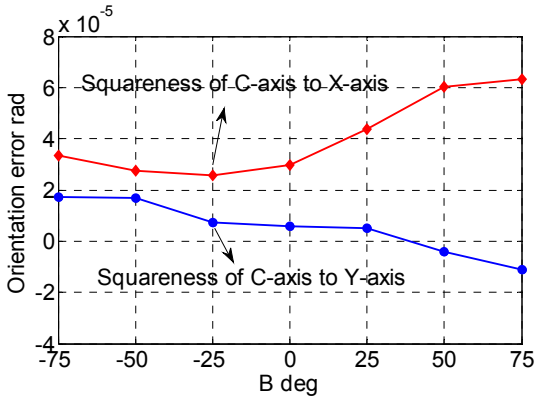

(a) Squareness of C-axis to X-axis and Y-axis of the B-coordinate system at each B_i^*, identified from the measured profile in Setup 1-a (outer low)

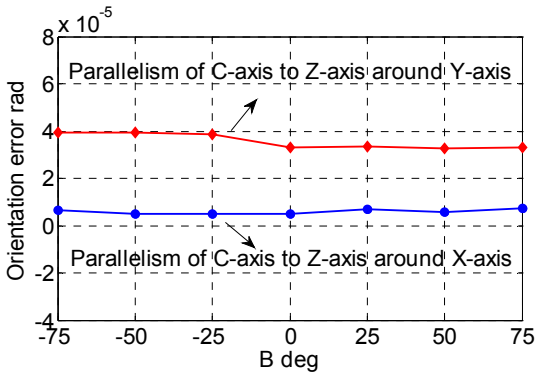

(b) Parallelism of C-axis to Z-axis of the B-coordinate system at each B_i^*, identified from measured profiles in Setups 2-a (center low) and 2-b (center high)

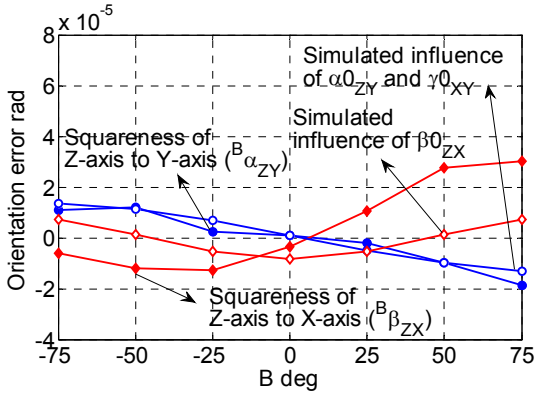

(c) squareness of Z-axis to X- and Y-axes of the B-coordinate system calculated from (a) and (b) and the influence of squareness errors of linear axes (i.e. $\hat{\alpha}^0_{ZY}$, $\hat{\beta}^0_{ZX}$, and $\hat{\gamma}^0_{XY}$)

Fig. 3-12 Orientation error of C-axis in the B-coordinate system from measured R-test profiles in Figs. 3-10 to 3-11, and separation of the squareness errors of linear axes.

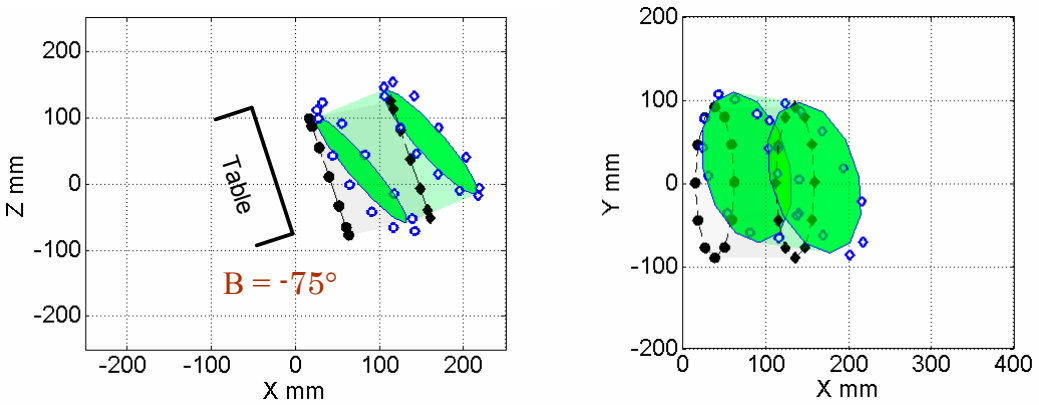

Projection onto XZ plane　　Projection onto XY plane

(a) At B_i^* = -75°

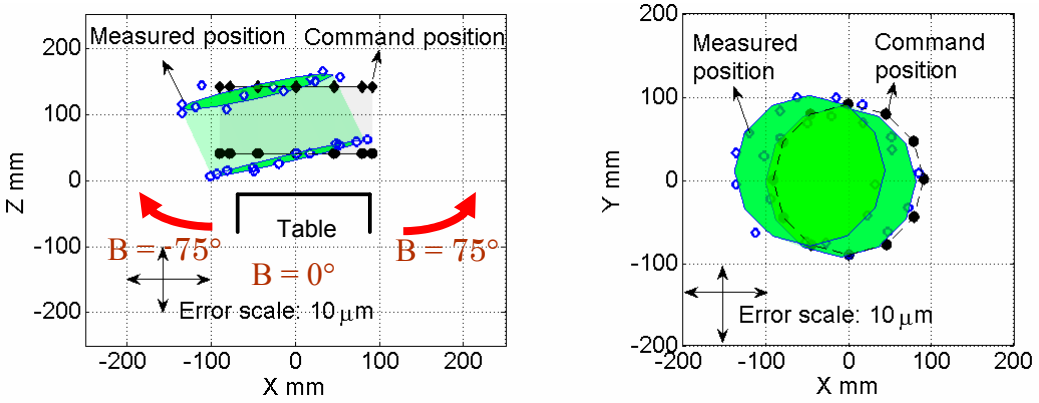

Projection onto XZ plane　　Projection onto XY plane

(b) At B_i^* = 0°

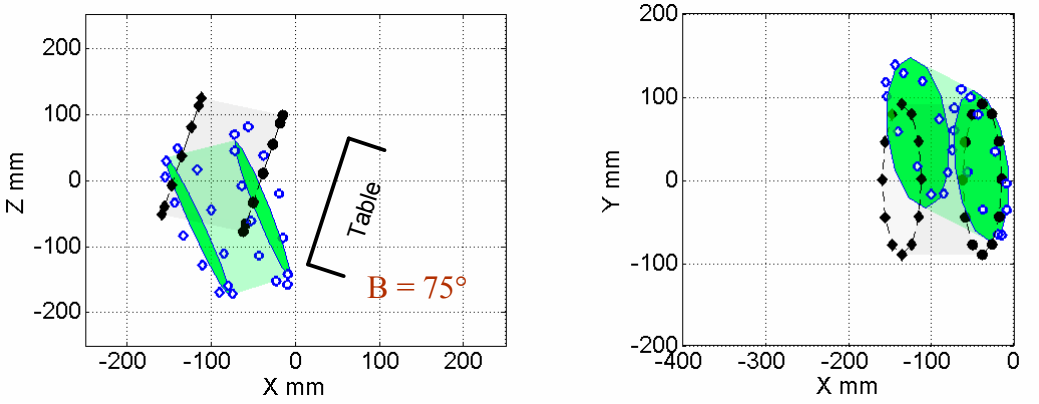

Projection onto XZ plane　　Projection onto XY plane

(c) At B_i^* = 75°

Fig. 3-13 Sensor positions measured with R-test after eliminating the influence of estimated squareness errors of linear axes (i.e. $\hat{\alpha}^0_{YZ}$, $\hat{\beta}^0_{XZ}$, and $\hat{\gamma}^0_{YX}$) (Setups 1-a (outer low) and 1-b (outer high)).

The squareness errors of linear axes (i.e. ${}^{0}\alpha_{YZ}$, ${}^{0}\beta_{XZ}$, and ${}^{0}\gamma_{YX}$) is estimated from Eqs. (3-9) and (3-10), as mentioned in Section 3.5(4). From the measurement result shown in Fig. 3-12(c), the following results are obtained: $\hat{\alpha}^{0}_{YZ} = -0.1\times10^{-5}$ rad; $\hat{\beta}^{0}_{XZ} = -0.8\times10^{-5}$ rad; and $\hat{\gamma}^{0}_{YX} = 1.4\times10^{-5}$ rad.

The influence of identified squareness errors (i.e. $\hat{\alpha}^{0}_{YZ}$, $\hat{\beta}^{0}_{XZ}$, and $\hat{\gamma}^{0}_{YX}$) on the squareness error of Z-axis to X- and Y-axes of the B-coordinate system, calculated by Eqs. (3-9) and (3-10), is also shown in Fig. 3-12(c) (lines with ◇ and ○ marks, respectively).

Figure 3-12(c) shows that the measured profile of ${}^{B}\hat{\alpha}_{ZY}(B_i^*)$ matches well with the simulated one with $\hat{\alpha}^{0}_{YZ}$ and $\hat{\gamma}^{0}_{YX}$. On the other hand, the measured profile of ${}^{B}\hat{\beta}_{ZX}(B_i^*)$ does not match with the simulated one with $\hat{\beta}^{0}_{XZ}$. This suggests that the Z-X squareness error in the reference coordinate system is not constant at different X-positions (i.e. the assumption in Section 3.5-(4) is not met). This may be caused by the pitch error motion of X-axis. As a result, we conclude that, the estimated Z-X squareness error, $\hat{\beta}^{0}_{XZ}$, contains large estimation error (the Z-X squareness error can not be represented by a single position-independent parameters).

3.7.3 Identification of geometric errors associated with B-axis

As was discussed in Section 3.6, if the machine meets the assumption that squareness errors are the same at any X positions, squareness errors of linear axes can be estimated as demonstrated above. In this particular experimental machine, this assumption was not satisfied, especially for X and Z axes.

(1) Separation of squareness errors of linear axes

By the algorithm proposed in Section 3.6, error motions of B-axis observed by R-test are numerically parameterized as position-dependent geometric errors.

First, the influence of the squareness errors of linear axes, ${}^{w}\hat{\bar{q}}^{s}(B_i^*, C_j^*)$, estimated by Eq. (3-14) in Section 3.6.2 is numerically eliminated from the R-test

measurement result of Setup 1-a (outer low), as mentioned in Section 3.6. The sensor positions (Setups 1-a (outer low) and 1-b(outer high)) after eliminating the influence of $\hat{\alpha}^0_{YZ}$, $\hat{\beta}^0_{XZ}$, and $\hat{\gamma}^0_{YX}$, i.e. ${}^w\overline{q}(B_i^*, C_j^*) - {}^w\hat{\overline{q}}^s(B_i^*, C_j^*)$, are shown in Fig. 3-13.

Original R-test profiles shown in Fig. 3-10 contain the influence of both rotary and linear axes error motions. In Fig. 3-13, the influence of squareness errors of linear axes is removed. It should be emphasized that the influence of other error motions of linear axes, e.g. straightness errors or linear positioning errors, still remains. Since the R-test measures only the relative displacement of the rotary table (driven by rotary axes) to the spindle-side sphere position (driven by linear axes), it is in principle not possible to completely eliminate the influence of linear axes. However, in practical applications, squareness of linear axes are often dominant error factors on the volumetric error in the three-axis kinematics.

Comparing Fig. 3-13 with Fig. 3-10, we can find that both trajectories, with and without the influence of squareness errors of linear axes, do not differ much (the maximum difference in measured sensor position is about 1.5 μm). In this particular application example, it suggests that the influence of squareness errors of linear axes on R-test profiles is not significant.

As was discussed in Section 3.7.2, we found that the estimated Z-X squareness error, $\hat{\beta}^0_{XZ}$, had a large estimation error. The analysis presented in this subsection nevertheless used this estimate, with a primal interest in demonstrating the proposed scheme presented in Section 3.6.2.

(2) Identification of location errors

Location errors were estimated by Eq. (3-16) in Section 3.6.3. The identified location errors are listed in Table 3-2.

(3) Identification of position-dependent geometric errors associated with B-axis

Identification of position-dependent geometric errors associated with B-axis was conducted by Eq. (3-22) in Section 3.6.4. The identified

position-dependent geometric errors of B-axis are shown in Fig. 3-14. This can be seen as an "error map" of B-axis.

Table 3-2 Identified location errors

Symbol	Value (μm)	Symbol	Value ($\times 10^{-5}$ rad)
δx^0_{BY}	-7.8	α^0_{BY}	1.8
δy^0_{BY}	12.1	β^0_{BY}	4.1
δz^0_{BY}	-38.0	γ^0_{BY}	0.8

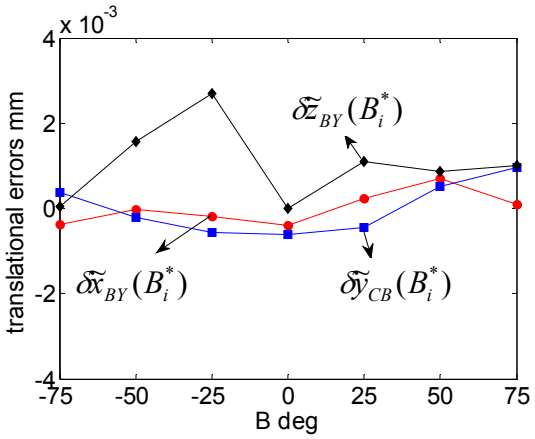

(a) $\delta\tilde{x}_{BY}(B_i^*), \delta\tilde{y}_{CB}(B_i^*), \delta\tilde{z}_{BY}(B_i^*)$

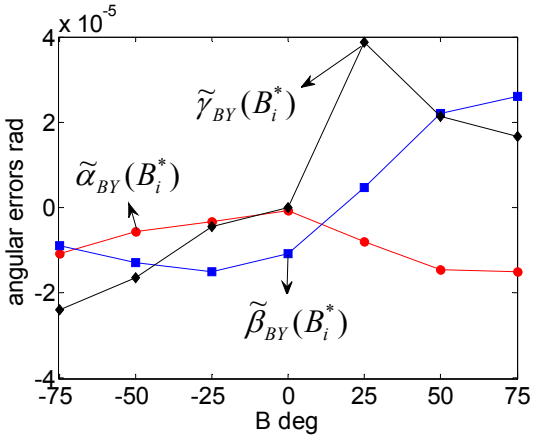

(b) $\tilde{\alpha}_{BY}(B_i^*), \tilde{\beta}_{BY}(B_i^*), \tilde{\gamma}_{BY}(B_i^*)$

Fig. 3-14 Identified position-dependent geometric errors of the rotary table dependent on B-axis angular position.

(4) Observations

a. Location errors (i.e. position-independent terms) as listed in Table 3-2, suggest that static center offsets of B- and C-axes average lines from their nominal positions (i.e. δx^0_{BY}, δy^0_{BY}, and δz^0_{BY}), as well as constant angular positioning error ,β^0_{BY} (about 4×10^{-5} rad (≈ 8 arcsec)), are dominant for this experimental case.

b. All of previous R-test works reviewed in Section 1.2 focused only on the identification of location errors. As can be clearly seen by comparing Table 3-2 and Fig. 3-14, location errors (in Table 3-2) only represent the "average" of error motions observed in Fig. 3-14. For example, when tilt error motions of B-axis, parameterized by $\tilde{\alpha}_{BY}(B_i^*)$ and $\tilde{\gamma}_{BY}(B_i^*)$, vary significantly with the B-rotation as can be observed in Fig. 3-14(b), their "average" values do not have much significance. This illustrates a major contribution of this chapter.

c. Axial error motion of B-axis, i.e. the variation in observed $\delta\tilde{y}_{CB}(B_i^*)$ with the B-rotation, is not significant (about 1μm).

d. Radial error motion of B-axis, i.e. the variation $\delta\tilde{x}_{BY}(B_i^*)$ and $\delta\tilde{z}_{BY}(B_i^*)$ with the B-rotation, was observed. However, the radial error motion of B-axis (i.e. "run-out", see Fig. 2-7(b) in Section 2.3.1.2) is only about ±1 μm (peak-to-peak), which is not significant compared to the measurement uncertainty of the R-test device.

e. Tilt error motion of B-axis, i.e. $\tilde{\alpha}_{BY}(B_i^*)$ and $\tilde{\gamma}_{BY}(B_i^*)$, was observed. Tilt error motion of B-axis, or "coning" (see Figs. 2-7(c) in Section 2.3.1.2), is about $\pm3\times10^{-5}$ rad (peak-to-peak).

3.8 Conclusion

Compared to ball bar measurements [Abbaszaheh-Mir, 2002, Kakino, 1994, Tsutsumi, 2003], the R-test has a strong potential advantage in its applicability to high-efficient, fully-automated calibration of error motions of rotary axes on five-axis machine tools.

A graphical presentation method of R-test measurements was presented in this chapter. Experimental results intuitively clarified how error motions of rotary table changes depending on the B-angle.

This chapter compares two R-test setups where the sphere is away from or on the nominal C-axis average line. By combining both measurements, the directional relationship of C-, Z- and X- (or Y-) axes can be obtained at each B-angle. Under a certain assumption, squareness between X-axis, Y-axis, and Z-axis could be estimated, in addition to orientation errors of the C-axis average line at each B-angle.

An algorithm to numerically parameterize position-dependent geometric errors of B-axis is proposed in this chapter. The experimental case study shows that 1) static center offsets of B- and C-axes average lines from their nominal positions (i.e. δx^0_{BY}, δy^0_{BY}, and δz^0_{BY}) are the significant error factors, 2) however, angular positioning error of B-axis (i.e. $\beta_{BY}(B)$) , as well as tilt error motion of B-axis, (represented by $\alpha_{BY}(B)$ and $\gamma_{BY}(B)$) are also observed in this experimental case.

Chapter 4
Observation of thermal influence on error motions of rotary axes by static R-test

4.1 Introduction

As was reviewed in Section 1.2, many researchers have recently reported a calibration scheme of kinematic errors in a five-axis machine tool. However, an evaluation method of thermal influence on the five-axis kinematics is rarely found in the literature. Among many error sources in machine tool kinematics, thermal errors can be one of dominant error factors under extended usage of the machine [Ramesh, 2000, Schwenke, 2008].

ISO 230-3 and ISO 10791-10 [ISO 230-3, 2007, ISO 10791-10, 2007] describe tests to evaluate thermal distortions on machine tools caused by rotating spindle and reciprocating motion of linear axes. For the application to a five-axis machine tool, these standards have the following issues:

1) No test is described in these standards on the thermal influence on a rotary axis.
2) The tests described in these standards, such as the measurement of thermal distortions due to moving X-axis shown in Fig. 4-1 (described in ISO 230-3 [ISO 230-3, 2007]), only measure thermal influence on the TCP (tool center position) and its orientation, and do not evaluate thermal influence on *error motions* of an axis.
3) In serial-link kinematics, error motions of one axis are often affected by those of the axis on which it is mounted on. For example, in the tilting rotary table configuration (see Fig. 2-5 in Section 2.3), where a rotary table (C-axis) is installed on a swiveling axis (B-axis), error motions of C-axis are often influenced by the angular position of B-axis, due to e.g. the gravity-induced deformation. The thermal deformation may change this dependency of C-axis error motions on the B-axis angular position. No tests

described in ISO 230-3 and 10791-10 can see such an influence.

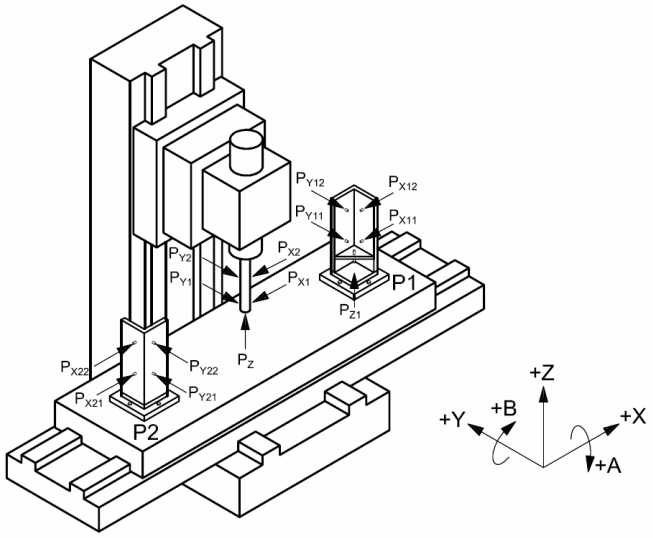

Fig. 4-1 The set-up for measurement of thermal distortions due to moving X axis table of machining centre. [ISO 230-3, 2007]

4.2 Objective and original contribution of this chapter

The objective of this research is to propose a method to observe the influence of thermal distortions on error motions of a rotary axis in five-axis kinematics by R-test measurement.

To intuitively observe geometric errors of rotary axes, a graphical presentation of displacement profiles measured by R-test was proposed in Section 3.4. An algorithm to identify not only location errors, but also position-dependent component errors of rotary axes with static R-test, was proposed in Section 3.6. The measurement and analysis scheme presented in this chapter is a straightforward application of these approaches to thermal tests.

4.3 Test procedure

(1) Reciprocating motion of a rotary axis

In the proposed thermal test, thermal influence caused by a servo motor of a rotary axis will be investigated. First, the rotary axis to perform reciprocating motion to generate the heat must be chosen. In our test, since the deformation of

the swiveling B-axis may significantly influence error motions of the rotary table, B-axis is naturally selected to be the reciprocating axis. The B-axis performs a reciprocating movement. Note that other axes (i.e. linear axes and C-axis) are stopped within the B-axis reciprocating motion. At the given time interval, the reciprocating motion of B-axis is interrupted and the following R-test measurement cycle is conducted.

(2) R-test measurement procedure

At given time interval, this B-axis reciprocating motion is interrupted, and the R-test measurement cycle with Setup 1-a (outer low), as shown in Fig. 3-1 and Fig. 3-2(a), is conducted. See Section 3.3.1 for details on the R-test measurement cycle.

4.4 Analysis of R-test profiles

4.4.1 Graphical presentation of R-test profile

For more intuitive understanding of rotary axes error motions, the measured R-test profile is graphically displayed by the procedure presented in Section 3.4.

4.4.2 Error parameters of the rotary table to be identified

The location and orientation of axis of rotation may vary due to its rotation (i.e. position-dependent geometric errors described in Section 2.3.1.2). Moreover, as was discussed in [Srivastava, 1995], the thermal distortions can be modeled by geometric errors that vary with the time. The position-dependent geometric errors of B-axis, listed in Table 4-1, represent position and orientation errors of the *C-axis* (rotary table) *average line* at each B angle. In other words, they represent how the C-axis rotates at each B-angle. The algorithm therefore targets numerical parameterization of these parameters, as already described in Section 3.6.

In Chapter 3, total four R-test cycles are conducted with different sphere locations. In this test, only one R-test cycle is performed at each measurement

interval. This is simply because it is not possible to perform multiple R-test cycles at a measurement interval. As the result, the present scheme mainly targets the observation of the thermal influence on the B-axis error motions.

Table 4-1 Description of geometric errors of a rotary table

Symbol	Description
$\delta x_{BY}(B, t)$	Location changes of B-axis of rotation in X-direction depending on B-angle and time t.
$\delta y_{CB}(B, t)$	Location changes of the rotary table's axis of rotation in Y-direction depending on B-angle and time t.
$\delta z_{BY}(B, t)$	Location changes of B-axis of rotation in Z-direction depending on B-angle and time t.
$\alpha_{BY}(B, t)$	Orientation changes of B-axis of rotation around X-axis depending on B-angle and time t.
$\beta_{BY}(B, t)$	Angular positioning error of B-axis of rotation depending on B-angle and time t.
$\gamma_{BY}(B, t)$	Orientation changes of B-axis of rotation around Z-axis depending on B-angle and time t.

4.4.3 Calibration procedure of geometric errors of the rotary table

From each R-test profile measured at the given time interval, location errors and position-dependent geometric errors are numerically identified. Its detailed algorithm is presented in Section 3.6.

4.5 Case study

4.5.1 Experimental setups

In this experiment, the R-test sensors nest is installed at ${}^{w}q^{*}$ = [-0.448 mm, -91.187 mm, 40.567 mm]^{T} in the workpiece coordinate system (defined in Section 2.3), as shown in Fig. 4-2. Five thermocouple sensors (sheathed type) are attached on the locations shown in Fig. 4-2 for roughly correlating calibrated geometric errors and thermal distribution.

The machine is cold-started. Then, the B-axis keeps swiveling between -90° and -60° by the angular velocity of 5,000 degree/min. At every 15 minutes, this B-axis reciprocating motion is interrupted, and the R-test measurement cycle is conducted with the following command B and C angular positions:

B_i^* = -60°, -30°, …, 60° (i=1,…,5)

C_j^* = 0°, 72°, …, 288° (j=1,…,5)

Total 5×5 = 25 points are measured. Figure 4-3 shows command X^*, Y^*, Z^*, B^*, and C^* trajectories for an R-test measurement cycle. One R-test measurement cycle for 25 points takes within 2 minutes including the setup time in this experimental case.

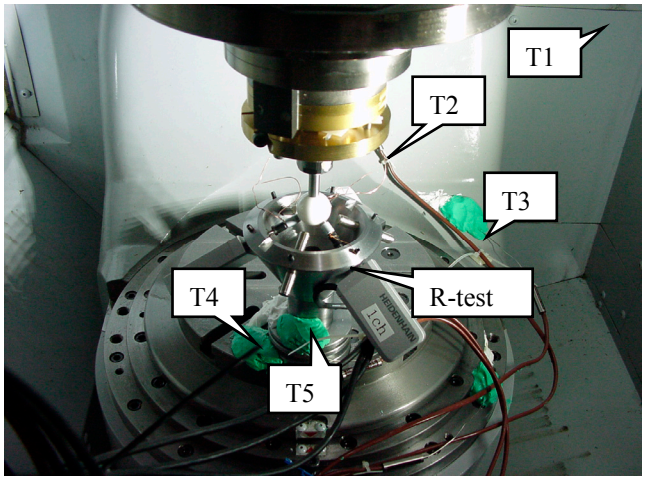

Fig. 4-2 Setup of R-test and thermocouple sensors (T1: thermocouple sensor for ambient temperature; T2: on the B-axis cover near B-axis center; T3: on the cover near bridge between B-shaft and C-table; T4: on C-table; T5: on R-test).

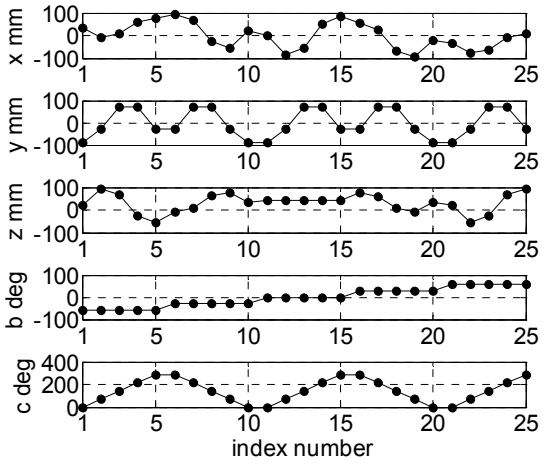

Fig. 4-3 Command X, Y, Z, B, and C positions for each R-test measurement cycle.

4.5.2 Measured temperatures

Figure 4-4 shows measured temperatures throughout this experiment, continued for about 3 hours. Observations can be made as follows:

- The temperature on the B-axis cover near B-axis center (T2) rose by 1.4 °C. Note that the thermo couple sensor T2 is attached to the B-axis cover, not the B-axis motor directly, simply because we are not allowed to dismount the cover. The temperature of the B-axis motor itself was not measured.
- The temperature rise on the cover near the bridge between B-shaft and C-table (T3) was about 0.7 °C. The temperature rise on the C-table (T4) was not observed. It suggests that the transfer of the heat caused by reciprocating motion of B-axis to the surface of rotary table was sufficient small.
- Throughout this experiment, the change in the ambient temperature (T1) and the temperature of R-test device (T5) was within 0.5 °C.

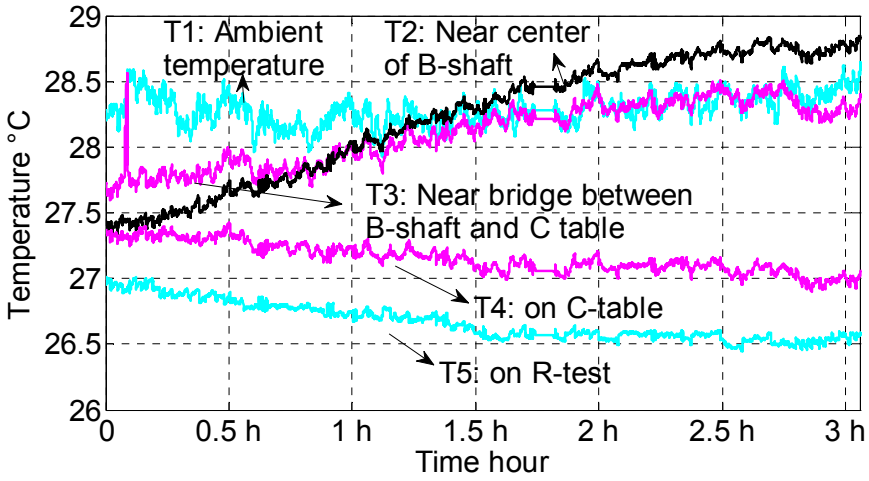

Fig. 4-4 Measured temperature by thermal couple sensors.

To see the causal connection of reciprocated motions and temperature rise, as well as error motions of rotary axes, we have conducted another experiment in different conditions of reciprocating B-axis motion. In this test, the B-axis was swiveled between -15° to 15° in 5,000 deg/min. Compared to the present test (-90° to -60° in 5,000 deg/min), the temperature rise of the B-shaft was significantly smaller. In the present test, the B-axis motor outputs significantly larger torque due to the gravity influence. By comparing these two tests, we

reasonably conclude that temperature rise observed in Fig. 4-4, as well as the change in error motions presented in the following subsection, is caused mainly by the B-axis reciprocating motion.

4.5.3 Graphical presentation of R-test profile

(1) Test results

The R-test profile measured at each test intervals, ${}^{w}\overline{q}(B_i^*, C_j^*)$ (i = 1~5, j = 1~5), is transformed to the reference coordinate system, denoted by ${}^{r}p(B_i^*, C_j^*)$ as is presented in Section 3.4. Sensor position profiles measured at 0, 1, and 2 hours from the beginning of the test (denoted by time t = 0h, 1h, 2h) are shown in Figs. 4-5(a) to (c) in the three-dimensional view. Although the R-test cycle was conducted at total 11 times in 3 hours, only three profiles (t = 0h, 1h, 2h) are shown to simplify the plot. Note that an error of measured positions (○) from its command position (●) is magnified 8,000 times.

Figures 4-5(a), (b), and (c) present sensor position profiles measured with C-rotation (C_j^* = 0° to 288°) at B_i^* = -60°, 0°, 60°, respectively. In each plot, three painted circles represent the average circle fit to measured sensor positions for t = 0h, 1h, and 2h. These average circles are shown to help easier understanding of position and orientation of the C-axis average line (see Fig. 3-4 in Section 3.4). “Table” shows rough position of the rotary table. Figures 4-6(a) to (c) show their projection onto the XY plane and XZ plane.

It is to be noted that the static axis shift of B-axis in Z-direction at the start of this series of measurements (i.e. t = 0h) is numerically eliminated from the R-test profile in these plots, since it is typically caused by the miscalibration of tool length and thus is not regarded as the machine’s error motions (see Section 3.4). The change with time in this axis shift of C-table to the Z-direction is shown. These plots clearly show the position and the orientation of C-axis average line at each B_i^*, and how they changes with the time proceeds.

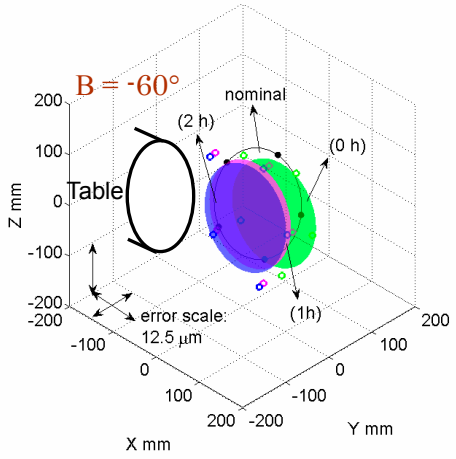

(a) $B^{\tilde{}} = -60°$

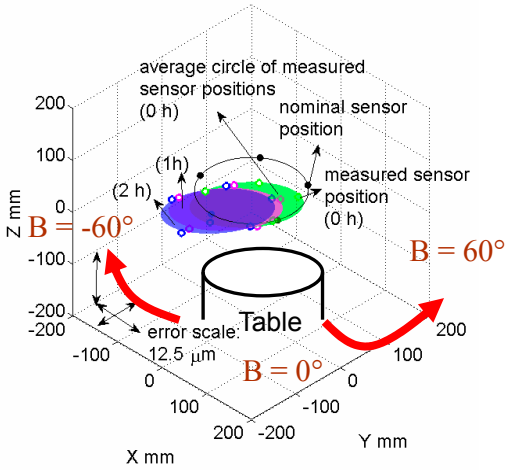

(b) $B^{*} = 0°$

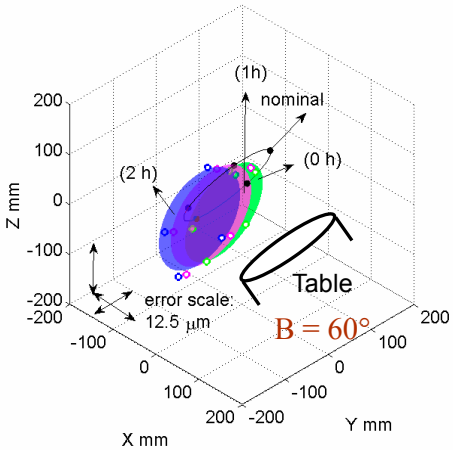

(c) $B^{*} = 60°$

Fig. 4-5 Sensor positions measured by R-test in the reference coordinate system with C-rotation at B_i^{*} = -60°, 0°, 60°. An error of measured sensor positions (○) from its command positions (●) is magnified 8,000 times.

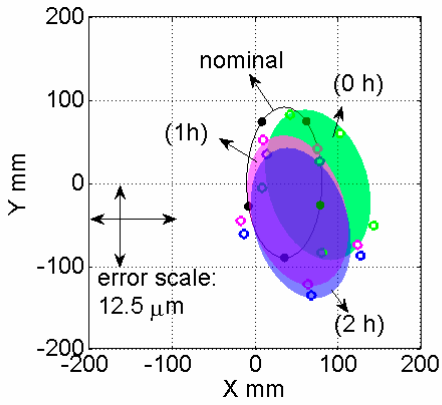

Projected on XY plane

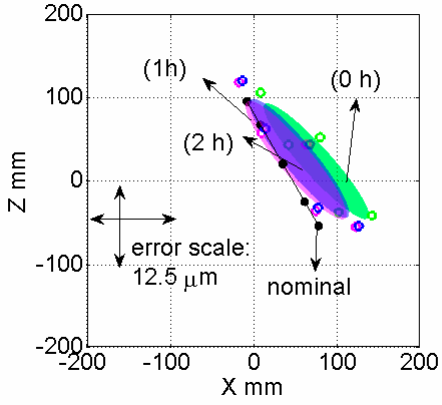

Projected on XZ plane

(a) B^* = -60°

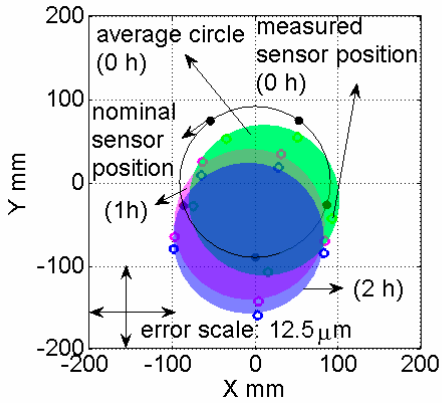

Projected on XY plane

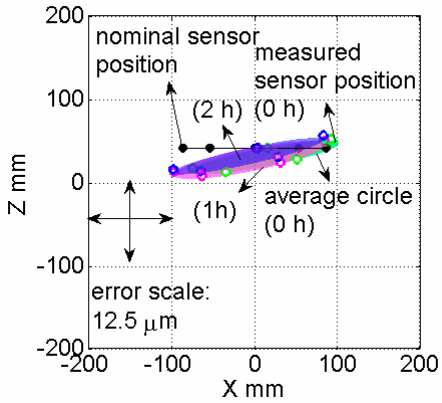

Projected on XZ plane

(b) B^* = 0°

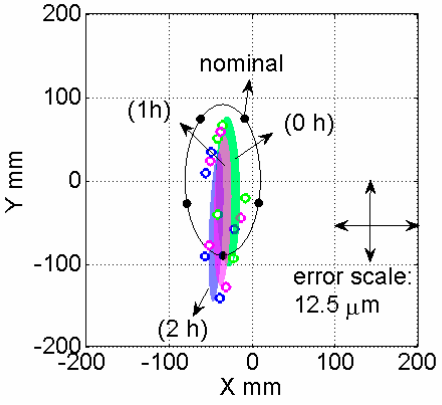

Projected on XY plane

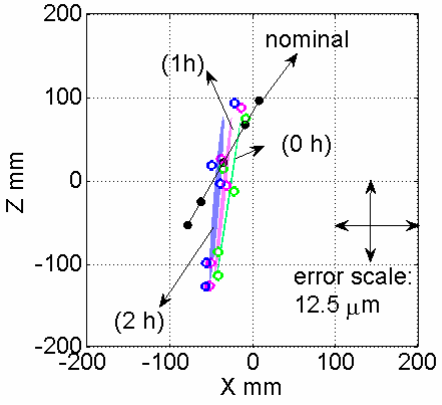

Projected on XZ plane

(c) B^* = 60°

Fig. 4-6 Sensor positions measured by R-test in the reference coordinate system with C-rotation at B_i^* = -60°, 0°, 60°, projected onto XY plane and XZ plane.

(2) Observation

Observations can be made as follows:

a. In projection on XY plane of Figs. 4-6(a) to (c), measured sensor positions move to (-X, -Y) direction as time proceeds (about -2 μm to X-direction and -6 μm to Y-direction in 3 hours). It suggests that the temperature rise gradually shifted the position of the axis average line of C-axis.

b. In projection on XZ plane at B = 0° (Fig. 4-6(b)), gradual shift of measured trajectories to the Z-direction can be observed, although it is significantly smaller than the shift to the Y-direction. In this machine, the influence of heat by the B-axis motion mainly affects the rotary table position in the Y-direction, rather than in X- or Z-directions.

c. In projection on XZ plane of Fig. 4-6(b), measured sensor positions are tilted from the nominal trajectory around the Y-axis. As already discussed in Section 3.4, this suggests the squareness error of the C-axis average line to the X-axis, which can be caused by the angular positioning error of B-axis at $B = 0°$. This orientation error of measured profiles is larger at B = 60° (in projection on XZ plane in Fig. 4-6(c)). This represents larger B-axis angular positioning error at $B = 60°$ relative to that at $B = 0°$, which could be also observed from projection on XY plane of Fig. 4-6(c). A slight change in this angular positioning error with the temperature rise can be observed, although it is not significantly large.

In this analysis, the influence of squareness errors of linear axes is not removed, unlike the case presented in Sections 3.3 to 3.6. This is because: 1) the influence of squareness errors of linear axes is, in this experimental machine, sufficiently small compared to error motions of rotary axes, as shown in Fig. 3-12. 2) It is not possible to evaluate the thermal influence on error motions of linear axes, since it is not possible to conduct multiple R-test cycles with different sphere positions at each test interval. Therefore, the observations above assume that error motions of linear axes are sufficiently small, and thus errors observed in Figs. 4-5 and 4-6 are caused by rotary axis error motions only. When

this assumption is not met, error profiles are influenced by not only error motions of rotary axes, but also those of linear axes. In the present thermal test, however, it can be reasonably assumed that the heat transfer to linear axes is limited (see Section 4.5.2) and thus the thermal influence on their error motions is sufficiently small.

4.5.4 Calibration of geometric errors of the rotary table

(1) Test results

From the R-test results presented in Section 4.5.3, the position and the orientation of C-axis average line at each B_i^* can be calculated. Six geometric error parameters of the rotary table, shown in Table 4-1, can be parameterized essentially from the position and the orientation of "average circles" of measured sensor positions shown in Fig. 4-5 and 4-6. Figures 4-7(a) to (f) show how calibrated geometric error parameters change with the time proceeds.

(2) Observation

The identification results shown in Fig. 4-7 tell that:

a. The gradual shift of the rotary table in X-, and Y-direction observed in the previous subsection is parameterized by a gradual change in δx_{BY} and δy_{CB} in Figs. 4-7(a) and (b).

b. From the identified result δz_{BY} shown in Fig. 4-7(c), a gradual shift of the Z-position of B-axis centerline is also observed (about -2 μm in 3 hours) as time proceeds.

c. Compared to the measurement uncertainty of the R-test device (estimated to be about 2μm [Weikert, 2004]), the influence of thermal distortion of machine tool on the tilt error motion of B-axis (i.e. α_{BY}, β_{BY}, and γ_{BY}) in Figs. 4-7(d) to (f) is relatively small, which could also be observed from Figs. 4-5 and 4-6. However, a slight change of the tilt error motions of B-axis was identified, particularly on the tilt error motion around Z-axis (γ_{BY}).

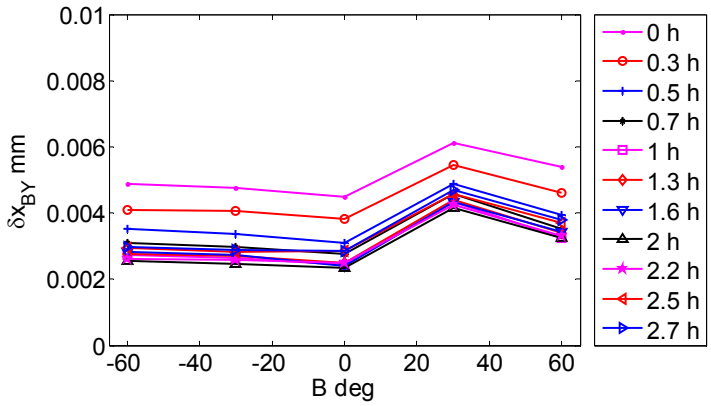

(a) δx_{BY}

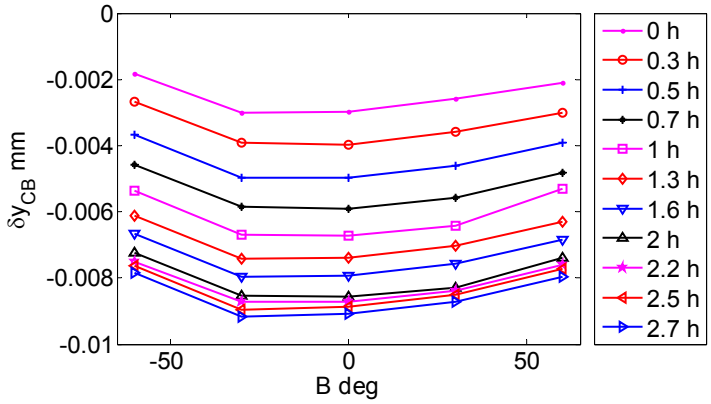

(b) δy_{CB}

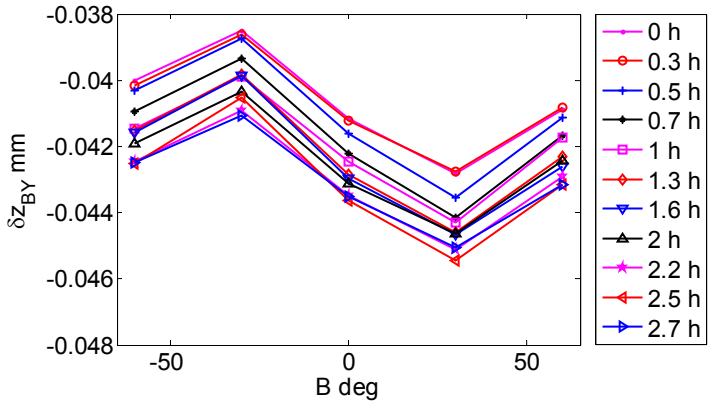

(c) δz_{BY}

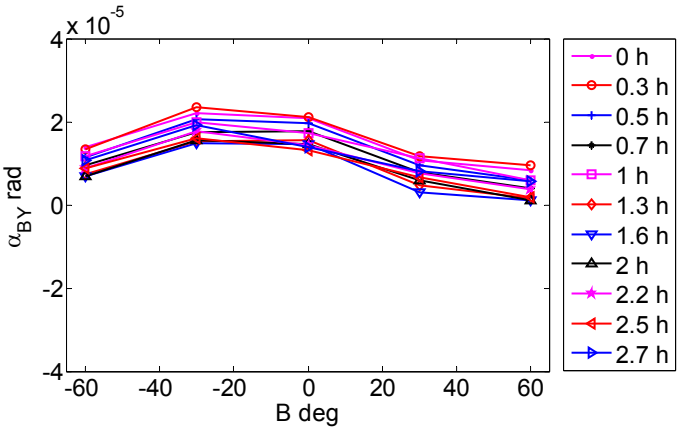

(d) α_{BY}

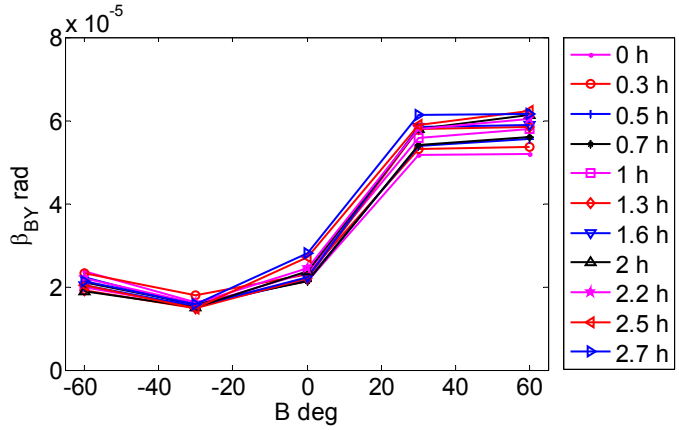

(e) β_{BY}

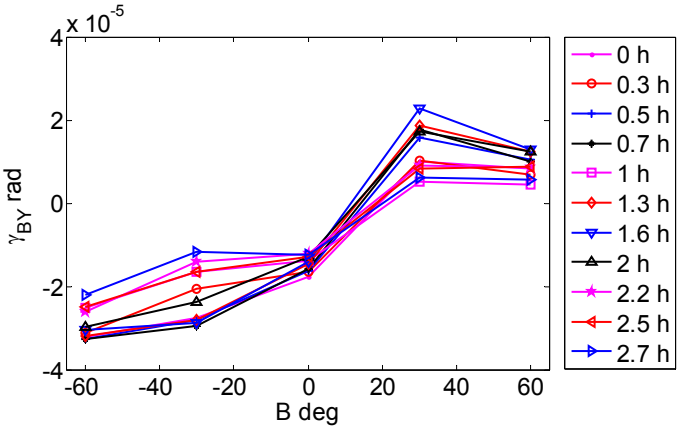

(f) γ_{BY}

Fig. 4-7 Calibrated geometric errors of the rotary table at each time interval (See Table 4-1 for definition of error parameters).

4.6 Conclusion

By introducing an approach proposed in Section 3.4 and Section 3.6, calibration method of thermally induced geometric errors of C-axis caused by reciprocating movements of B-axis was proposed in this section.

Its experimental application example was demonstrated. The present thermal test clarifies how error motions of the rotary table change with the time proceeds. From experimental results, the following observations are made:

(1) Temperature rise of B-shaft mainly caused a gradual position shift of C-axis average line. Such a shift may potentially cause significant geometric errors of the finished workpiece by five-axis machining, as will be demonstrated for an example of the cone frustum machining test in Chapter 6.

(2) R-test results clarified the orientation error of C-axis average line varying with B-rotation due to reciprocated motion of B-axis. A slight change on this tilt error motion was observed, particularly on the tilt error motion around the Z-axis, which is potentially caused by the thermal influence of B-axis.

(3) By comparing with analogous test results under the condition where the B-axis motor generates smaller heat, it can be observed that the observed change in error motions is caused mainly by the heat generated by the B-axis motor, although this causal connection is not proved in this experiment.

Chapter 5
Non-contact R-test for dynamic measurement on five-axis machine tools

5.1 Introduction

Chapter 3 and 4 presented the application of the conventional R-test device to the measurement of static error motions of rotary axes. Similarly, as was reviewed in Section 1.2, most of the researches in the literature focused on error calibration on five-axis machine tools in static R-test measurement [Weikert, 2004, Bringmann, 2006 Ibaraki, 2011, Zargarbashi, 2009]. Note that "static" measurement means the measurement under the condition that the machine tool keeps still when logging the measurement data. On the other hand, a "dynamic" measurement is defined as a measurement that is conducted when the machine tool is driven with a velocity.

All the conventional R-test devices, including commercially available ones [IBS, Fidia], use contact-type linear displacement sensors with a flat-ended probe. When flat-ended probes are contacted with the sphere, the three-dimensional position of the sphere center can be calculated by a simple formula [Weikert, 2004, Bringmann, 2006, Ibaraki, 2011] from measured displacements by using pre-calibrated direction vectors of linear displacement sensors only (see Section 2.2.2). However, the influence of friction between probes and the sphere, or the dynamics of a spring supporting probes, could potentially impose significant influence on the measured displacement, particularly in dynamic measurements. Furthermore, the safety of measurement, avoiding the crash caused by e.g. mis-programming, can be a critical issue with the contact-type R-test. Therefore, a non-contact R-test has potentially significant advantages particularly for dynamic measurement on five-axis machine tool.

5.2 Objective and original contribution of this chapter

As was reviewed in the previous section, all the conventional R-test

devices [Weikert, 2004, IBS, Fidia, Ibaraki, 2009] use contact-type displacement sensors. The objective of this chapter is to construct a non-contact type R-test with laser displacement sensors, particularly for dynamic measurement on five-axis machine tools. As a non-contact displacement sensor, we employ a laser displacement sensor for its longer reference distance and larger measurement range than other non-contact sensors, such as capacitive and inductive displacement sensors.

Potential inherent advantages of applying non-contact displacement sensors to the R-test include:

1) The measurement is not affected at all by the friction on the sphere surface and probes.
2) The measurement is not affected at all by the dynamics of a supporting spring in contact-type displacement sensors.
3) The measurement is safer due to longer working distance between the sphere and sensors.

When a non-contact displacement sensor is used, or when the sensor does not touch the sphere with a flat surface, e.g. sphere-ended probes, the offset of the sphere center from the line representing the sensor's sensitive direction could introduce an error for calculating the three-dimensional displacement of the sphere when the conventional algorithm for contact-type R-test is used (see Section 5.4.1 for further details). A new algorithm for calculating three-dimensional displacement of sphere with non-contact displacement sensors should be proposed.

Another critical issue with the application of a laser displacement sensor to the non-contact R-test is its measurement uncertainty due to the inclination of the target surface. When the sensor's sensitive direction is off the center of the sphere, the target surface, where the laser spot hits, is inclined from the sensor's sensitive direction, which often results in the measurement error. An appropriate laser displacement sensor should be chosen, whose measurement uncertainty is less sensitive to the inclination of the target surface. Furthermore, such a measurement error must be numerically compensated from measured

displacement profiles.

For this end, the contribution of this chapter can be summarized as follows: 1) a profile measurement of a sphere by using laser displacement sensors with different measuring principles is conducted to investigate the measurement uncertainty due to the inclination of the target surface (Section 5.3); 2) an algorithm to calculate three-dimensional displacement of the sphere center for non-contact R-test is proposed (Section 5.4); 3) a model to interpolate the measurement error of the non-contact type R-test measurement is proposed. The compensation with the estimated measurement error is also conducted to improve the measurement accuracy with the non-contact R-test (Section 5.5); 4) a prototype non-contact R-test is developed. Case studies, including a static measurement and a dynamic measurement by the developed non-contact R-test device, are conducted to evaluate its measurement performance by comparing the measurement results with the contact-type R-test device (Section 5.6).

5.3 Selection of laser displacement sensor for non-contact R-test

5.3.1 Objective

Laser displacement sensors generally exhibit the best measurement performance when the measured surface is placed normal to the sensor's sensitive direction. Therefore, when measuring a sphere surface, the measurement uncertainty is supposedly minimized when the sensor is directed exactly to the sphere center. When the sphere center is shifted from there, the measured surface becomes tilted from the sensor's sensitive direction, and as a result, the measurement uncertainty is expected to increase.

The measurement uncertainty mentioned above is expected to be significantly dependent on the measuring principle. For the application to a non-contact R-test, it is crucial to select an appropriate type of laser displacement sensor that has the measurement uncertainty less sensitive to the inclination of the target surface. Meanwhile, it is also important to have larger measuring range and smaller noise.

Several laser displacement sensors with different measuring principle are

available in today's market. This section experimentally investigates the measurement uncertainty of four laser displacement sensors with different measuring principle when they are applied to measure a sphere surface.

For a non-contact R-test device, it is favorable to select the displacement sensor with the following properties:

(1) Larger "measurable" area on a sphere surface can be obtained. In this chapter, "measurable area" represents the area perpendicular to the sensor's sensitive direction where valid reflected laser beam returns to the sensor and the measurement is possible.

(2) The measurement range, defined as the working distance along the sensor's sensitive direction where the measurement is possible, is larger.

(3) The measurement uncertainty caused by the inclination of the target surface, due to the curvature of sphere surface, is smaller.

(4) The noise in the measured profile is smaller. The measurement noise is typically caused by the speckle noise in the laser beam.

5.3.2 Laser displacement sensors used in this study

The investigated laser displacement sensors include spectral interference type (SI-F10 by Keyence), specular reflection type (LK-G10 by Keyence), diffuse reflection type (LK-H052 by Keyence), and confocal type (LT-9010MS by Keyence) [Keyence]. Table 5-1 shows main specifications of the investigated laser displacement sensors. The external views and schematics of the measuring principle are shown in Fig. 5-1.

Table 5-1 Main specifications of laser displacement sensors used in this study [Keyence]

Maker: Keyence	LK-G10	LK-H052	SI-F10	LT-9010MS
Measuring principle	Specular reflection type	Diffuse reflection type	Spectral interference type	Confocal reflection type
Reference distance	10 mm	50 mm	11.3 mm to 12.35 mm	6 mm
Measurement range	±1 mm	± 10 mm		±0.3 mm
Spot diameter (at reference distance)	Φ20 μm	Φ50 μm	Φ40 μm	Φ2 μm

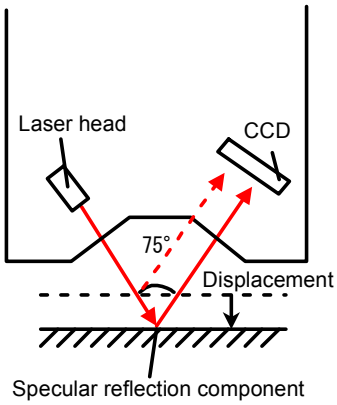

External view Measuring principle

(a) Specular reflection type (LK-G10)

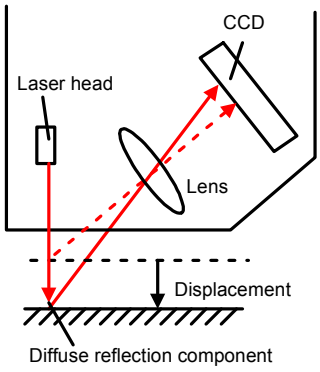

External view Measuring principle

(b) Diffuse reflection type (LK-H052)

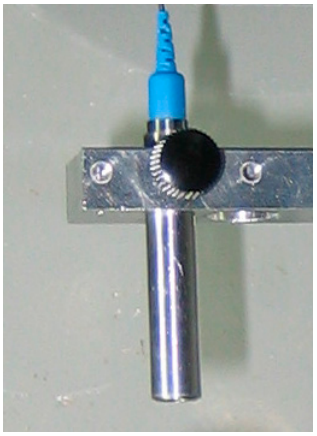

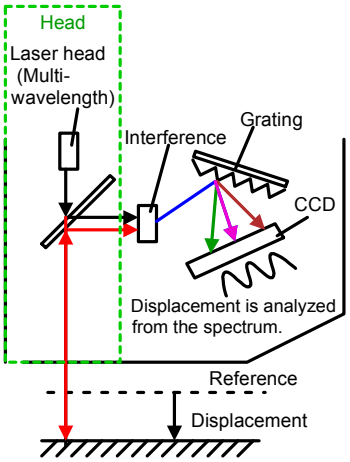

External view Measuring principle

(c) Spectral interference type (SI-F10)

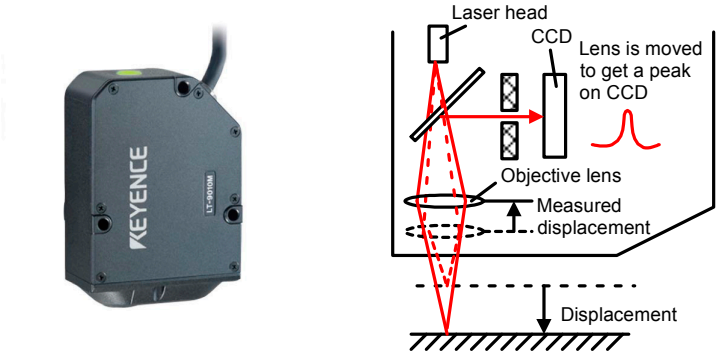

External view Measuring principle

(d) Confocal type (LT-9010MS)

Fig. 5-1 Laser displacement sensors with different measuring principles. [Keyence]

The measuring principles of these four laser displacement sensors are briefly introduced as follows (more detailed information can be found in [Keyence]):

(a) Specular reflection type (LK-G10 by Keyence), and

(b) Diffuse reflection type (LK-H052 by Keyence)

As shown in Figs. 5-1(a) and (b), theses laser displacement sensors focus the laser beam on a target. The target reflects the beam back through the lens where it is focused on a light-receiving element (CCD arrays). By detecting the displacement of the beam spot on the CCD arrays, the target's displacement (in the vertical direction in Figs. 5-1(a) and (b)) can be determined. The surface-reflected laser from a target object consists of a regular reflection and a diffuse reflection component. (a) and (b) accept regular reflection component and diffuse reflection component, respectively.

(c) Spectral interference type (SI-F10 by Keyence)

As shown in Fig. 5-1(c), a target-reflected laser beam with wide wavelength band, interferes with the laser beam from a reference surface. The spectrum of the interfered laser beam is detected by a light-receiving element and analyzed to determine the displacement of the target.

(d) Confocal type (LT-9010MS by Keyence)

As shown in Fig. 5-1(d), a laser beam is focused on a target surface through an objective lens that vibrates up and down at high speed by means of a tuning fork. The beam reflected off the target surface is converged on a pinhole and then enters a light-receiving element. By measuring the exact position of the objective lens when the light enters the receiving element, the target height can be determined.

5.3.3 Experimental investigation of measurement uncertainty of laser displacement sensors for profile measurement of sphere

(1) Test objective

As mentioned in Section 5.3.1, the measurement uncertainty is supposed to increase when the laser displacement sensor's sensitive direction is off the center of the target sphere. Therefore, in this subsection, a test to measure the profile of a sphere with the laser displacement sensor is conducted. By conducting such a test, the measurable area, the measurement uncertainty due to the inclination of the target surface, and the noise when the laser scans the sphere surface (as mentioned in Section 5.3.1), are investigated.

(2) Test procedure

First, the ceramic precision sphere with the radius of 12.7 mm (other specifications are shown in Table 2-2), is attached to the machine spindle. One of four laser displacement sensors in Section 5.3.2 is fixed on the machine table vertically as illustrated in Fig. 5-2. In each test, the sensor is set up such that the position (X, Y) = (0, 0) corresponds to the point where the sensor's sensitive direction approximately points to the sphere center.

Then, for the specular reflection type laser displacement sensor LK-G10 for example (see Fig. 5-3), the machine is moved from X = -0.6 mm to +0.6 mm at Y = -0.6 mm, where the laser displacement is continuously logged. The same scanning operation is repeated at Y = -0.5, -0.4, …, +0.6 mm. Similar scanning test is conducted for each sensor, although the scanning direction, the scanning

range, and the scanning path pitch differ for each sensor.

If the sensor's sensitive direction is exactly pointing to the sphere center at (X, Y) = (0, 0), the measured laser displacement should be the shortest (i.e. maximum value) there. Due to its setup error, this "top" location, as well as the orientation of measured profile, may be shifted from the nominal position and orientation. To cancel the influence of this setup error, the ideal sphere profile is best-fit to the measured profile. The difference of measured profiles from the best-fit ideal sphere is then recalculated. The profile of the measured sphere surface is generated with the nominal X- and Y-position of the sensor.

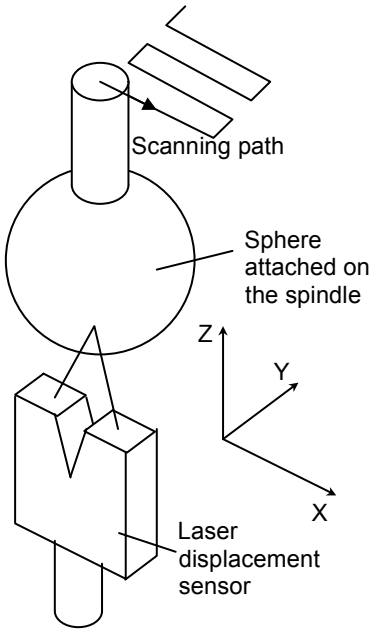

Fig. 5-2 Schematics of the profile measurement of a sphere.

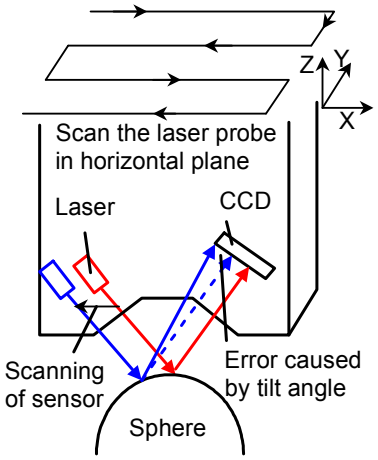

Fig. 5-3 Measurement uncertainty to the inclination of the target surface with specular reflection type laser displacement sensor (LK-G10).

(3) Analysis objective and procedure

As was mentioned before, the measurement uncertainty is supposedly minimized when the sensor's sensitive direction is exactly aligned to the line pointing to the sphere center. As the laser spot moves away from this "top" position on the sphere surface, the measurement uncertainty is expected to increase (see Fig. 5-3. This schematic diagram shows the specular reflection type laser displacement sensor as an example, but similar observation can be made for other sensors). Eventually, as the distance from this "top" position is larger than certain value, the reflected light fails to return to the sensor and thus the measurement fails. Based on test results, we divide the sphere surface depending on the distance from the line pointing to the sphere center as follows:

1) The range where the measurement displacement is sufficient small, i.e. the range that can be regarded as a flat surface (smaller than 1 μm in this study);
2) The range where the profile measurement error is smaller than the defined tolerance;
3) The range where the profile measurement error is larger than the defined tolerance;
4) The range where the measurement of the sphere profile fails.

Note that the profile measurement error is defined as the measured displacement with respect to the nominal sphere geometry. The tolerance is set to be 1 μm in this section. The geometric inaccuracy of the ceramic precision sphere is pre-calibrated to be sufficiently small compared to the sensor's measurement uncertainty.

The main objective of experiments in this section is to find the size of each range (1~4) for each of four different laser displacement sensors presented in Section 5.2. Naturally, the sensor having larger range is preferred for the application to the non-contact R-test.

(4) Test results

Figures 5-4 show the profile measurement result of a sphere with specular reflection type laser displacement sensor (LK-G10). Figure 5-4(a) shows the test setup. Figure 5-4(b) shows measured "raw" profiles of laser displacements plotted with nominal X and Y positions of the sensor. As presented in Section 5.3.3-(2), the nominal sphere profile (also shown in Fig. 5-4(b)) is best-fit to measured profiles. In Fig. 5-4(c), for each of scanning line to the X-direction, the difference in the measured profile from the nominal profile is plotted with nominal X and Y positions. This represents the measurement error, where the influence of the sensor's setup error is removed. This profile is called the profile measurement error. Fig. 5-4(d) shows the projection of profile measurement error in Fig. 5-4(c) along X-direction (all the scanning lines are superimposed). Figures 5-5 to 5-7 are the setup and the profile measurement result with diffuse reflection type laser displacement sensor (LK-H052), spectral interference type laser displacement sensor (SI-F10), and confocal reflection type laser displacement sensor (LT-9010MS), respectively.

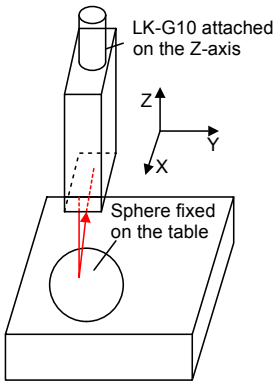

(a) Setup

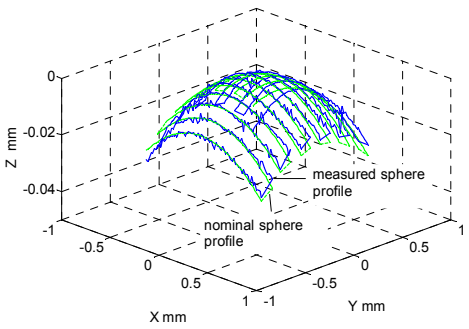

(b) Profile measurement result

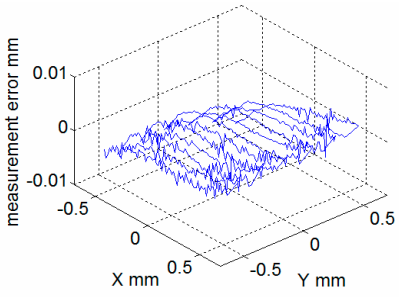

(c) Profile measurement error

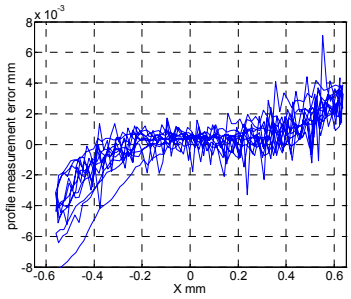

(d) Profile measurement error along X-axis

Fig. 5-4 Profile measurement result of a sphere with specular reflection type laser displacement sensor (LK-G10).

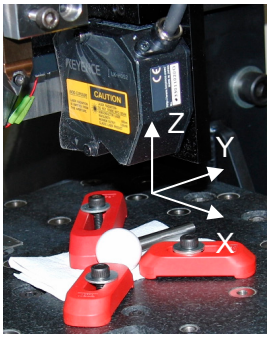

(a) Setup

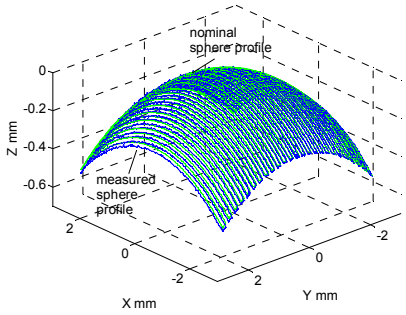

(b) Profile measurement result

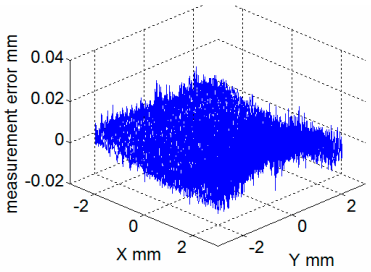

(c) Profile measurement error

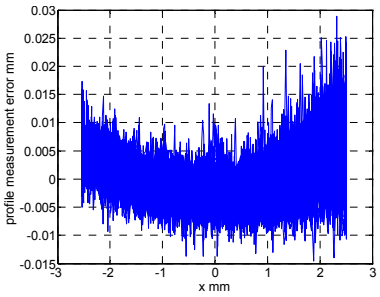

(d) Profile measurement error along X-axis

Fig. 5-5 Profile measurement result of a sphere with diffuse reflection type laser displacement sensor (LK-H052).

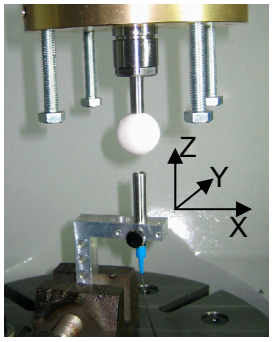

(a) Setup

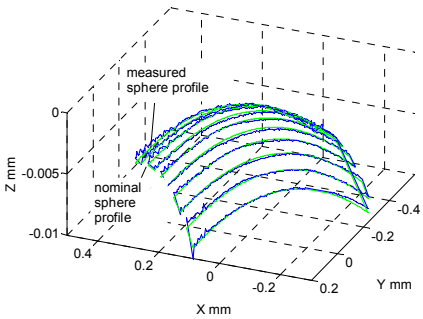

(b) Profile measurement result

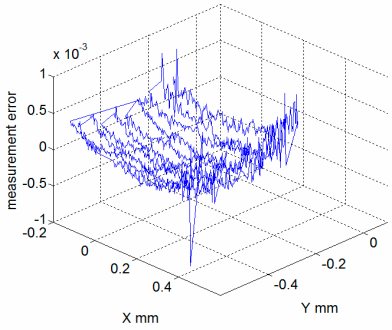

(c) Profile measurement error

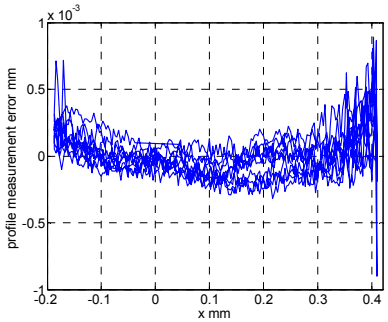

(d) Profile measurement error along X-axis

Fig. 5-6 Profile measurement result of a sphere with spectral interference type laser displacement sensor (SI-F10).

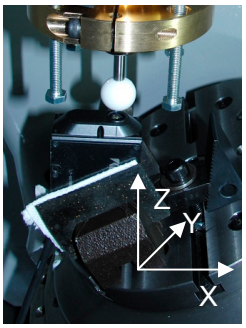

(a) Setup

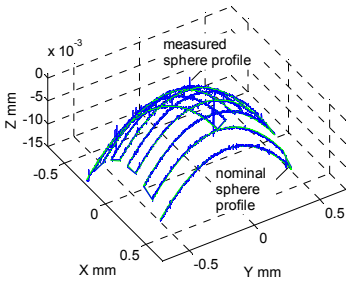

(b) Profile measurement result

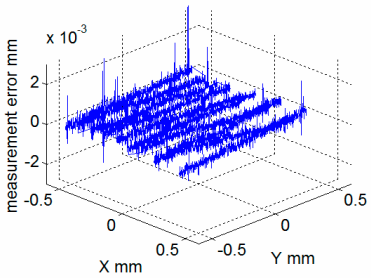

(c) Profile measurement error

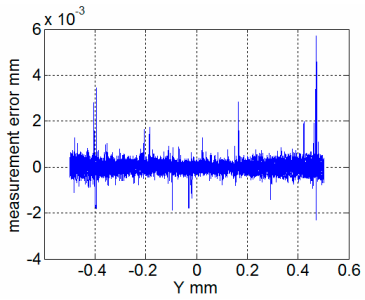

(d) Profile measurement error along X-axis

Fig. 5-7 Profile measurement result of a sphere with confocal type laser displacement sensor (LT-9010MS).

(5) Observations

The following observations can be made for each laser displacement sensor:

1) Specular reflection type (LK-G10, Figs. 5-4)

Since the object is a sphere, the angle of reflection would vary with tilt angle of the normal direction of measured surface with respect to the sensor's sensitive direction, which would cause measurement error (see Figs. 5-4(c) and (d)). When the tilt angle of the normal direction of measured surface with respect to the sensitive direction of laser displacement sensor is reversed, the direction of the measurement error is expected to be reversed.

As can be observed in Figs. 5-4(c) and (d), within the range ±0.5 mm in the XY plane from the sphere top, the average error from the sphere's nominal geometry is within ±3 μm approximately. The higher-frequency variation in measured profiles of the amplitude up to 2 μm is also observed over the entire range, which is likely caused by the speckle noise in laser beam.

2) Diffuse reflection type (LK-H052, Figs. 5-5)

Diffuse reflection type laser displacement sensor (LK-H052 from Keyence) succeeded to measure the widest range of sphere surface (over ±2.5 mm in the XY plane) among the four sensors, while higher-frequency variation is significantly larger (its amplitude is up to 15 μm, as shown in Figs. 5.5(c) and (d)) than other laser displacement sensors, which could be caused by the speckle noise in laser beam. More studies on the measurement uncertainty of this sensor for profile measurement can be found in [Kimura, 2011].

3) Spectral interference type (SI-F10, Figs. 5-6)

Although the spectral interference type laser displacement sensor has smaller measurement area (±0.3 mm), the test result in Figs. 5-6 (b) to (d) shows smallest errors over the range ±0.3 mm (the mean error is within ±0.2 μm). Its higher-frequency component is also the lowest among the four sensors.

4) Confocal type (LT-9010MS, Figs. 5-7)

For confocal type laser displacement sensor, both the profile measurement error (within 1μm in the range ±0.5 mm) and higher-frequency error (within ±0.8 μm) are relatively small among the four sensors. However, occasional spikes, of the amplitude 6 μm at maximum, are observed. This could be caused by the focusing error due to the laser's speckle noise.

The summary of profile measurement results is shown in Table 5-2. Noise level is defined as the standard deviation (1σ) of higher-frequency component in the profile measurement error. Based on measured profiles, the ranges 1) to 3) presented in Section 5.3.3-(3) are evaluated for each sensor. In Table 5-2, "profile measurable area" shows the size of each range in the XY plane with the center at the sphere top.

Specular reflection type laser displacement sensor (LK-G10 by Keyence), which has relatively large measurement range, relatively large measurable area, as well as relatively good measurement performance (i.e. measurement uncertainty and the noise level), is chosen to be the sensor to develop an R-test prototype. The cost of each sensor is also one of reasons for this choice. The price of each sensor is: LK-H052 < LK-G10 < LT-9010MS < SI-F10.

Table 5-2 Profile measurement result of a ceramic sphere with radius of 12.7 mm.

Model	Profile measurable area	Noise level (1σ)
Specular reflection type (LK-G10)	1): ±0.1 mm 2): ±0.3 mm 3): ±0.6 mm	1μm
Diffuse reflection type (LK-H052)	1): ±0.1 mm 2): ±1 mm 3): over ±2.5 mm	5μm
Spectral interference type (SI-F10)	1): ±0.1 mm 2): ±0.3 mm 3): ±0.3 mm	0.1μm
Confocal type (LT-9010MS)	1): ±0.1 mm 2): ±0.3 mm 3): ±1.5 mm	0.5μm

5.4 Construction of algorithm to calculate three-dimensional displacement of sphere center

5.4.1 Difference in algorithms for non-contact and contact-type R-tests

For the conventional R-test, a contact-type linear displacement sensor with flat-ended probes is pushed to being contacted with the sphere. Therefore, its displacement would not be affected by center offset of the sphere in the plane perpendicular to the sensor's sensitive direction (see Fig. 5-8 (a)).

As presented in Section 2.2.2, the algorithm to calculate the sphere center displacement by the conventional contact-type R-test is reviewed as follows: Figure 5-9 shows the measurement setup of conventional contact-type R-test (re-posted from Fig. 2-2). A precision sphere is attached to the spindle of test machine. Three displacement sensors (i = 1, 2, 3) are installed on the table (Fig. 5-9 only shows one displacement sensor). The origin of the coordinate system, $O_0 = (0, 0, 0)^T$, is defined at the sphere center in its initial position. The unit direction vector $V_i = (u_i, v_i, w_i)^T$ (i = 1, 2, 3) represents the sensitive direction of the i-th displacement sensor. The displacement of sphere center, $O_j = (O_{jx}, O_{jy}, O_{jz})^T$ (j = 1, ..., N), can be calculated as follows (see Section 2.2.2):

$$\begin{bmatrix} O_{jx} & O_{jy} & O_{jz} \end{bmatrix} = \begin{bmatrix} d_{1j} & d_{2j} & d_{3j} \end{bmatrix} \cdot \begin{bmatrix} u_1 & u_2 & u_3 \\ v_1 & v_2 & v_3 \\ w_1 & w_2 & w_3 \end{bmatrix}^{-1} \tag{5-1}$$

where d_{ij} (i = 1, 2, 3; j = 1, ..., N) denotes the measured displacement of the i-th displacement sensor when the sphere center is moved from O_0 to O_j. It suggests that when three displacement sensors touch the sphere from different directions, the three-dimensional displacement of the sphere center can be calculated from pre-calibrated direction vectors and measured displacements of three probes only.

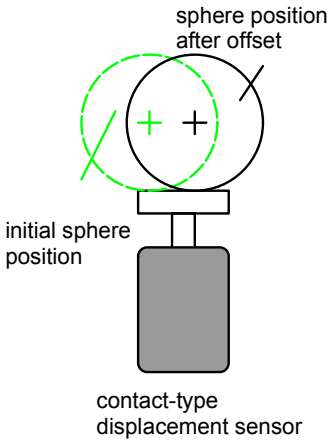

(a) By contact-type displacement sensor with flat-end probe

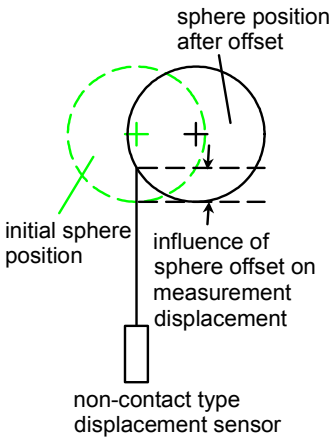

(b) By non-contact displacement sensor

Fig. 5-8 Influence of sphere center's offset on the measured displacement with contact-type displacement sensor and with non-contact type displacement sensor.

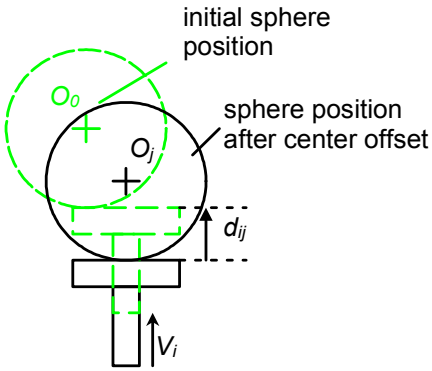

Fig. 5-9 Measurement setup of conventional contact-type R-test. [Ibaraki, 2009]

However, for the case of a non-contact R-test, the measured displacement of the probe changes when the sphere center is shifted perpendicular to the sensitive direction of laser displacement sensor (see Fig. 5-8 (b)). It suggests that an error would be introduced by the center offset of sphere when the conventional algorithm for contact-type R-test is used. Note that, although Zargarbashi and Mayer [Zargarbashi, 2009] have proposed a non-contact measurement device named 'Cap-test' with capacitance displacement sensors, the algorithm used for calculating the three-dimensional displacement of sphere seemed the same with the algorithm used in conventional R-test. To eliminate the influence of center shift illustrated in Fig. 5-8 (b), a new algorithm for calculating three-dimensional displacement of sphere with non-contact displacement sensors should be proposed.

5.4.2 Algorithm to calculate three-dimensional displacement of sphere center

Figure 5-10 shows the measurement principle of a non-contact R-test. A precision sphere with the radius R is attached to the spindle of test machine. Three laser displacement sensors (i = 1, 2, 3), which are installed on the table, are roughly directed to the sphere center. The origin of the coordinate system, O_0 = $(0, 0, 0)^T$, is defined at the sphere center in its initial position; the orientation of the coordinate system is defined based on the machine coordinate system [Schwenke, 2008]. The unit direction vector $V_i = (u_i, v_i, w_i)^T$ (i = 1, 2, 3)

represents the sensitive measurement direction of the corresponding laser displacement sensor. The intersection point of the line representing i-th sensor's sensitive direction and the sphere surface at the initial position is defined as $P_{i0} = (x_{i0}, y_{i0}, z_{i0})^{\mathrm{T}}$ (i = 1, 2, 3). When the sphere center is positioned at $O_j = (O_{jx}, O_{jy}, O_{jz})^{\mathrm{T}}$ (j = 1, ..., N), the intersection moves to $P_{ij} = (x_{ij}, y_{ij}, z_{ij})^{\mathrm{T}}$ (i = 1, 2, 3). d_{ij} (i = 1, 2, 3; j = 1, ..., N) denotes the measured displacement of the i-th laser displacement sensor when the sphere center is moved from O_0 to O_j.

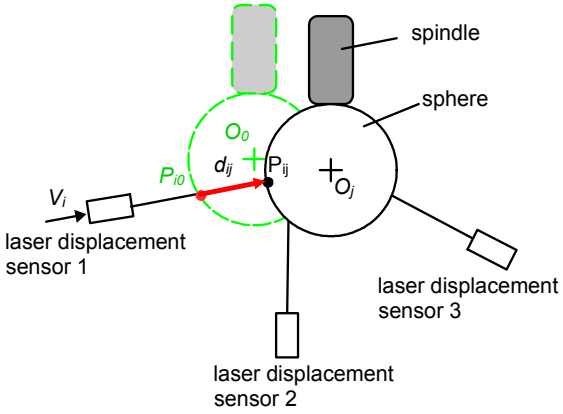

Fig. 5-10 Measurement setup of non-contact R-test with three laser displacement sensors.

Equations (5-2) represent the relationship between the displacement of laser displacement sensors and the position of the sphere center:

$$\begin{cases} P_{ij} = P_{i0} + d_{ij} V_i \\ \left\| P_{ij} - O_j \right\|^2 = R^2 \end{cases} \tag{5-2}$$

The procedure to calculate the three-dimensional position of the sphere center, O_j, with non-contact R-test is shown as follows:

(1) Calibration of parameters of each sensor

Similarly as the conventional contact-type R-test (see Section 2.2.2), the direction vector of each sensor, V_i (i = 1, 2, 3), must be pre-calibrated in the machine coordinate system. However, the estimation of the sphere center, O_j, from laser displacements, d_{ij} (i = 1, 2, 3), requires not only the orientation of each sensor's sensitive direction, V_i, but also intersection points when the sphere

is at the initial position, represented by P_{i0} (i = 1, 2, 3). This is an essential difference in algorithms for contact-type and non-contact R-tests.

The calibration procedure of parameters mentioned above is shown as follows:

(a) Perform the same calibration cycle presented in Section 2.2.2-(2). Position the sphere center at given reference positions, O_j (j = 1, ..., N), within the measurement volume;

(b) Assuming that the machine's positioning error at O_j is sufficiently small, calibrate P_{i0} and V_i of each laser displacement sensor separately (i = 1, 2, 3), from O_j (j = 1, ..., N) and measured laser displacements d_{ij} (j = 1, ..., N) by solving the following minimization problem:

$$\min_{P_{i0},V_i} \sum_{j=1,\ldots,N_1} \left(\left\| P_{i0} + d_{ij} \cdot V_i - O_j \right\| - R \right)^2 \tag{5-3}$$

where equality constraints $||P_{i0}|| = R$, $||V_i|| = 1$ (i = 1, 2, 3) are applied.

(2) Estimation of sphere center displacement from laser displacements

Once the direction vector of each sensor, V_i (i = 1, 2, 3), as well as its position, represented by P_{i0} (i = 1, 2, 3), is calibrated, the three-dimensional displacement of sphere center, O_j (j = 1, ..., N_2), can be calculated from measured laser displacements, d_{ij} (i = 1, 2, 3), by solving the following minimization problem:

$$\min_{O_j} \sum_{i=1,2,3} \left(\left\| P_{i0} + d_{ij} \cdot V_i - O_j \right\| - R \right)^2 \tag{5-4}$$

Both Eq. (5-3) and Eq. (5-4) can be solved with the nonlinear least square method [Matlab, 2002].

5.4.3 Experimental verification of the proposed algorithm

(1) Test objective and procedure

The objective of this subsection is to experimentally investigate estimation accuracy of the sphere displacement by the proposed algorithm in Section 5.4.2. The procedure of experiments is listed as follows:

Identification of sensor parameters:

(a-1) The spindle-side sphere is positioned at total 9 positions given in Section 2.2.2-(2). The interval of each point, l in Section 2.2.2-(2), is different for each sensor (since the measurable range of each sensor is different). In Fig. 5-11, the center point and 8 corner points are command positions.

(a-2) The displacements of laser displacement sensors at 9 positions (the center position and the 8 corner positions) are used to calibrate V_i and P_{i0} (i = 1, 2, 3) with Eq. (5-3).

Estimation of sphere positions:

(b-1) Then, the spindle-side sphere is positioned at total 27 points (9 points above are included) within the same cubic volume as shown in Fig. 5-11.

(b-2) By using calibrated V_i and P_{i0} (i = 1, 2, 3), the sphere center position for each commanded position is calculated from measured displacements, d_{ij}, by Eq. (5-4).

(b-3) Estimated positions of sphere center are plotted by magnifying the error vector from commanded positions.

Note that, a ceramic precision sphere with radius of 12.7 mm is used (see Table 2-2 of Section 2.2.3 for details).

(2) Test result

Same tests are conducted with four sensors presented in (1). The estimated positions of sphere center for each of four laser displacement sensors are shown in Fig. 5-11. The error scale is shown in each plot in Fig. 5-11, respectively.

The machine's positioning error is assumed to be sufficiently small compared to measurement uncertainty. Then, errors of identified positions from command positions observed in Fig. 5-11(a) to (d) can be seen as estimation errors of non-contact R-tests. Table 5-3 summarizes the estimation error of sphere positions of the conducted static R-test measurements. 'mean' represents mean value of norm of measurement errors within the 27 positions and 'std' represents standard deviation (1σ) of norm of measurement errors. The test is

conducted for 3 times. The ‘repeatability’ in Table 5-3 shows the maximum deviation of norm of measurement error within any two tests.

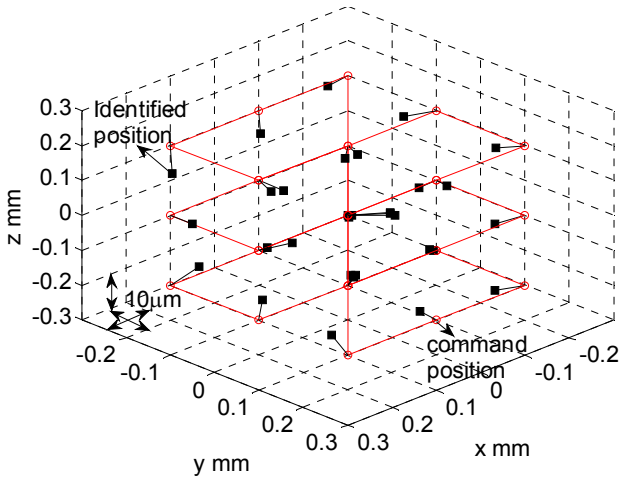

(a) With specular reflection type (LK-G10)

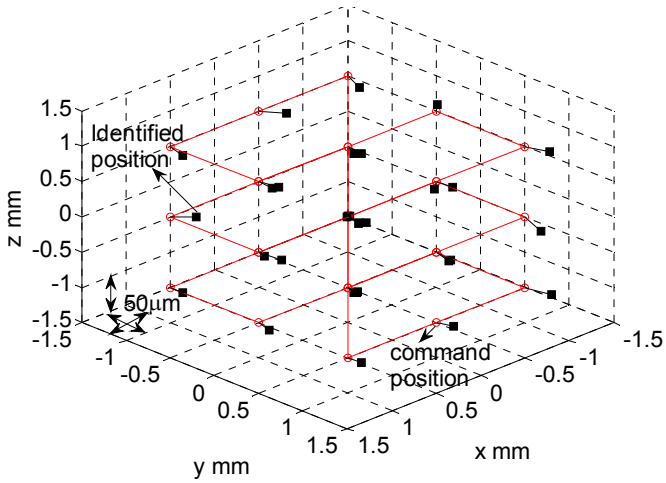

(b) With diffuse reflection type (LK-H052)

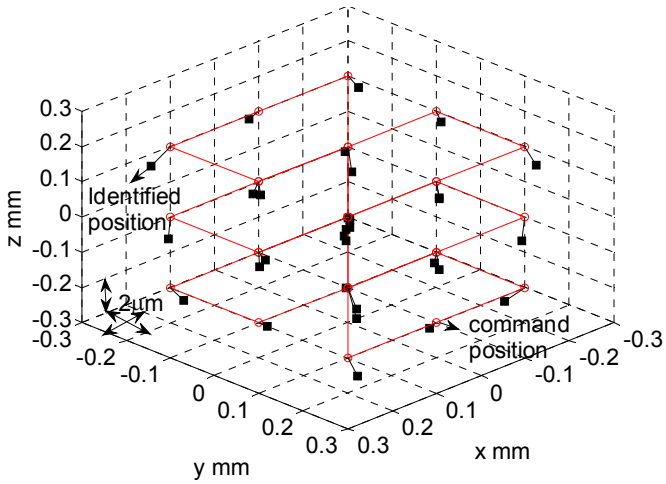

(c) With spectral interference type (SI-F10)

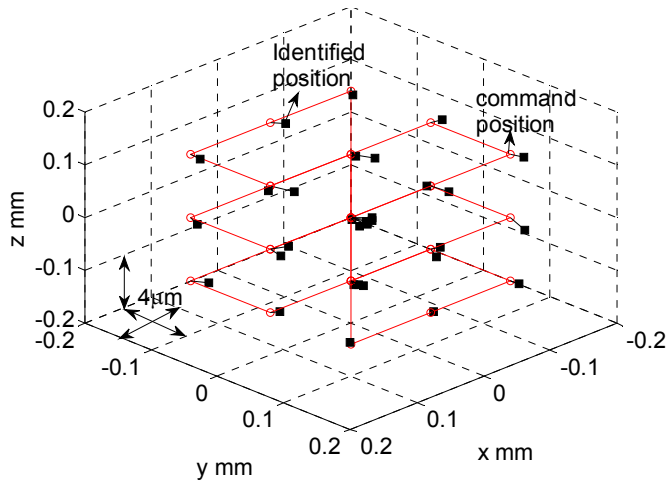

(d) With confocal type (LT-9010MS)

Fig. 5-11 Commanded and identified position of sphere center in a static R-test measurement.

Similar tests are conducted with different measurement volumes (e.g. X0.24 mm×Y0.24mm×Z0.24 mm for LK-G10), although plots of measurement errors are not shown. All the test results are summarized in Table 5-3. For some sensors, only a part of these measurement volumes are tested, due to the limitation in measurable area (see Section 5.3.3-(3)). For example, the measurement volume 2×2×2 mm is tested only for LK-H052. Note that Fig. 5-11 only shows one of these tests for each sensor.

Table 5-3 Profile measurement error (mean, std) and repeatability of sphere displacement in a static R-test measurement.

	Measurement volume (mm^3)	LK-G10 (μm)	LK-H052 (μm)	SI-F10 (μm)	LT-9010 MS(μm)
Measurement error (mean, std)	within 0.24^3	(2.4, 0.9)		(0.8, 0.3)	(0.8, 0.3)
	within 0.4^3	(4.7 , 2.3)	(12.9, 7.1)	(1.0, 0.4)	
	within 2^3		(14.3, 6.5)		
Repeatability	within 0.24^3	0.5		0.1	0.8
	within 0.4^3	0.5	4.1	0.3	
	within 2^3		6.1		

(3) Observation

From Table 5-3, spectral interference type laser displacement sensor (SI-F10 by Keyence) and confocal type laser displacement sensor (LT-9010MS by Keyence) exhibit smallest measurement errors (both in the mean and the standard deviation) among the tested laser displacement sensors, although the measurable volume by these two sensors is smaller (within 0.4^3 mm^3 for SI-F10, within 0.24^3 mm^3 for LT-9010MS). Diffuse reflection type laser displacement sensor (LK-H052 by Keyence) can measure the largest volume (over 2^3 mm^3), while the measurement error is significantly larger both in the mean and the standard deviation than other types of laser displacement sensors. Specular reflection type laser displacement sensor (LK-G10 by Keyence), has relatively large measurable area as well as relatively good estimation performance compared to LK-H052.

5.5 Compensation scheme of the measurement error caused by laser displacement sensor

5.5.1 Objective

As was presented in Section 5.4.3, when specular reflection type laser displacement sensor (LK-G10) is used, the estimation error of sphere displacement is 4.7 μm in average within 0.4×0.4×0.4 mm. This is significantly large compared to the target measurement accuracy. From test results shown in Section 5.4.3 (Fig. 5-11(a) for LK-G10), it is reasonably concluded that the measurement uncertainty to the inclination of the target surface is the critical error factor for this estimation error of sphere center, since the proposed algorithm did not consider this influence.

Moreover, Table 5-3 shows that the measurement results of sphere center with the proposed algorithm exhibit good repeatability compared to the machine's positioning repeatability. For LK-G10, the repeatability of the norm of the three-dimensional measurement error is below 1 μm, as shown in Table 5-3. It suggests that the measurement accuracy of sphere center can be improved, when the measurement error due to the curvature of sphere surface is

compensated.

The objective of this section is to propose its compensation scheme. The overall estimation accuracy of the non-contact R-test with the proposed compensation scheme will be experimentally investigated in Section 5.6.

5.5.2 Interpolation of the measurement error with RBF Network

A radial basis function (RBF) network is an artificial neural network that uses radial basis functions (such as the function shown in Eq. (5-7)) as activation functions. The RBF Network is typically used in such applications as function approximation, time series prediction, and control, especially when the analytical formulation of the problem is hard.

In this section, the RBF Network is used as a three-dimensional look-up table to interpolate the measurement error of non-contact R-test. General schematic of the RBF Network is shown in Fig. 5-12. In our application, at each nominal sphere center position (denoted by $x^*(i) \in \Re^3$), the measurement error by the non-contact R-test, denoted by $b_i(\hat{x}(i)) \in \Re^3$ (i = 1,..,M), is the output of the RBF Network, as shown in Eq. (5-5). Note that $\hat{x}(i) \in \Re^3$ represents the estimated sphere center position of $x^*(i)$ by the algorithm proposed in Section 5.4.2, and is the input to the RBF Network.

In the RBF Network [Seshagiri, 2000], a weight matrix $w_{ij}(\hat{x}(i)) \in \Re^3 (j$ = 1,…,N) and radial basis functions $\varphi_{ij}(\hat{x}(i)) \in \Re^3$ are together used to describe the measurement error $b_i(\hat{x}(i))$ (i = 1,..,M) as in Eq. (5-6). The radial basis function, as shown in Eq. (5-7), represents the three-dimensional displacement of the sphere center position $x^*(i)$ from another position, $x^*(j)$ (j = 1,…,N), in the measurement volume. However, since the nominal sphere center position (i.e. $x^*(i)$) is not known, the estimated sphere center position $\hat{x}(i)$ replaces the nominal position $x^*(i)$, assuming the estimated $\hat{x}(i)$ is close enough to the nominal $x^*(i)$.

$$b(\hat{x}(i)) = x^*(i) - \hat{x}(i)(i = 1,...,M) \tag{5-5}$$

$$\sum_{j=1}^{N} \varphi_{ij}(\hat{x}(i)) w_{ij}(\hat{x}(i)) = b_i(\hat{x}(i)) (i = 1,...,M) \tag{5-6}$$

$$\varphi_{ij}(\hat{x}(i)) = \hat{x}(j) - \hat{x}(i) (j = 1,...,N) \tag{5-7}$$

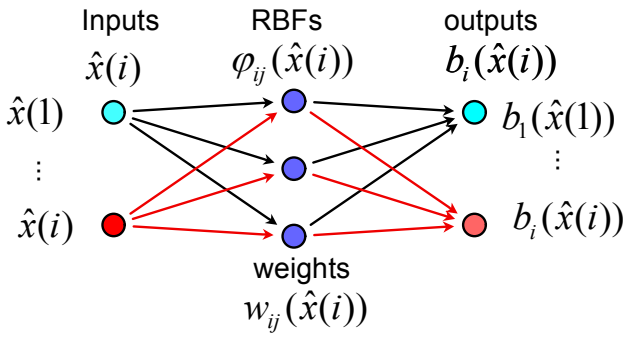

Fig. 5-12 Interpolation of measurement error with RBF Network.

The procedure to interpolate the three-dimensional measurement error of the sphere center with the RBF Network is shown as follows:

(1) Calibration of weight matrices

To build the RBF Network, its weight matrices, $w_{ij}(\hat{x}(i))$, must be identified. The calibration procedure of weight matrices is shown as follows:

(a) The same calibration cycle is performed as presented in Section 5.4. The sphere center is positioned at total $N = 27$ positions in a cube for calibration. The machine's positioning error is assumed to be sufficiently small compared to measurement uncertainty. The command sphere center positions are denoted by $x^*(i)$;

(b) The sphere center positions are "roughly" estimated by the algorithm proposed in Section 5.4.2, which are denoted by $\hat{x}(i)$ (i = 1,…,N). The radial basis functions are calculated with Eq. (5-7), and the weight matrix is best-fit with the least square method:

$$\min_{w_{ij}(\hat{x}(i))} \sum_{i=1}^{N} \left(b_i(\hat{x}(i)) - \varphi_{ij}(\hat{x}(i)) w_{ij}(\hat{x}(i)) \right)^2 \quad (j = 1, \ldots, N) \tag{5-8}$$

(2) Estimation of measurement error of sphere center position

When weight matrices, $w_{ij}(\hat{x}(i))$, are identified, the objective of the RBF

Network is to estimate the estimated measurement error of sphere center position $b_i(\hat{x}(i))$ (Eq.(5-5)) from roughly estimated sphere center position $\hat{x}(i)$. It is given by:

$$\hat{b}_i(\hat{x}(i)) = \sum_{j=1}^{N_x} \varphi_{ij}(\hat{x}(i)) w_{ij}(\hat{x}(i)) \quad (i = 1, \ \ldots, \ N) \tag{5-9}$$

Figure 5-13 shows the overall block diagram representation of the sphere center calculation algorithm for non-contact R-test, with compensating the measurement error of the laser displacement sensor.

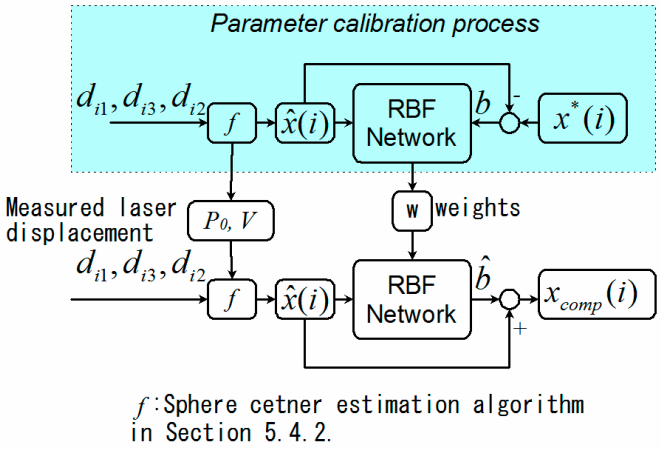

Fig. 5-13 Overall block diagram representation of the sphere center calculation algorithm for non-contact R-test.

5.6 Developed prototype of non-contact R-test device

A non-contact R-test prototype with three specular reflection type laser displacement sensors (LK-G10) was developed. This section presents the developed prototype, as well as experimental investigation of its measurement accuracy of sphere displacement.

5.6.1 Developed prototype of non-contact R-test with LK-G10

The developed R-test prototype is shown in Fig. 5-14. The specifications of the laser displacement sensor LK-G10 are shown in Table 5-1 of Section 5.3.2. The specifications of the ceramic sphere are shown in Table 5-4. Note that a

sphere with larger diameter (Φ 50 mm) compared to the one tested in Section 5.4.3 (Fig. 5-11) and Section 5.3.3 (Fig. 5-4) (see Table 2-2 of Section 2.2.2) is used to get a larger measurable area for each sensor, and consequently, larger measurable volume for sphere displacement.

The laser displacement sensors LK-G10 are installed on a sensors nest, whose orientation is tilted 45° from the horizontal plane, as shown in Fig. 5-14. With this set-up, the rotation range of the B-axis angle can reach ±90° in an R-test measurement cycle (see Section 3.3.1).

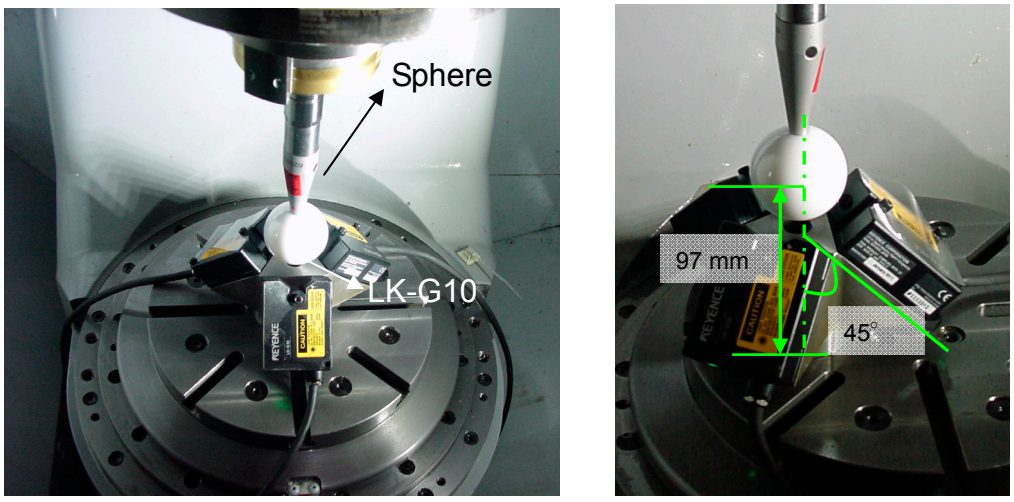

(a) External view (1) (b) External view (2)

Fig. 5-14 Non-contact R-test measurement device with three laser displacement sensors (LK-G10).

Table 5-4 Specifications of the reference ball (from Kolb & Baumann).

Diameter	50 mm +1.5μm at 20.6℃
Sphericity	below 0.4 μm
Material	ceramic

5.6.2 Profile measurement of a sphere with LK-G10

In Fig. 5-3 in Section 5.3.4, a profile measurement of a sphere of the diameter 25.5 mm was presented. Since a sphere of the diameter 50 mm is used for the non-contact R-test prototype, the same profile measurement is conducted for this sphere. This profile measurement is required to construct the RBF

Network presented in Section 5.5.1.

For the procedure for a profile measurement of a sphere, a reader should refer to Section 5.3.3. The measurement result is shown in Fig. 5-15. When the measurement range is extended to ±1 mm from the sphere top, the average error from the sphere's nominal geometry is about ±3 μm approximately. Compared with the test shown in Section 5.3.3, the measurement range is proportionally extended as the diameter of the sphere is enlarged. It is also observed that the measurement uncertainty is significantly dependent on the inclination of the target surface.

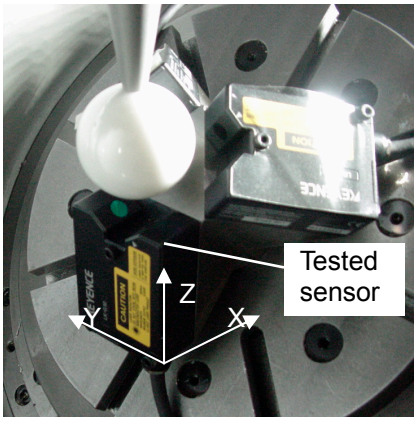

(a) Experimental setup

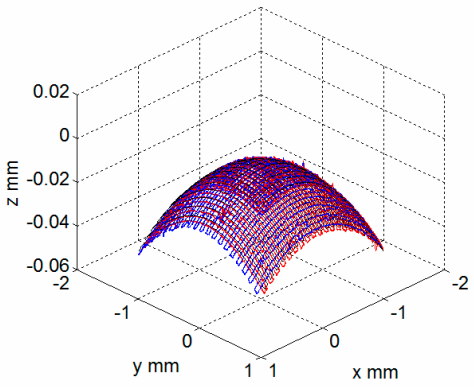

(b) Profile measurement result

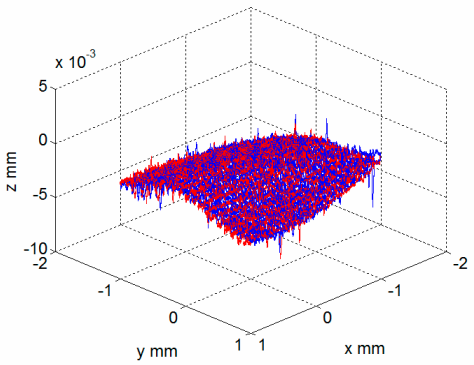

(c) Profile measurement error

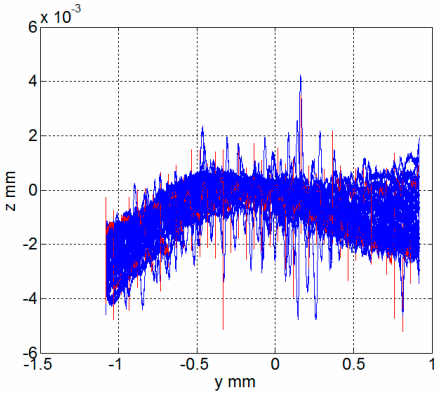

(d) Profile measurement error along Y-direction

Fig. 5-15 Profile measurement result of a sphere using LK-G10 and the sphere in Table 5-4.

5.6.3 Experimental verification of the proposed algorithm

The objective of this subsection is to experimentally investigate the validity of the algorithm to estimate the sphere center position from laser displacements, with the compensation of measurement errors due to the sphere curvature, presented in Section 5.5. The same test presented in Section 5.3.3 is conducted for the non-contact R-test prototype developed in the previous subsection.

The spindle-side sphere is positioned at total 27 positions within a cubic volume (1×1×1 mm) shown in Fig. 5-16(a) for parameter calibration. Then, the spindle-side sphere is positioned at total 1183 positions shown in Fig. 5-16(b) within the same volume to verify the measurement accuracy with the proposed algorithm shown in Fig. 5-13. After calibrating the parameters, the sphere center positions with compensation are estimated and shown in Fig. 5-16(b).

First, when the conventional algorithm for conventional contact-type R-test presented in Section 2.2.2 is used, errors in the estimated sphere center position from its command position (in X, Y, and Z directions) is shown in Fig. 5-16(c). Similarly as in Section 5.4.3, when the machine's positioning error is assumed to be sufficient small, these errors can be seen as the estimation error of the R-test measurement. Figure 5-16(d) shows the three-dimensional estimation error of sphere center positions by the algorithm proposed in Section 5.4.2 without compensating the measurement error of the laser displacement sensor itself; Figure 5-16(e) shows the three-dimensional estimation error of sphere center positions by the algorithm proposed in Section 5.5 (see Fig. 5-13) with compensating the measurement error of the laser displacement sensor.

It clearly shows that, 1) when the proposed algorithm in Section 5.4.2 is applied without the compensation, estimation errors are only slightly smaller than those with the conventional algorithm; there are still large estimation errors (within ±0.02 mm); 2) the estimation accuracy is significantly improved when the compensation presented in Section 5.5 is applied (the estimation error is summarized in Table 5-5).

In the tests above, both the calibration test (in Fig. 5-16(a)) and the

verification test (in Fig. 5-16(b)) were done with the same setup of the non-contact R-test. To further investigates its measurement accuracy under different setups, the measurement shown in Fig. 5-16(b) is also conducted when the rotary table is positioned at B = 0°, C = 0°; B = 90°, C = 0°; and B = 0°, C = 90°, to evaluate the repeatability and the effectiveness of the algorithm proposed in Section 5.5. The results are shown in Table 5-5. Note that the estimation error is evaluated by (mean, std). See Section 5.4.3 for the definition of (mean, std).

Table 5-5 indicates that the developed non-contact R-test device has the measurement uncertainty about 1.5 μm in the mean, and about 0.8 μm in the standard deviation within the measured volume 1×1×1 mm. It should be noted that the test results shown in Table 5-5 includes the positioning uncertainty of the machine tool as well.

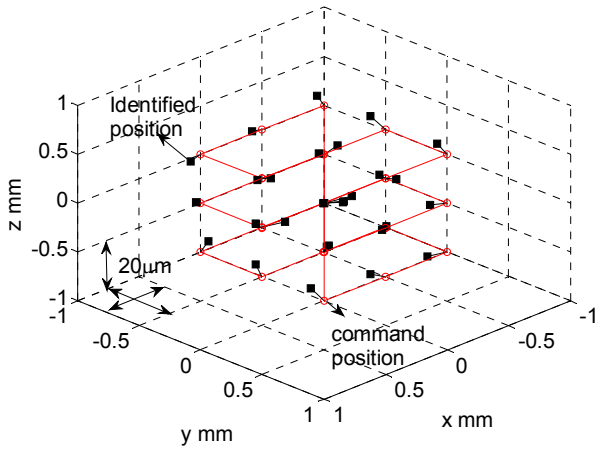

(a) Command and estimated sphere center positions for parameter calibration.

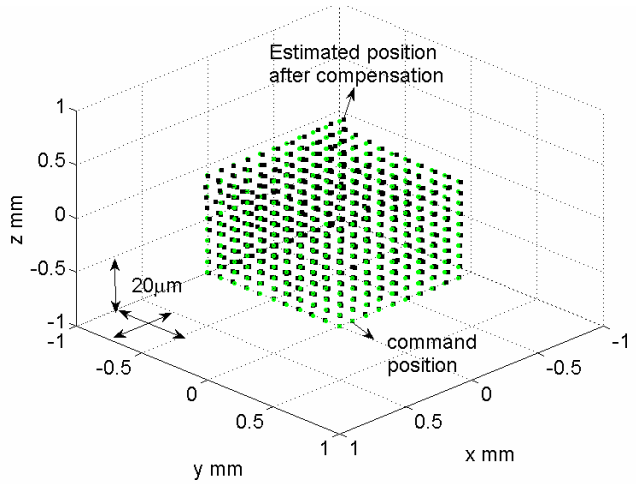

(b) Command and estimated positions with compensation

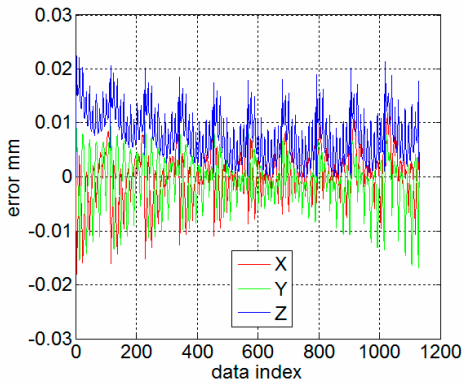

(c) Error with conventional algorithm for contact-type R-test (for total 1183 points shown in (b))

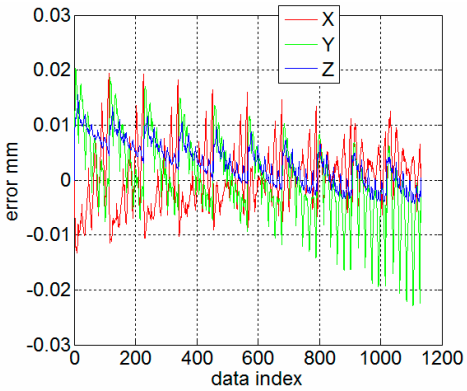

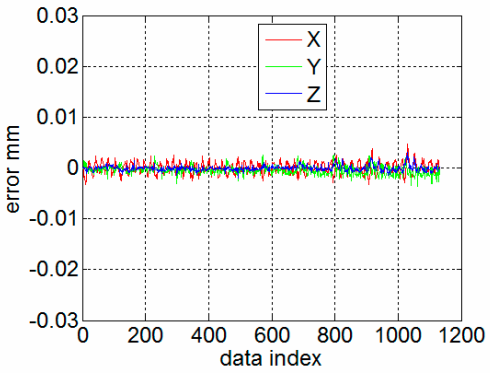

(d) Error without compensation (e) Error with compensation

Fig. 5-16 Estimation errors of sphere position within 1×1×1 mm.

Table 5-5 Measurement error (mean, std) and repeatability of sphere displacement with specular reflection type laser displacement sensor (LK-G10).

	Measurement volume (mm^3)	Sphere center estimation algorithm (μm)			Sphere center estimation with compensation (μm)		
		B=0°, C=0°	B=0°, C=90°	B=90°, C=0°	B=0°, C=0°	B=0°, C=90°	B=90°, C=0°
Measurement uncertainty	within 1^3	(6.5, 3.8)	(6.0, 3.7)	(6.3, 3.8)	(1.4, 0.7)	(1.6, 0.7)	(1.7,0.8)

5.7 Case studies

The objective of this subsection is to demonstrate the application of the developed non-contact R-test device to static and dynamic measurements, as well as to present the experimental comparison of measured results by contact-type

and non-contact R-test devices. Present experimental case studies includes: 1) a static measurement to calibrate an error map of a rotary axis, and 2) a dynamic measurement to observe dynamic errors in the synchronous motion between rotary axis and linear axes.

5.7.1 Calibration of an error map of a rotary axis in static measurement

(1) Test objective and procedure

The objective of this test is to experimentally investigate the measurement performance of the developed non-contact R-test in a static R-test measurement cycle presented in Section 3.3.1, as well as the experimental comparison with the contact-type R-test.

The static R-test measurement cycle presented in Section 3.3.1 is experimentally conducted on the same five-axis machine tool shown in Fig. 2-5 (in Section 2.3.1.2), with the contact-type R-test and with the non-contact R-test. The detailed experimental procedure can be found in Section 3.3.1. However, in this subsection, only the R-test measurement cycle of Setup 1-a (outer low), as shown in Fig. 3-1(a) of Section 3.3.1, was conducted. Sphere locations in the workpiece coordinate system are:

- Setup 1-a (outer low) with the contact-type R-test: ${}^{w}q_{ct}{}^{*}$ = [0.2, -83.9, 40.5] (mm)
- Setup 1-a (outer low) with the non-contact R-test: ${}^{w}q_{nc}{}^{*}$ = [0.7, -80.1, -3.0] (mm)

The R-test measurement cycle is conducted with the following command B and C angular positions:

B_i^* = -75°, -50°, …, 75° (i=1,…,7)

C_j^* = 0°, 30°, …, 330° (j=1,…,12)

The R-test measurement cycle was repeated for 3 times with the contact-type R-test and with the non-contact R-test, separately. The measurement result is plotted, as was proposed in Section 3.4. Note that static center offset of C-axis in X-, Y-, and Z-direction (i.e. δx^0_{BY}, δy^0_{CB}, δz^0_{BY}) is numerically eliminated, since it is usually not the inherent error of B-axis (see Section 3.4 for

more details).

The experimental setups (Setup 1-a(outer low) in Section 3.3.2) with the contact-type R-test and with the non-contact R-test are shown in Fig. 5-17 (a) and (b), respectively.

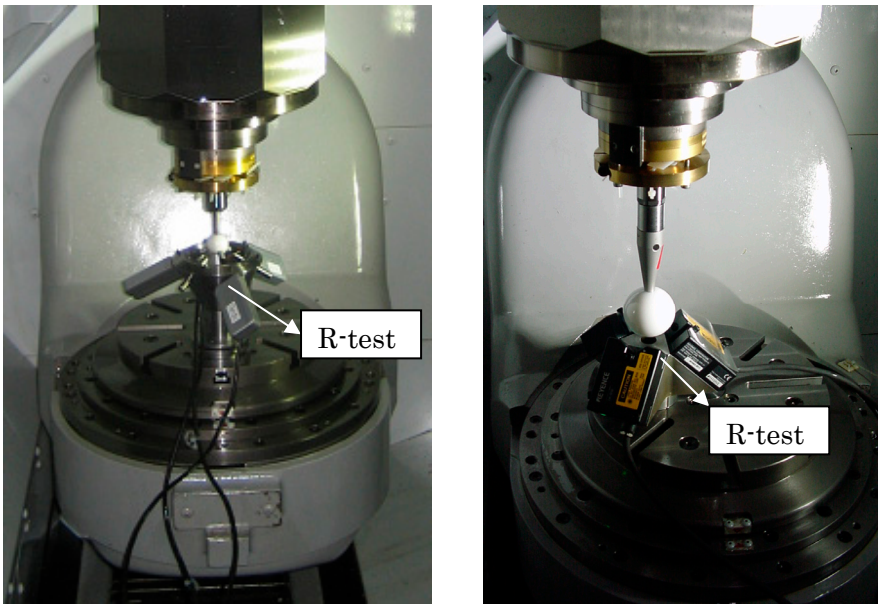

(a) with contact-type R-test (b) with non-contact R-test

Fig. 5-17 Experimental setups (Setup 1-a (outer low) in Section 3.3.2) with contact-type R-test and with non-contact R-test.

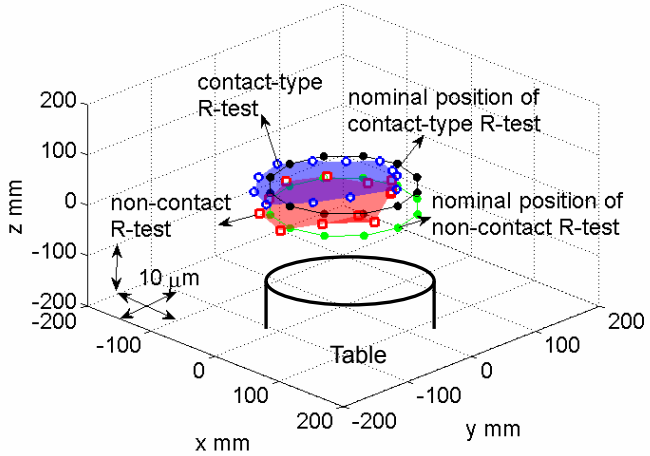

Fig. 5-18 Measured sensor positions in the static R-test measurement cycle by contact-type and non-contact R-test devices.

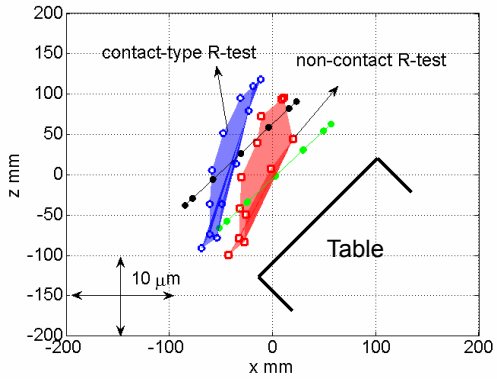

(a) At B = 50° projected on XZ plane

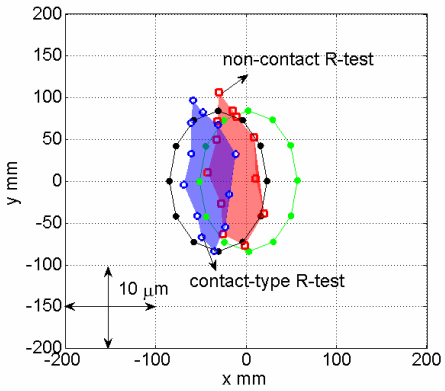

(b) At B = 50° projected on XY plane

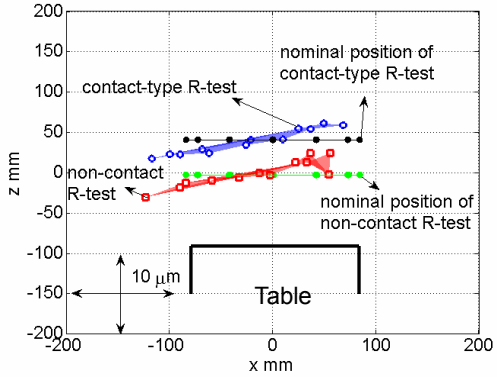

(c) At B = 0° projected on XZ plane

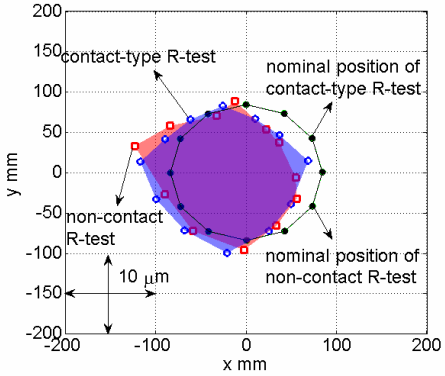

(d) At B = 0° projected on XY plane

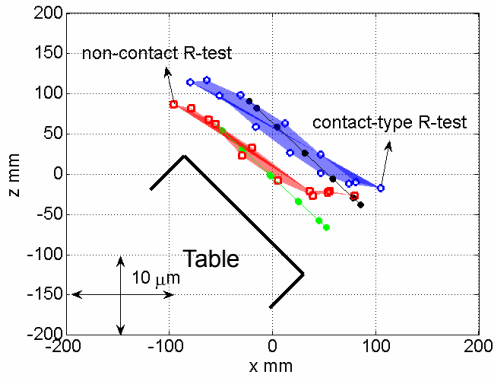

(e) At B = -50° projected on XZ plane

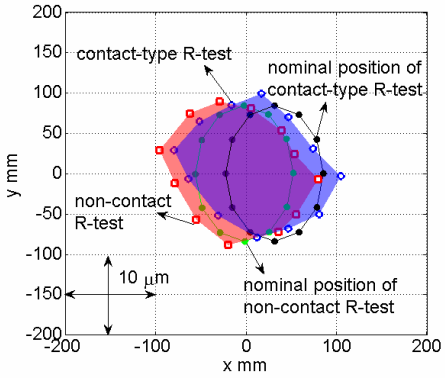

(f) At B = -50° projected on XY plane

Fig. 5-19 Measured sensor positions in the static R-test measurement cycle by contact-type and non-contact R-test devices, projected on XZ plane and XY plane.

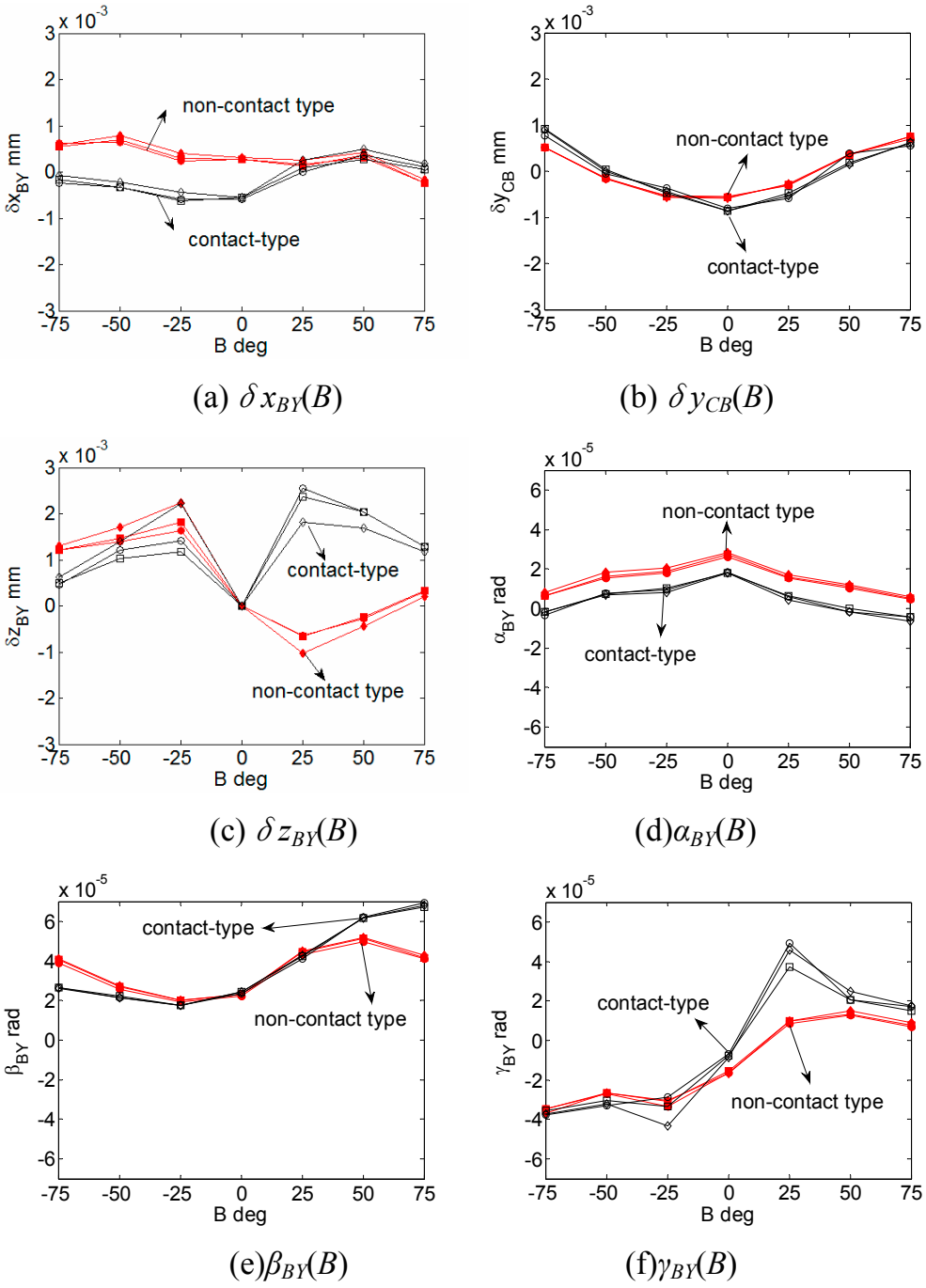

Fig. 5-20 Calibrated geometric errors of the rotary table.

(2) Test results

Figure 5-18 shows the graphical representation of the measured positions of the R-test sensors nest in the reference coordinate system when B = 0° (see Section 3.4 for more details on the representation scheme). The measured profiles at B = 50°, 0°, and -50° are projected onto (a) XZ plane and (b) XY

plane, as plotted in Fig. 5-19. The errors are magnified 10,000 times (i.e. with an error scale of 10 μm/100 mm). Note that the difference in the height (i.e. the distance from the table surface) of two profiles by contact-type and non-contact R-test devices in Figs. 5-18 to 5-19 is due to the difference in the Z-position of the sphere in both measurements.

Position-dependent geometric errors associated with the B-axis, or an error map of the rotary table, is calibrated with the method proposed in Section 3.6. The calibration result is shown in Fig. 5-20. See Table 2-4 for the description of each geometric error parameter. Note that all the three measurement cycles with the contact-type R-test and with the non-contact R-test are plotted in Fig. 5-20, to evaluate the repeatability of measurement.

(3) Observation

From the results shown in Figs. 5-18 to 5-20, the following observations could be made:

a. Measured position profiles shown in Fig. 5-19, as well as geometric error estimated in Fig. 5-20, by contact-type and non-contact R-test devices, show a good agreement within measurement uncertainties (and the machine's positioning uncertainties).
b. Both contact-type and non-contact R-test devices show good repeatability compared to the machine's positioning repeatability.
c. However, there are still some difference in measurement results, particularly in the $\delta z_{BY}(B)$ and $\beta_{BY}(B)$, as shown in Fig. 5-20(c) and (e). The deviation in the $\delta z_{BY}(B)$ is 3 μm approximately, , particularly at B = 25°. the angular deviation in the $\beta_{BY}(B)$ is about $\pm 2 \times 10^{-5}$ rad, particularly at B = ±75°. This may be caused by the thermal influence on the machine's error motions, although its exact cause is not fully investigated.

5.7.2 Dynamic measurement with synchronous motion of rotary axis and linear axes

(1) Test objective and procedure

As mentioned in Section 5.1, a dynamic measurement is defined as a measurement that is conducted when the machine tool is driven with a velocity. The objective of this test is to experimentally investigate the measurement performance of the developed non-contact R-test in a dynamic R-test measurement, as well as the experimental comparison with the contact-type R-test. The dynamic measurement was conducted with the synchronous motion of rotary axis (C-axis) and linear axes (X- and Y-axes).

The same machine tool presented in Section 2.2 was tested. The procedure is shown as follows:

a. The C-axis is commanded to rotate with a constant feedrate at B = 0°. The spindle-side sphere is commanded to follow the R-test sensors' nest on the table, as shown in Fig. 5-21.
b. The R-test continuously measures the relative displacement in the workpiece coordinate system. At the same time, X, Y, and C positions in the CNC system measured by the linear encoder are logged.
c. The dynamic measurement was conducted at two angular velocity of C-axis (358 degree/min and 3,583 degree/min in this case study), to observe the influence of the feedrate on dynamic errors.

Note that sphere locations in the workpiece coordinate system are:

- Setup 1-a (outer low) with the contact-type R-test: ${}^{w}q_{ct}^{*}$ = [0.2, -83.9, 40.5] (mm)
- Setup 1-a (outer low) with the non-contact R-test: ${}^{w}q_{nc}^{*}$ = [0.7, -80.1, -3.0] (mm)

which are the same as the static measurement in Section 5.7.1.

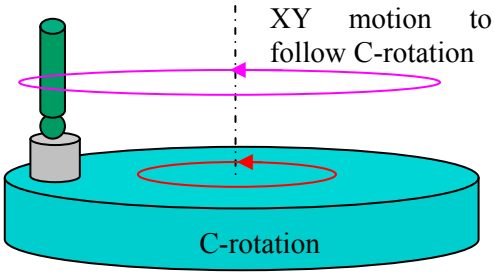

Fig. 5-21 Synchronous motion of C-axis and XY-axes.

(2) Test results

As mentioned in Section 2.2, R-test measures the displacement of sphere (i.e. the TCP) in the workpiece coordinate system, relative to the R-test sensors nest attached on the work table. As shown in Fig. 5-22, the measured R-test displacements are decomposed into the "radial", "tangential", and "axial" directions. Note that, in radial and tangential directions, the influence of the static center offset of B-axis in X- and Y-direction (i.e. δx^0_{CY}, δy^0_{CY}) is numerically eliminated (in the same manner as in Section 3.4).

Figure 5-23 shows measured displacement profiles in (a) radial, (b) tangential, and (c) axial directions, when the angular velocity of C-axis is 358 degree/min (i.e. the feedrate of the circular interpolation with linear axes is about 500 mm/min). Figure 5-24 shows the measured displacement profiles, when the angular velocity of C-axis is 3,583 degree/min (i.e. the feedrate of the circular interpolation with linear axes is about 5,000 mm/min).

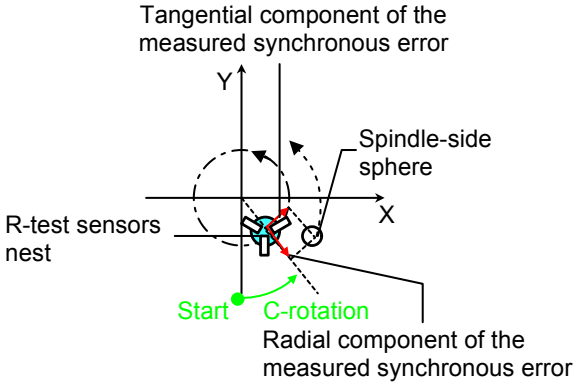

Fig. 5-22 Representation of the measured synchronous errors with synchronous motion of C-axis and X-, Y-axes.

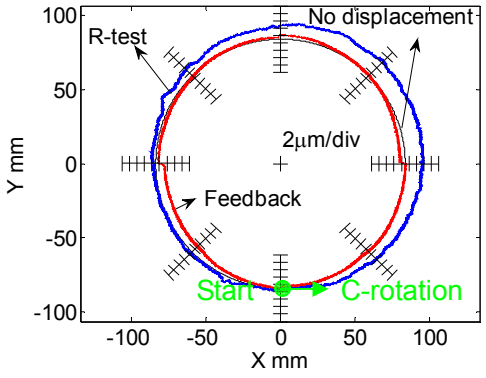

Contact-type R-test

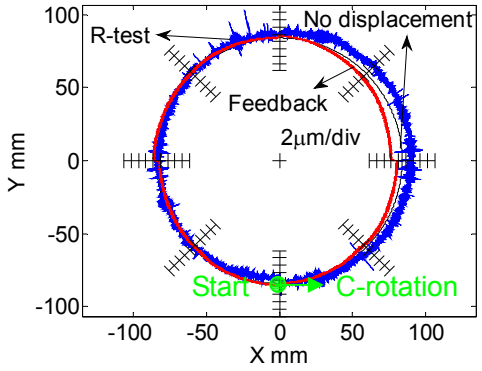

Non-contact R-test

(a) Radial direction

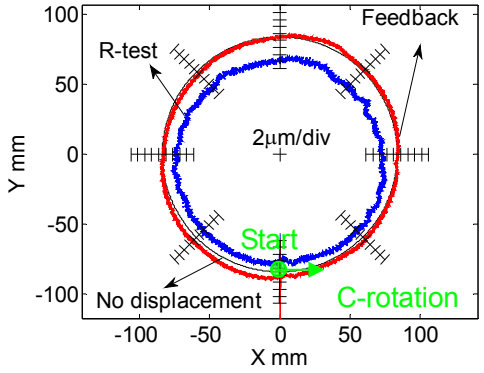

Contact-type R-test

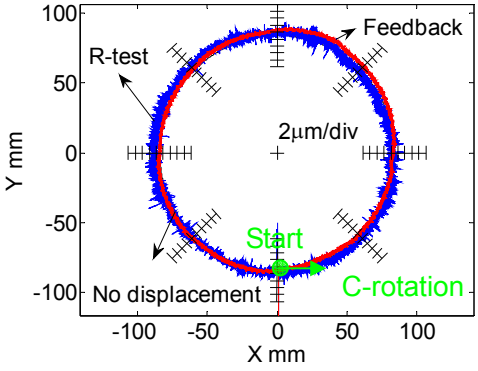

Non-contact R-test

(b) Tangential direction

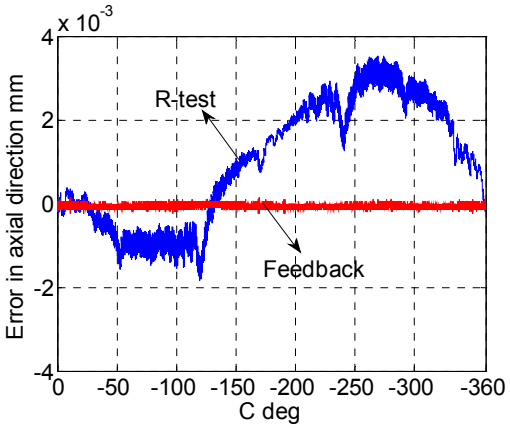

Contact-type R-test

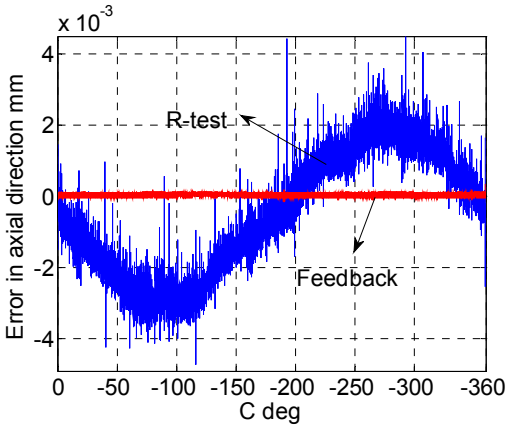

Non-contact R-test

(c) Axial direction

Fig. 5-23 Measured synchronous errors with synchronous motion of C-axis and X-, Y-axes (at C-axis angular velocity: 358 degree/min).

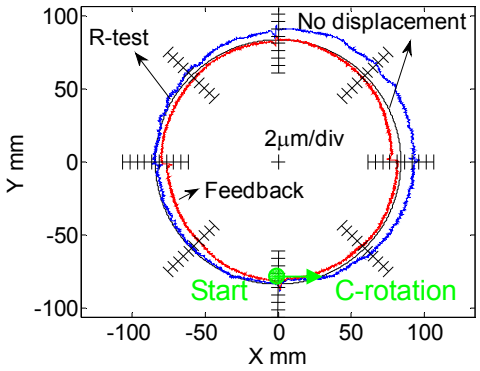

Contact-type R-test

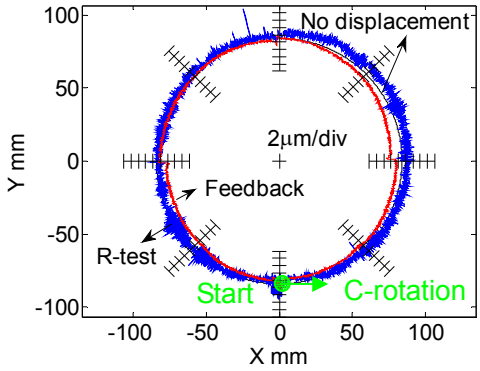

Non-contact R-test

(a) Radial direction

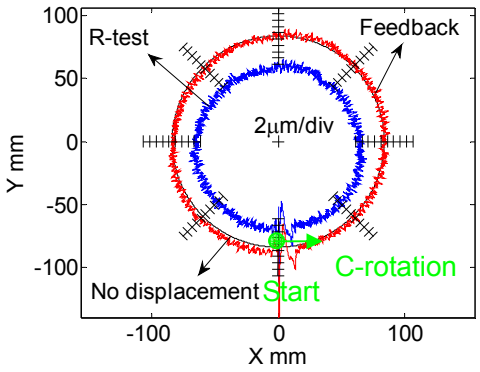

Contact-type R-test

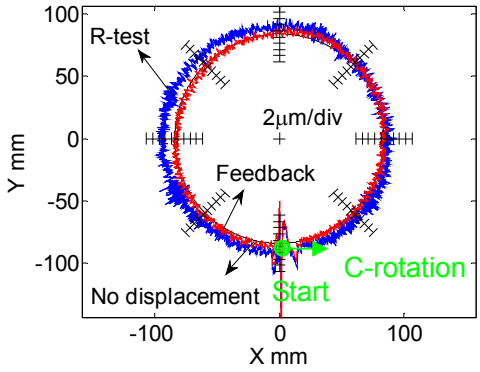

Non-contact R-test

(b) Tangential direction

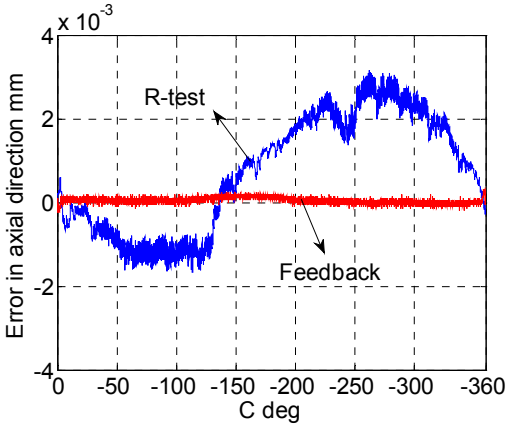

Contact-type R-test

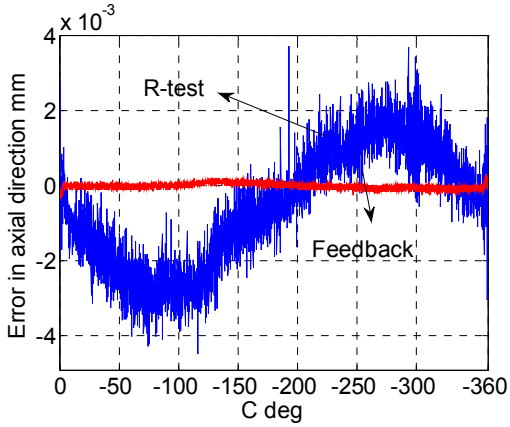

Non-contact R-test

(c) Axial direction

Fig. 5-24 Measured synchronous errors with synchronous motion of C-axis and X-, Y-axes (at C-axis angular velocity: 3,583 degree/min).

In Fig. 5-23(a) and Fig. 5-24(a), the radial component of the measured sphere displacement is magnified 2,500 times and polar-plotted. “R-test” represents the radial-direction trajectory measured by the contact-type (left) or the non-contact (right) R-test. “Feedback” represents the same trajectory calculated from X, Y, and C-positions measured by linear (rotary) encoders. The trajectory “Feedback” is identical in both left and right plots. The start position of the C-rotation and the rotation direction is pointed out in the figures. The circle with “no displacement” represents the level where there is no displacement. When the radius of the magnified error plot of R-test is larger than the reference circle representing zero error, it means the radius of the sphere center trajectory is larger than that of the R-test sensors nest trajectory on the table.

In Fig. 5-23(b) and Fig. 5-24(b), the tangential component of the measured displacement is magnified 2,500 times and polar-plotted. When the radius of the magnified error plot of R-test is smaller than the reference circle representing zero error, it means the spindle-side sphere center is delayed relative to the R-test sensors nest on the table.

The axial component of the measured displacement is plotted along the C-rotation angle, as shown in Fig. 5-23(c) and Fig. 5-24(c). The axial error in the positive direction means the sphere center moves to + Z direction relative to the R-test sensors nest.

(3) Observation

Many observations can be made from Figs. 5-23 and Fig. 5-24:

a. In the tangential direction (Fig. 5-23(b) and Fig. 5-24(b)), the measurement result with the contact-type R-test shows a constant delay in the spindle-side sphere position relative to the R-test sensors nest (about 3μm under 3,58 deg/min). Moreover, the delay enlarges as the angular velocity of C-axis increases (about 6μm under 3,583 deg/min). However, there is approximately no constant delay at both velocities of C-axis with the non-contact R-test. This may show the measurement error by the contact-type R-test device due to the

influence of the friction or the dynamics of sensors themselves. Its exact cause is, however, not clarified at this stage. To clarify it, “true” synchronous error of C-axis to XY-axes should be measured for comparison by a more reliable measuring instrument of the traceable measurement uncertainty. It is not done at this stage.

b. In the tangential direction (Fig. 5-23(b) and Fig. 5-24(b)), when the machine tool starts the synchronous motion, a spike-shaped error (about ± 5μm or ± 6×10^{-5} rad under 3,583 deg/min) could be observed both with the contact-type R-test and the non-contact R-test. This error can be also observed in the feedback data. This error is caused by transient synchronous errors of C- and X-axes.

c. In all plots (a) to (c) by the non-contact R-test, the “noise” (or high-frequency components of the measured profile) is larger (peak-to-peak 2 μm approximately). It could be caused by the measurement uncertainty of laser displacement sensor due to the speckle noise in laser beam. In profile scanning of a sphere shown in Fig. 5-15 in Section 5.6.2, similar noise can be observed.

d. Except for the “noise”, the radial trajectory (Fig. 5-23(a) and Fig. 5-24(a)) and the axial trajectory (Fig. 5-23(c) and Fig. 5-24 (c)) by contact-type and non-contact R-test devices show a good match.

5.8 Conclusion

(1) All the previous studies on the R-test in the literature used contact-type displacement sensors with a flat-ended probe. This chapter presented the development of the non-contact R-test device using laser displacement sensors. A non-contact R-test device was developed with the specular reflection type laser displacement sensor (LK-G10) in this study.

(2) The measurement accuracy of four laser displacement sensors with different measuring principles for profile measurement of a sphere surface was experimentally investigated. The performance of the four laser displacement sensors in the application to the non-contact R-test was

studied.

(3) A new algorithm was proposed to estimate the three-dimensional displacement of sphere center by using a non-contact type R-test with laser displacement sensors. It shows that the algorithm should consider the measurement uncertainty caused by the inclination of the target surface.

(4) The measuring performance of the developed non-contact R-test was investigated compared with the contact-type R-test in the application to error calibration of an error map of the rotary table in static measurement, as well as a dynamic measurement of synchronization errors of rotary axes and linear axes.

   a. Measurement results in the static measurement with contact-type and non-contact R-test devices show a good agreement. Both of contact-type and non-contact R-test devices exhibit good repeatability.

   b. Both R-test devices exhibited slightly different result in the dynamic measurement, particularly in the tangential direction to the C-axis rotation (about 3μm under C-axis velocity of 358 deg/min, about 6μm under 3,583 deg/min). Possibly, the dynamics of the contact-type R-test may be an error factor, while its exact cause should be clarified in the future.

   c. The prototype non-contact R-test device developed in this chapter is subjected to high-frequency noise of the amplitude about 2 μm due to the speckle noise in laser beam. When a laser displacement sensor of different measuring principle (e.g. the spectral interference type laser displacement sensor, studied in this chapter) is used, this noise may be significantly reduced, although the measurable area may become smaller.

Chapter 6
Influence of geometric errors of rotary axes on a machining test of cone frustum by five-axis machine tools

6.1 Introduction

The previous chapters (Chapter 3 to 5) focused on the error calibration method of geometric errors of rotary axes by R-test. One of inherent difficulties with five-axis machining is in that it is difficult to understand how error motions of machine tools are copied as the geometric error of the machined workpiece. For example, in case of three-axis machining with X, Y, and Z axes, the squareness error of linear axes is copied as the squareness error of two edges of the machined workpiece. On the other hand, in five-axis machining, it is difficult to intuitively understand how the squareness error of a rotary axis to a linear axis, one of location errors, is copied onto the machined workpiece. It is even more difficult to understand the influence of more complex error motions, parameterized as position-dependent geometric errors in this thesis.

As a result, it is difficult for machine tool builders or users to understand how important it is to calibrate such a complex error motion. If error motions of rotary axes calibrated in previous chapters (Chapter 3 and 5) do not impose significant influence on the machining accuracy, it is of no importance to calibrate them accurately.

For the same reason, it is difficult to diagnose the cause in machine tools for the geometric inaccuracy of the machined workpiece. As a typical example, a machining test of cone frustum, described in NAS (National Aerospace Standard) 979 [NAS 979, 1969], is widely accepted by machine tool builders to evaluate the machining performance of five-axis machine tools. In this test, even when the geometric error of the machined test piece exceeds the acceptable tolerance, it is generally very difficult for machine tool builders to find its causes, and then to

find where to improve in the machine configuration to achieve the target accuracy.

This chapter discusses the influence of various error motions of rotary axes on a five-axis machine tool on the machining geometric accuracy of cone frustum machined by this test. From such an analysis, we can evaluate the importance of each error motion with respect to the influence on the machining accuracy in the given machining application. Furthermore, such an analysis can be the fundamental for error diagnosis from the geometric inaccuracy of the machined workpiece.

It must be emphasized that the cone frustum machining test is just an example of machining applications. This chapter considers the cone frustum machining test only, as an example of widely accepted machining tests in the machine tool industry. Analogous error sensitivity analysis methodology to be presented in this chapter can be straightforwardly applied to any machining applications in general.

6.2 Objective and original contribution of this chapter

NAS 979 [NAS 979, 1969] describes the evaluation of machining accuracy of a five-axis machine tool by the machining of a cone frustum, which is widely accepted to many machine tool builders as a final performance test for five-axis machine tools. Equivalent non-cutting measurement methods using a ball bar measurement have also been studied by Ihara et al. [Ihara, 2005, Matano, 2007], and its inclusion in the revised ISO 10791-6 [ISO 10791-6, 2011] is currently under discussion in ISO/TC39/SC2.

A critical issue with this cone frustum test is that the influence of the machine's error sources on the geometric accuracy of the machined workpiece is very difficult to understand for machine tool builders.

The influence of the machine's position-independent geometric errors (location errors) on the geometric error of the machined cone frustum test piece was discussed in [Uddin, 2009]. Matsushita et al. [Matsushita, 2008] and Yumiza et al. [Yumiza, 2007] presented similar analysis to discuss how their influences

are correlated to the location and the orientation of test piece. As is clear from these error analyses, a part of position-independent geometric errors imposes a significant influence on the circularity of the machined test piece.

From our experiences, however, on the latest commercial small-sized five-axis machine tools, the circularity error can be typically as small as five to ten micrometers. It suggests that position-independent geometric errors on such a machine are tuned sufficiently small. To further improve the circularity of the machined test piece on such a machine, more complex error motions of a rotary axis, such as the gravity deformation, angular positioning error of a rotary axis, pure radial error motions or tilt error motions of a rotary axis, must be reduced. Such more complex error motions can be modeled as position-dependent geometric error, as presented in Section 2.2. To our knowledge, no work in the literature extended the analysis to position-dependent geometric error.

The objective of this paper is to present a numerical analysis of the influence of major error motions on the circularity error of the machined cone frustum test piece. Error motions that have relatively larger influence on circularity, and those that have negligibly small influence, are found out. Based on the present discussion, experimental case studies are presented to demonstrate the error diagnosis on a cone frustum machining test.

It must be emphasized that the main contribution of this chapter is on the proposal of the analysis methodology of the sensitivity of position-dependent geometric errors on the machining geometric accuracy. It can be applied basically to any machining applications.

6.3 Setup of cone frustum machining test

Figure 6-1 shows machining configuration and parameters of tilted cone frustum to be considered in this paper. D, φ, ψ are defined as diameter of tool path, tilted angle of cone frustum about Y-axis in the workpiece coordinate system and half-apex angle of the cone frustum, respectively. (C_x, C_y, C_z) is the center location of tool tip trajectory in the workpiece coordinate system. The origin of the workpiece coordinate system is defined at the intersection of

nominal B-axis and C-axis. For simplicity of computation, this section simulates a tool center trajectory which can be interpreted as a geometric profile of the machined workpiece surface when the tool radius is zero.

Table 6-1 shows the conditions for cone frustum machining test used in simulations presented in Sections 6.4 and 6.5. The simulation will be conducted under two conditions: (a) φ=15°, ψ=30° and (b) φ=75°, ψ=30°. The machine configuration shown in Fig. 2-5 is assumed. The command trajectory of each axis in each case is shown in Fig. 6-2. The algorithm to calculate the command trajectory $X^*(k)$, $Y^*(k)$, $Z^*(k)$, $B^*(k)$, and $C^*(k)$ (k = 1,…,N) can be found in e.g. [Uddin, 2009].

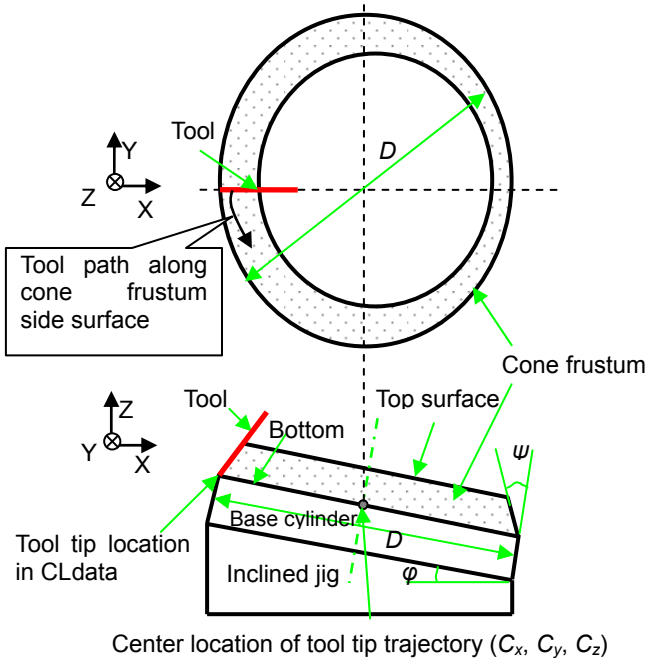

Fig. 6-1 Setup for machining test of cone frustum.

Table 6-1 Test conditions for the machining test of cone frustum

Parameter	Value	
Diameter of tool path, D (mm)	129.9	
Tilt angle, φ(°)	case (a): 15	case (b): 75
Half-apex angle, ψ (°)	30	
Center location of tool path (C_x, C_y, C_z) (mm)	(-81.8, 0,189.3)	

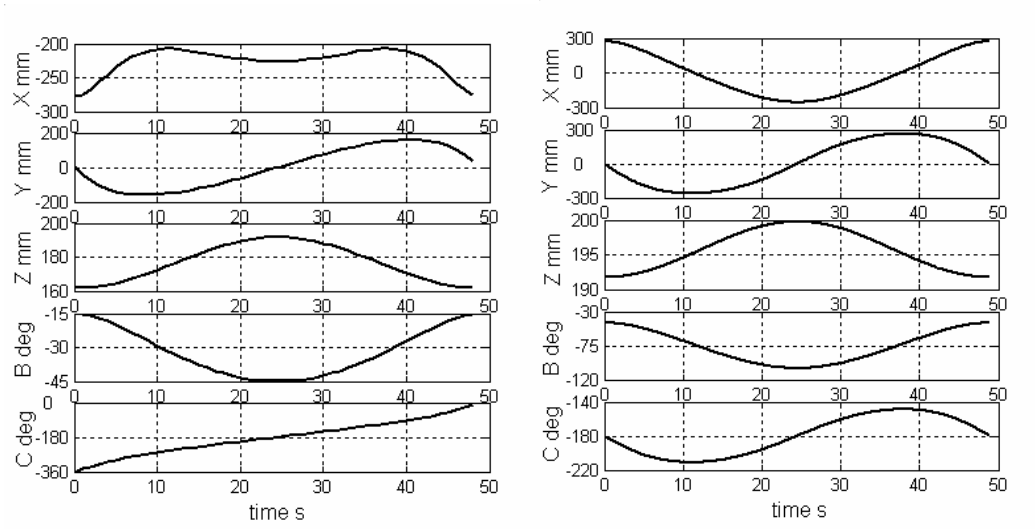

(a) $\varphi<\psi$ (φ=15°, ψ=30°) (b) $\varphi>\psi$ (φ=75°, ψ=30°)

Fig. 6-2 Command trajectory of each axis (assuming feedrate 1,000 mm/min).

It is to be noted that Ihara and Tanaka [Ihara, 2005] showed that command trajectories for cone frustum machining can be categorized into two groups. When $\varphi<\psi$, C-axis rotates for 360°, while B-axis rotates for 2φ, as is shown in Fig. 6-2 (a). However when $\varphi>\psi$, B-axis rotates for 2ψ, while C-axis does not rotate for 360°, as is shown in Fig. 6-2 (b).

Although the following section shows only two simulation results for representative cases $\varphi<\psi$ (φ=15°, ψ=30°) and $\varphi>\psi$ (φ=75°, ψ=30°), the discussion in [Ihara, 2005] indicates that the influence of each error motion on the contouring accuracy can be also qualitatively categorized into either case ($\varphi<\psi$ or $\varphi>\psi$).

6.4 Influence of position-independent geometric errors of rotary axes

(1) Analysis objective and procedure

This subsection first discusses the quantitative influence of position-independent geometric errors, or location errors shown in Table 2-3 in Section 2.3.1.2, on the circularity of the machined cone frustum test piece. Although such a sensitivity analysis of position-independent geometric errors can be found in previous studies in the literature [Uddin, 2009, Matsushita, 2008,

Yumiza, 2007], this subsection briefly reviews it, since it is the fundamental for the analysis to be presented in Section 6.5.

Note that for the definitions and symbols of geometric errors, including position-independent geometric errors (in Table 2-3), and position-dependent geometric errors (in Table 2-4), a reader should refer to Section 2.3.1.2.

When each position-independent geometric error of rotary axes in Table 2-3 is set either 0.01mm for linear errors or 0.01° for angular errors, the tool position in the workpiece coordinate system, ${}^{w}q \in \Re^3$, is calculated by using the kinematic model (with Eq. (2-11) in Section 2.3.2), for the given command position ($X^*(k)$, $Y^*(k)$, $Z^*(k)$, $B^*(k)$, and $C^*(k)$). By repeating this simulation at each position in command trajectories in Fig. 6-2, a contour error trajectory in the workpiece coordinate system is computed.

(2) Analysis result

A simulated error trajectory for each position-independent geometric error is shown in Fig. 6-3. The *circularity error*, or the circular deviation *G* (defined in ISO 230-4 [ISO 230-4, 2005]), defined as *the difference between maximum and minimum radial errors*, is computed from the simulated error trajectory. Note that the center of simulated error trajectory is set to the MRS center (minimum radial separation center) [ISO 230-4, 2005], where the smallest circularity error is obtained. The simulated sensitivity of circularity error to each position-independent geometric error is summarized in Table 6-2.

From the simulation results shown in Fig. 6-3, it can be observed that: 1) the influence of δx^0_{BY}, δx^0_{CB}, and β^0_{BY} on the geometry of the contour error trajectory is qualitatively similar, either of which affect the contour error trajectory in X-direction (or in Y-direction). Note that the amplitude of distortion depends on the value of the assumed error; 2) the influence of δy^0_{BY}, α^0_{CB}, and α^0_{BY} is qualitatively similar, either of which affects the contour error trajectory to 45° direction to the X-axis; 3) both δz^0_{BY} and γ^0_{BY} do not affect the contour error trajectory of cone frustum at all. Therefore, it is generally not possible to conduct

error diagnosis of each position-independent geometric error of rotary axes by a single cone frustum machining test.

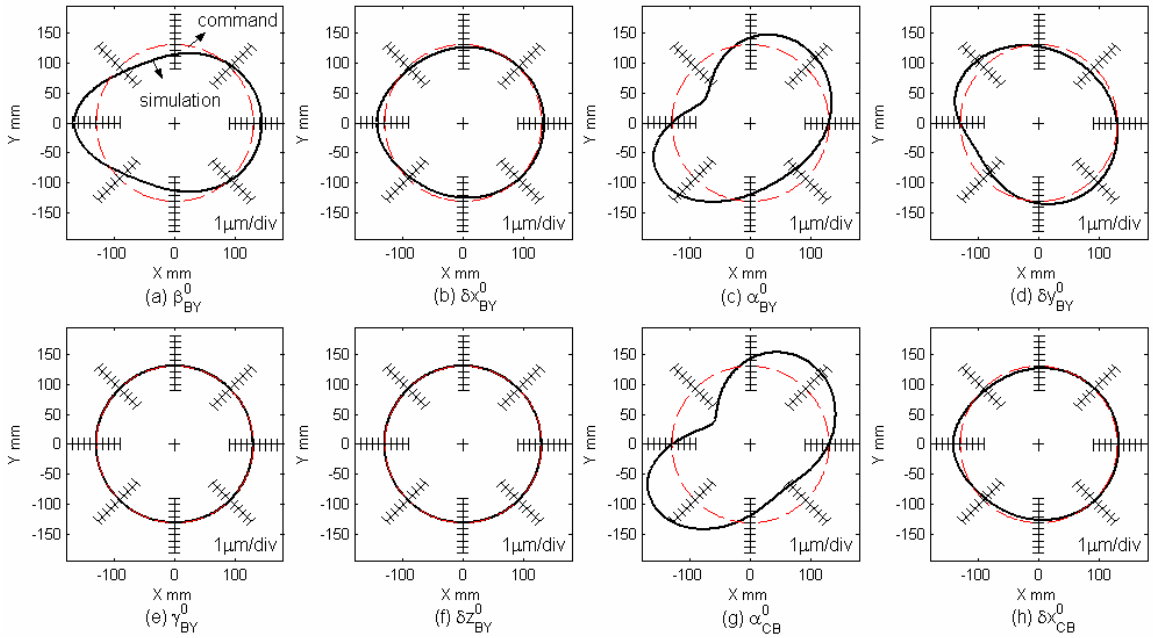

(a) $\varphi<\psi$ (φ=15°, ψ=30°)

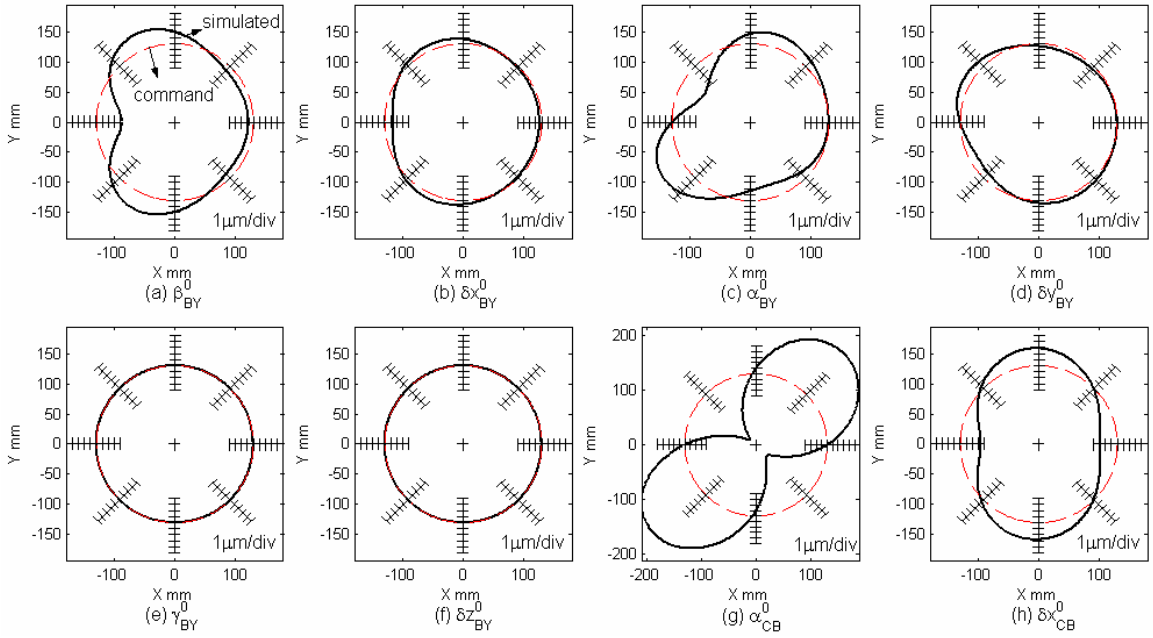

(b) $\varphi>\psi$ (φ=75°, ψ=30°)

Fig. 6-3 Influence of each position-independent geometric error on simulated contour error profile.

Table 6-2 Circularity error simulated with each position-independent geometric error

Contributor	Circularity error (μm)	
	$\varphi<\psi$ (φ=15°, ψ=30°)	$\varphi>\psi$ (φ=75°, ψ=30°)
α^0_{BY}	9.1	8.2
β^0_{BY}	5.6	7.2
γ^0_{BY}	0	0
α^0_{CB}	11.8	22.4
δx^0_{BY}	1.9	2.3
δy^0_{BY}	3.6	2.6
δz^0_{BY}	0	0
δx^0_{CB}	1.7	6.3

6.5 Influence of position-dependent geometric errors of rotary axes

6.5.1 Analysis objective and basic methodology

This subsection further extends the analysis to more complex error motions of a rotary axis, described by position-dependent geometric errors. The objective of this subsection is to present the sensitivity of the circularity of cone frustum workpiece to each error motion under two conditions (in Table 6-1).

The basic analysis methodology is as follows: as an illustrating example, consider the problem to investigate the influence of B-axis angular positioning error on the circularity of the machined cone frustum workpiece (see Section 6.5.2). A profile of B-axis angular positioning error, as a function of the B angular position (B_i), can be arbitrary. It is not possible to study the influence of an infinite number of B-axis angular positioning error profiles. Instead, we assume a "typical" function for this trajectory. For example, the B-axis angular positioning error is typically a linear function of the B-angular position, caused by e.g. homogenous expansion of a linear encoder. The gradient of this function may differ at different region, due to e.g. a calibration error of a linear encoder. By considering "typical" error profiles found in actual machine tools, we model a profile of B-axis angular positioning error as the superposition of multiple first-order functions of B-angular position. Their gradient, amplitude and offset are parameters to be specified.

Then, the influence of this B-axis angular positioning error profile on the circularity of the cone frustum workpiece is simulated by using the kinematic model (with Eq. (2-11) in Section 2.3.2), for the given command position ($X^*(k)$, $Y^*(k)$, $Z^*(k)$, $B^*(k)$, and $C^*(k)$).

The influence of the B-angular positioning error on the circularity of the cone frustum workpiece is studied by using the Monte Carlo simulation. In other words, parameters of the geometric error (the gradient, the amplitude, and the offset of the profile in this example) are randomly given with specified mean and standard deviation, and the workpiece circularity is simulated in each case. The sensitivity of input geometric errors to statistical mean and standard deviation of simulated circularity is studied. Such a statistical analysis based on the Monte Carlo simulation is common and well established in the measurement uncertainty analysis to evaluate the influence of each uncertainty contributor on the overall measurement uncertainty [JCGM 100, 2008]. For example, in [Bringmann, 2009], the influence of error motions of linear axes on the estimation of location errors was studied by using the Monte Carlo simulation. Similarly as in this subsection, error motions of linear axes are modeled by typical functions. It can be seen analogous to the analysis procedure presented in this chapter.

This subsection considers the following error motions of rotary axes, which are potentially common errors observed in commercial five-axis machine tools.

6.5.2 Angular positioning error of B-axis

As was discussed in the previous subsection, we assume that the B-axis has an angular positioning error profile shown in Fig. 6-4(a) with arbitrary a_1, a_2 and b. Note that a_0=mean ($\beta_{BY}(B_i)$) and a_1 represents the gradient of the least square fit line for $\beta_{BY}(B)$. Such an error profile can be decomposed into three components as is shown in Fig. 6-4(b)-(d) (i.e. $\beta_{BY}(B_i) = \beta^0{}_{BY} + \beta^1{}_{BY}(B_i) + \beta^2{}_{BY}(B_i)$). Each position-dependent component is formulated as follows:

$$\beta_{BY}{}^{1}(B_i) = \frac{a_1}{2} + \frac{B_i - B_{\max}}{B_{\max} - B_{\min}} a_1 \tag{6-1}$$

$$\beta_{BY}{}^{2}(B_i)=\begin{cases}\dfrac{a_2}{2}+\dfrac{B_i-b}{b-B_{\min}}a_2 & B_i\in(B_{\min},b)\\ -\left(\dfrac{a_2}{2}+\dfrac{B_i-B_{\max}}{B_{\max}-b}a_2\right) & B_i\in(b,B_{\max})\end{cases} \tag{6-2}$$

where a_1 and a_2 are given by N (0.01°, 0.0033°)**sgn*, where N (μ, σ) represents a normally distributed random number with the mean value μ and the standard deviation (abbreviated by std) σ. *sgn* is either +1 or -1 with 50% possibility. B_{min} and B_{max} are respectively set to be minimum or maximum of rotation angle of the B-axis. For example, for case (a) (φ=15°, ψ=30°), B_{min} and B_{max} are set to be -45° and -15°, respectively, because the command B-angle is between -45° and -15° as shown in Fig 6-2(a). b is the rotation angle where the gradient of modeled error profile ($\beta^2_{BY}(B)$) changes, which is given by b=U (B_{min}, B_{max}), where U (m, n) represents a uniformly distributed random number on the interval (m, n). $\beta^1_{BY}(B)$ refers to first-order component of the considered angular positioning error profile of B-axis, as shown in Fig. 6-4(c). $\beta^2_{BY}(B)$ refers to the ramp-type component as shown in Fig. 6-4(d).

The mean and the distribution of input random parameters (e.g. μ and σ for a_1 and a_2) should be selected according to typical level of positioning accuracy in commercial machine tools. Although it is in practice difficult for us to select "typical" level of motion errors, it should be noted that the major contribution of the present analysis is to find out the sensitivity, or the ratio, of input motion errors to the output circularity, not absolute value of the circularity.

It must be emphasized that investigating the influence of a periodic error of higher frequency (e.g. a periodic error caused by worm gear or a bearing) is not in main scope of this section, since the influence of such an error can be understood relatively easily. This section studies the influence of lower-frequency error profiles as represented in Fig. 6-4 as a potentially critical error factor in typical five-axis machines.

The influence of position-independent component, namely β^0_{BY}, was studied in Section 6.3 and summarized in Table 6-2. For $\beta^1_{BY}(B)$, total 1,000 simulations to compute geometric error profile of the machined cone frustum workpiece are performed with randomly given a_1. Similarly, the influence of

$\beta^2_{BY}(B)$ is studied with 1,000 simulations. The mean value and standard deviation (1σ) of simulated circularity errors is calculated.

Table 6-3 shows the sensitivity of the circularity of cone frustum workpiece to angular positioning errors of B-axis. For $\varphi<\psi$ (φ=15°, ψ=30°), it can be observed that the influence of $\beta^1_{BY}(B)$ is relatively small, since such a monotonously increasing (decreasing) positioning error mostly changes the radius and the center position of error trajectory, and thus has small influence on the circularity. On the other hand, the circularity is significantly more sensitive to $\beta^2_{BY}(B)$.

6.5.3 Axial error motion of B-axis

An axial position error of B-axis, typically caused by geometric profile error of a bearing, is analogously modeled by $\delta y^1_{BY}(B)$ and $\delta y^2_{BY}(B)$ as in Eq. (6-1) and Eq. (6-2) , while a_1 and a_2 are given by N (10 μm, 3.3 μm)**sgn*. The results are also shown in Table 6-3.

Table 6-3 Influence of angular positioning error of B-axis, axial error motion of B-axis and linear error motion of B-axis to Z- direction

Contributor		Parameter setting (a_1 and a_2)	Circularity error (μm)			
			φ=15°, ψ=30°		φ=75°, ψ=30°	
			mean	std	mean	std
Angular positioning error of B-axis	$\beta^1_{BY}(B)$	N (0.01°, 0.0033°)**sgn*	3.6	1.3	20	6.7
	$\beta^2_{BY}(B)$		32	11.5	15	11.1
Axial error motion of B-axis	$\delta y^1_{BY}(B)$	N (10 μm, 3.3 μm)**sgn*	3.5	1.2	6.0	2.2
	$\delta y^2_{BY}(B)$		4	1.5	7.5	3.3
Linear error motion of B-axis to Z- direction	$\delta z^1_{BY}(B)$	N (10 μm, 3.3 μm)**sgn*	0	0	0	0
	$\delta z^2_{BY}(B)$		0	0	0	0

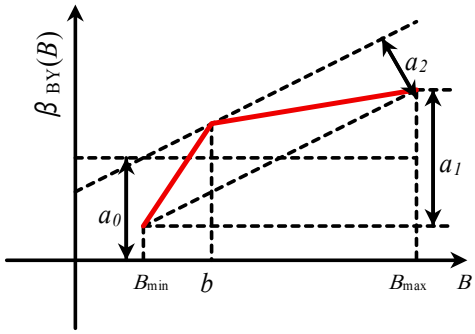

(a) Total angular positioning error profile of B-axis ($\beta_{BY}(B)$)

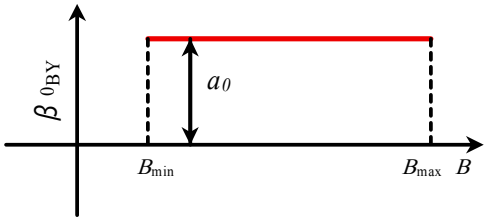

(b) Position-independent component ($\beta^0{}_{BY}(B)$)

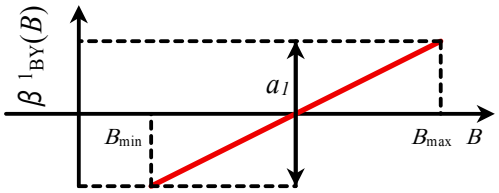

(c) First-order component ($\beta^1{}_{BY}(B)$)

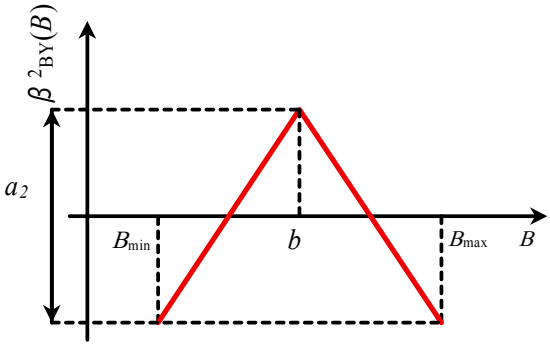

(d) Ramp-type component ($\beta^2{}_{BY}(B)$)

Fig. 6-4 Angular positioning error profile of B-axis considered in sensitivity study.

6.5.4 Linear error motion of B-axis to Z-direction

A linear error motion of B-axis to Z-direction, typically caused by the gravity-induced deformation of a rotary unit, is modeled as $\delta z^1_{BY}(B)$ and $\delta z^2_{BY}(B)$ in the same way with $\delta y_{BY}(B)$ in Section 6.5.3. Since linear error motion of B-axis to Z-direction ($\delta z_{BY}(B)$) is at the non-sensitive direction, the influence of $\delta z_{BY}(B)$ is negligibly small for both setups, as the simulation results shown in Table 6-3.

6.5.5 Angular positioning error of C- axis

The angular positioning error of C-axis $\gamma_{CB}(C)$ is assumed to be periodic for 360° rotation of C-axis. Therefore, an angular positioning error proportional to C angular position, with a different gradient before and after the given c, is considered. Analogous to error shown in Fig. 6-4 (d), it is modeled as follows:

$$\gamma^2_{CB}(C_i)=\begin{cases}\dfrac{a_2}{2}+\dfrac{C_i-c}{c-C_{\min}}a_2 & C_i\in(C_{\min},c)\\ -\left(\dfrac{a_2}{2}+\dfrac{C_i-C_{\max}}{C_{\max}-c}a_2\right) & C_i\in(c,C_{\max})\end{cases} \tag{6-3}$$

where c is given by c=U (C_{min}, C_{max}), a_2 is given by a_2 =N (0.01°, 0.0033°)*sgn. C_{min} and C_{max} are respectively set to be minimum or maximum of rotation angle C_i. Similar simulation process is conducted as in Section 6.5.2, and results are shown in Table 6-4.

Table 6-4 Influence of angular positioning error, axial error motion of C-axis

Contributor		Parameter setting (a_2)	Circularity error (μm)			
			φ=15°, ψ=30°		φ=75°, ψ=30°	
			mean	std	mean	std
Angular positioning error of C-axis	$\gamma^2_{CB}(C)$	N (0.01°, 0.0033°)*sgn	4.6	2.0	16.5	11.4
Axial error motion of C-axis	$\delta z^2_{CB}(C)$	N (10 μm, 3.3 μm)*sgn	2.0	0.9	6.6	2.5

6.5.6 Axial error motion of C-axis

An axial error motion of C-axis, typically caused by geometric profile error of bearing, is modeled by $\delta z^2_{CB}(C)$ as in Eq. (6-3), while a_2 is given by $a_2 = N$ (10 μm, 3.3 μm)**sgn*. The simulation results are shown in Table 6-4.

6.5.7 Periodic pure radial error motion of B- and C-axis

Figure 2-7(b) in Section 2.3.1.2-(4) shows periodic pure radial error motion of C-axis, or "run-out" of C-axis, which is modeled as follows:

$$\begin{cases} \delta x_{CB}(C_i) = a_2 \cos(C_i + \zeta) \\ \delta y_{CB}(C_i) = a_2 \sin(C_i + \zeta) \end{cases} \tag{6-4}$$

Periodic pure radial error motion of B-axis is modeled as follows:

$$\begin{cases} \delta x_{BY}(B_i) = a_2 \cos(B_i + \zeta) \\ \delta z_{BY}(B_i) = a_2 \sin(B_i + \zeta) \end{cases} \tag{6-5}$$

where a_2 and ζ are given by:

$a_2 = N$(10 μm, 3.3 μm), $\zeta = U$(0°, 360°).

The simulation results are shown in Table 6-5. From the simulation results, the influence of pure radial error motion of B- and C-axis on circularity is sufficiently small compared to given errors.

Table 6-5 Influence of periodic pure radial error motion and conical tilt error motion of B- and C-axis

Contributor		Parameter setting (a_2)	Circularity error (μm)			
			φ=15°, ψ=30°		φ=75°, ψ=30°	
			mean	std	mean	std
Periodic pure radial error motion of C-axis	$\delta x_{CB}(C)$ and $\delta y_{CB}(C)$	N (10 μm, 3.3 μm)	0	0	0	0
Periodic pure radial error motion of B-axis	$\delta x_{BY}(B)$ and $\delta z_{BY}(B)$		0.8	0.6	3	2.5
Periodic conical tilt error motion of C-axis	$\alpha_{CB}(C)$ and $\beta_{CB}(C)$	N (0.01°, 0.0033°)	0	0	0	0
Periodic conical tilt error motion of B-axis	$\alpha_{BY}(B)$ and $\gamma_{BY}(B)$		4.6	3.5	12	9.0

6.5.8 Periodic conical tilt error motion of B- and C-axis

As is shown in Fig. 2-7(c) in Section 2.3.1.2-(4), periodic conical tilt error motion of C-axis is modeled as follows:

$$\begin{cases} \alpha_{CB}(C_i) = a_2 \cos(C_i + \zeta) \\ \beta_{CB}(C_i) = a_2 \sin(C_i + \zeta) \end{cases} \tag{6-6}$$

Similarily, periodic conical tilt error motion of B-axis is modeled as follows:

$$\begin{cases} \alpha_{BY}(B_i) = a_2 \cos(B_i + \zeta) \\ \beta_{BY}(B_i) = a_2 \sin(B_i + \zeta) \end{cases} \tag{6-7}$$

where a_2 and ζ are given by:

a_2=N(0.01°, 0.0033°), ζ= U(0°, 360°).

The simulation results are shown in Table 6-5. The influence of periodic conical tilt error motion of C-axis on circularity is sufficiently small compared to given errors. However, periodic conical tilt error motion of B-axis have significantly larger influence, especially when φ>ψ (φ=75°, ψ=30°).

6.5.9 Change in position and orientation of C-axis centerline depending on B-axis rotation

Due to the gravity-induced deformation of B-axis, axis average line of C-axis could be tilted or drifted in radial direction when B rotates. The change in position and orientation of C-axis centerline depending on B-axis rotation are respectively modeled as follows:

$$\begin{cases} \delta x_{CB}(B_i) = a_1 \cos(\zeta)\left(\dfrac{|B_i| - |B|_{\min}}{|B|_{\max} - |B|_{\min}}\right) \\ \delta y_{CB}(B_i) = a_1 \sin(\zeta)\left(\dfrac{|B_i| - |B|_{\min}}{|B|_{\max} - |B|_{\min}}\right) \end{cases} \tag{6-8}$$

$$\begin{cases} \alpha_{CB}(B_i) = a_1 \cos(\zeta)\left(\dfrac{|B_i| - |B|_{\min}}{|B|_{\max} - |B|_{\min}}\right) \\ \beta_{CB}(B_i) = a_1 \sin(\zeta)\left(\dfrac{|B_i| - |B|_{\min}}{|B|_{\max} - |B|_{\min}}\right) \end{cases} \tag{6-9}$$

where a_1 is given by a_1=N(10 μm, 3.3 μm) for Eq. (6-8), and a_1=N(0.01°, 0.0033°) for Eq. (6-9), respectively. ζ is given by ζ= U(0°, 360°). This model

assumes error motions of C-axis increased proportionally as B rotates from $|B|_{min}$ to $|B|_{max}$, as is shown in Fig. 6-5. Note that $|B|_{min}$ and $|B|_{max}$ are respectively set to be minimum and maximum of absolute value of B-axis rotation angle. In our simulation, for case (a) (φ=15°, ψ=30°), $|B|_{min}$ and $|B|_{max}$ are set to be 15° and 45°, respectively. The simulation results are shown in Table 6-6.

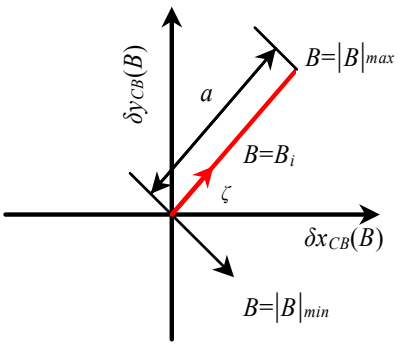

Fig. 6-5 Modeling of change in position of C-axis depending on B-axis rotation ($\delta x_{CB}(B)$ and $\delta y_{CB}(B)$).

Table 6-6 Influence of change in position and orientation of C-axis depending on B-axis rotation

Contributor		Parameter setting (a_2)	Circularity error (μm)			
			φ=15°, ψ=30°		φ=75°, ψ=30°	
			mean	std	mean	sd
Change in position of C-axis depending on B-axis	$\delta x_{CB}(B)$ and $\delta y_{CB}(B)$	N (10 μm, 3.3 μm)	1.5	0.6	3.8	1.6
Change in orientation of C-axis depending on B-axis	$\alpha_{CB}(B)$ and $\beta_{CB}(B)$	N (0.01°, 0.0033°)	2.0	1.1	12.5	5.4

6.5.10 Periodic pure radial error motion and tilt error motion of C-axis depending on B-axis rotation

The simulation results conducted in Sections 6.5.7 and 6.5.8 show that periodic pure radial error motion and tilt error motion of C-axis have negligibly small influence on circularity. This section considers the case where these error motions of C-axis increase as B rotates from $|B|_{min}$ to $|B|_{max}$, as is shown in Fig.

6-6. This error, caused typically by the gravity-induced deformation, is often the case in practice (see Section 6.6). Periodic pure radial error motion of C-axis depending on B-axis rotation is modeled as follows:

$$\begin{cases} \delta x_{CB}(C_i, B_i) = a_2 \cos(C_i + \zeta)\left(\dfrac{|B_i| - |B|_{\min}}{|B|_{\max} - |B|_{\min}}\right) \\ \delta y_{CB}(C_i, B_i) = a_2 \sin(C_i + \zeta)\left(\dfrac{|B_i| - |B|_{\min}}{|B|_{\max} - |B|_{\min}}\right) \end{cases} \tag{6-10}$$

where a_2 and ζ are given by a_2=N(10 μm, 3.3 μm) and ζ= U(0°, 360°).

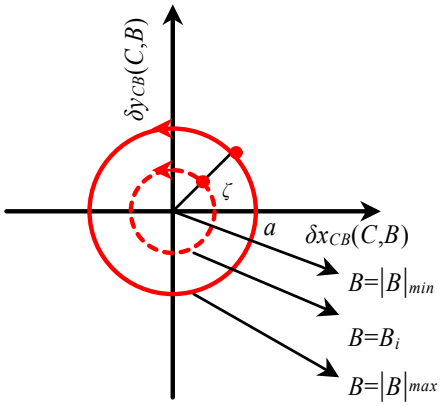

Fig. 6-6 Modeling of radial error motion of C-axis depending on B-axis rotation ($\delta x_{CB}(B,C)$ and $\delta y_{CB}(B,C)$).

Table 6-7 Influence of periodic pure radial error motion and tilt error motion of C-axis depending on B-axis rotation

Contributor		Parameter setting (a_2)	Circularity error (μm)			
			φ=15°, ψ=30°		φ=75°, ψ=30°	
			mean	standard deviation	mean	standard deviation
Periodic pure radial error motion of C-axis depending on B-axis	$\delta x_{CB}(B,C)$ and $\delta y_{CB}(B,C)$	N (10 μm, 3.3 μm)	5.0	1.7	3	1.7
Periodic tilt error motion of C-axis depending on B-axis	$\alpha_{CB}(B,C)$ and $\beta_{CB}(B,C)$	N (0.01°, 0.0033°)	16.5	6.1	10	7.3

Periodic tilt error motion of C-axis depending on B-axis rotation, is simulated in the same way as in Eq. (6-10), while a_2 is given by N(0.01°,

0.0033°). The simulation results are shown in Table 6-7. Compared with Sections 6.5.7 and 6.5.8, circularity error of cone frustum is more sensitive to periodic pure radial error motion and tilt error motion of C-axis when they increase with B rotation.

6.5.11 Summary of analysis

Tables 6-3 to 6-7 show the sensitivity of the circularity of cone frustum test piece, to position-dependent geometric errors, representing typical low-frequency error motions of a rotary axis. Many observations can be made from these simulation results. For example, some position-dependent geometric errors such as linear error motion of B-axis to Z direction, periodic pure radial error motion and conical tilt error motion of C-axis, have a negligibly small influence on circularity of cone frustum. However, periodic pure radial error motion and tilt error motion of C-axis enlarged with B rotation could be critical factors for cone frustum machining test.

It has been shown in Section 6.3 or [Matsushita, 2008] that a center offset of a rotary axis, one of position-independent geometric errors, has a significant influence on the circularity error of machined workpiece. In typical machine setup by an operator, the location of C-axis rotation center line is measured with B = 0°. When the C-axis rotation center line is moved as the B-axis rotates from B = 0°, typically due to the gravity influence, the present simulation shows that such an error may cause a large circularity error. Analogous observation can be made for pure radial and tilt error motions of C-axis.

6.6 Experimental case study

6.6.1 Objective

Based on the error analysis presented in previous sections, this section demonstrates an experimental case study to find out a critical error factor in a cone frustum machining test.

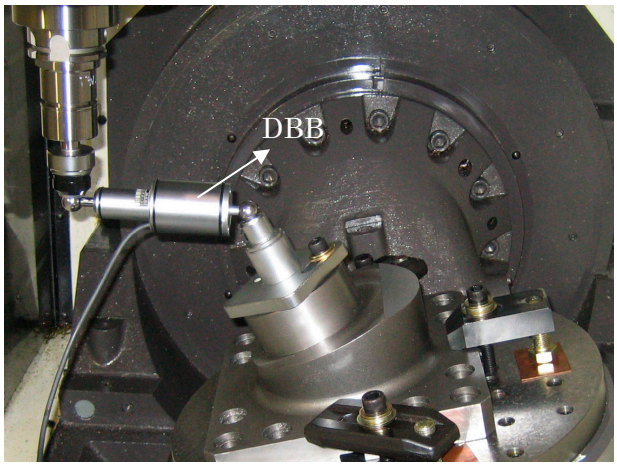

Fig. 6-7 Setup of the ball bar measurement.

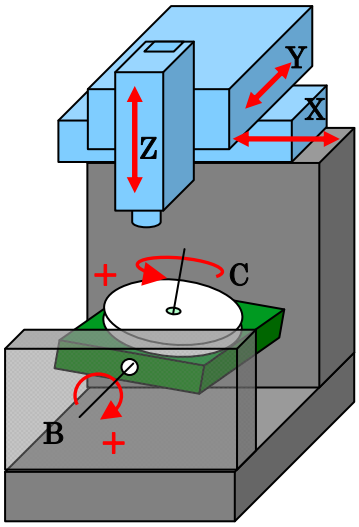

Fig. 6-8 Experimental five-axis machine tool.

Instead of actual machining test, a contouring error profile was measured with the same CL (cutter location) trajectory as in a cone frustum machining test by a ball bar measurement [Ihara, 2005]. Fig. 6-7 shows the setup of ball bar measurement. The configuration of the experimental five-axis machine tool is shown in Fig. 6-8. Note that the experimental machine tool studied here is different from the one used in Chapter 3 to 5. Test conditions are summarized in Table 6-1. Only the case with the tilt angle φ=15° and the half-apex angle ψ=30° was tested. The ball bar nominal length is 150 mm, and the feedrate in the workpiece coordinate system is 1,000 mm/min. Fig. 6-9 shows contour error profiles for the cone frustum CL trajectory measured by ball bar measurement.

The circularity error is 12.4 μm for clockwise (CW) rotation, and 9.2 μm for counter-clockwise (CCW) rotation.

The objective of this section is to demonstrate an experimental investigation of major error causes of the observed contour error profile.

6.6.2 Influences of position-independent geometric errors

First, position-independent geometric errors, shown in Table 2-3 in Section 2.2.1.2, were experimentally identified by using a set of ball bar measurements presented by Tsutsumi and Saito [Tsutsumi, 2003]. Then, their influence is simulated as has been presented in Section 6.4. The identified position-independent geometric errors are shown in Table 6-8. Since the rotation center of rotary axes were carefully identified at B=0° before a cone frustum measurement, δx^0_{BY}, δy^0_{BY}, δz^0_{BY} are assumed to be zero in this simulation.

Fig. 6-9(a) also shows a simulated error trajectory to show the influence of identified position-independent geometric errors. It can be observed that the influence of geometric errors shown in Table 6-8 is quite small; the circularity error of the simulated error trajectory is only 0.3 μm. This indicates that position-independent geometric errors of this machine are tuned sufficiently small in its mechanical assembly. From our experiences, such a case is often observed in the latest small-sized five-axis machining centers.

Table 6-8 Identified position-independent geometric errors associated with rotary axes

Location error	Identified value	Location error	Identified value
δx^0_{BY}(μm)	-	α^0_{BY}(°)	0.0005
δy^0_{BY}(μm)	-	β^0_{BY}(°)	0.0001
δz^0_{BY}(μm)	-	γ^0_{BY}(°)	0.0001
δx^0_{CB}(μm)	2.1	α^0_{CB}(°)	-0.0006

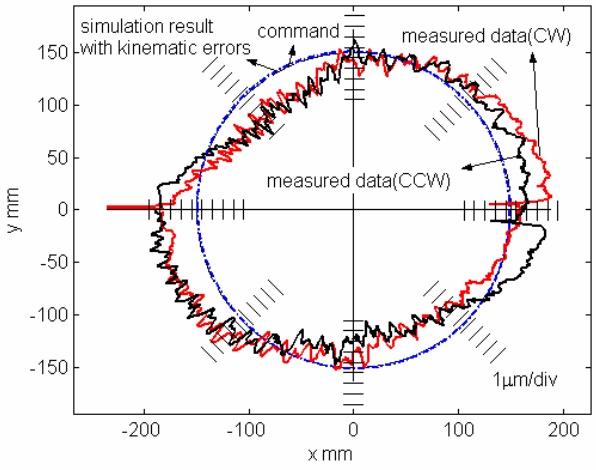

(a) Influence of position-independent geometric errors

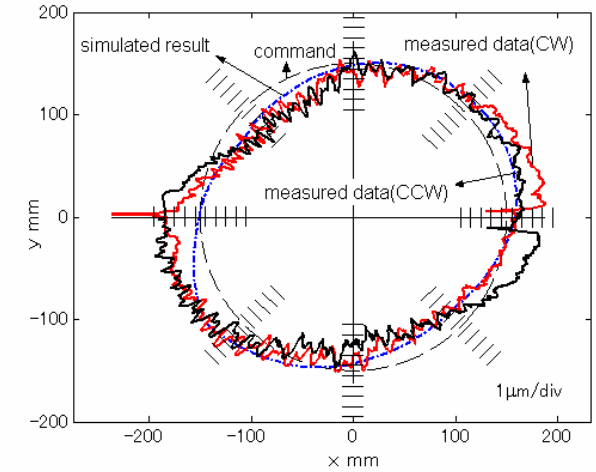

(b) Influence of position-dependent geometric errors of C-axis

Fig. 6-9 Contour error profiles for the cone frustum CL trajectory measured by ball bar measurement.

6.6.3 Influences of major position-dependent geometric errors

Then, a major contributor for this circularity error must be found. This and the following subsections present the application of the R-test to diagnose error motions of rotary axes that have potentially larger influence on this circularity error. In this study, we used the contact-type R-test presented in Section 2.1 (although the R-test device used in this chapter is not exactly the same as the one used in Chapters 3 and 4, it is essentially the same with similar fixture and same displacement sensors). The R-test measurement procedure presented in Section 3.3 was performed on this machine tool (as shown in Figs. 6-7 and 6-8). Since it

is the repetition of measurement and analysis procedure presented in Chapter 3, the detailed measurement result is not presented here. As the conclusion, from R-test measurements, following observations were made on position-dependent geometric errors of the experimental machine:

- Angular positioning error of B-axis ($\beta_{BY}(B)$) is negligibly small at B=0°, but gets larger as B gets larger or smaller; it becomes -0.0010° at B=90° and 0.0013° at B=-90°. Within -90°≤B≤0° or 0°≤B≤90°, $\beta_{BY}(B)$ increases or decreases approximately linearly.
- Angular positioning error of C-axis ($\gamma_{CB}(C, B)$) is sufficiently small compared to B-axis at any C (C=0°, 30°, …, 330°) and any B (B=-90°, -60°, …, 90°).
- Due to the gravity-induced deformation, the table is displaced to –Z direction as B gets closer to ±90°. The displacement to –Z direction ($\delta z_{BY}(B)$) is about 10.0 μm at B=±90°.
- The periodic tilt error motion of C-axis ($\alpha_{CB}(B,C)$, $\beta_{CB}(B,C)$) is negligibly small at B=0°. It gets, however, larger as B gets larger or smaller; it becomes as large as 0.005° at B=±90°. This is also caused by the gravity-induced deformation.

Based on the error analysis presented in previous sections, it can be seen that most of position-dependent geometric errors above do not impose significant influence on the circularity error of the cone frustum test piece. For example, since the B-axis rotates between B=-15° and -45° in the cone frustum tool path (see Fig. 6-2(a)), its angular positioning error in this range is about 0.001° at most. Based on Table 6-3 (Section 6.5.2), its influence on the circularity error can be estimated much smaller than 1 μm, which is negligibly small. Similarly, the angular positioning error of C-axis, and the gravity-induced deformation to –Z direction, as shown above, impose only negligibly small influence on the circularity error.

6.6.4 Measurement of error motion of C-axis and its influences

Error analysis presented in Section 6.5.9 (Table 6-7) suggests that the enlargement of the periodic radial error motion and tilt error motion of C-axis depending on B-axis position can be a potentially critical error factor for the circularity error (see Section 6.5.9 for further details). This section will present a part of R-test results to observe how error motions of C-axis rotation changes for different B-axis positions, since it is potentially a critical error factor for cone frustum machining tests.

The R-test measurement cycle presented in Section 3.3 was performed. For every 30 degree of C-axis rotation, the displacement of the ball is measured by using the R-test device. The same measurement was repeated for B=0°, -30°, and -60°. Note that in the CL trajectory shown in Fig.6-2 (a), the B-axis varies from -15° to -45°.

Unlike the analysis procedure in Section 3.3 (where measured R-test profiles are converted to the reference coordinate system), we convert measured R-test profiles to the B-axis coordinate system (see Section 2.3.1.2-(2) for its definition) to more clearly observe the shift of C-axis at different B angles. Figures 6-10(a) to (c) show measured position errors of the ball with the C-axis rotation. An error of measured position ("○" marks) from its command position ("●" marks) is magnified 10,000 times.

From Fig. 6-10(a), it can be observed that the error is sufficiently small at B=0°. In Fig. 6-10(b) and (c), the center of the error trajectory is significantly shifted to –X direction. This is mostly due to the miscalibration of the B-axis rotation center in the Z-direction, i.e. $\delta^0 z_{BY}$. In addition, more importantly, it can be observed that the diameter of the error trajectory becomes larger as the B-angle increases. This suggests that the periodic radial error motion (or tilt error motion) of C-axis getting larger as the B-angle increases (see Fig. 3-4).

The influence of such an error on the contour error in the cone frustum test is then simulated by using the five-axis kinematic model (see Section 2.3.1.2 for more details). Since the main focus of this analysis is on the influence of C-axis shift, the influence of position-independent geometric errors identified as shown

in Table 6-8 is removed from the measured R-test trajectories. Then, the position error shown in Fig. 6-10(a) to (c) is stored in a look-up table for each B- and C-axis position. For each point on the given cone frustum CL trajectory, the position error of rotary table is calculated by interpolating this look-up table. Fig. 6-9(b) shows the simulated contour error profile. Measured profiles are the same as those in Fig. 6-9(a). The simulated trajectory matches well with the measured trajectory. The circularity error of the simulated trajectory is 4.9 μm. It indicates that the enlargement of periodic pure radial error motion (or tilt error motion) of C-axis enlarged by B-axis position, as can be observed in Fig. 6-10(a) to (c), are major causes of contour error in cone frustum machining in this particular case.

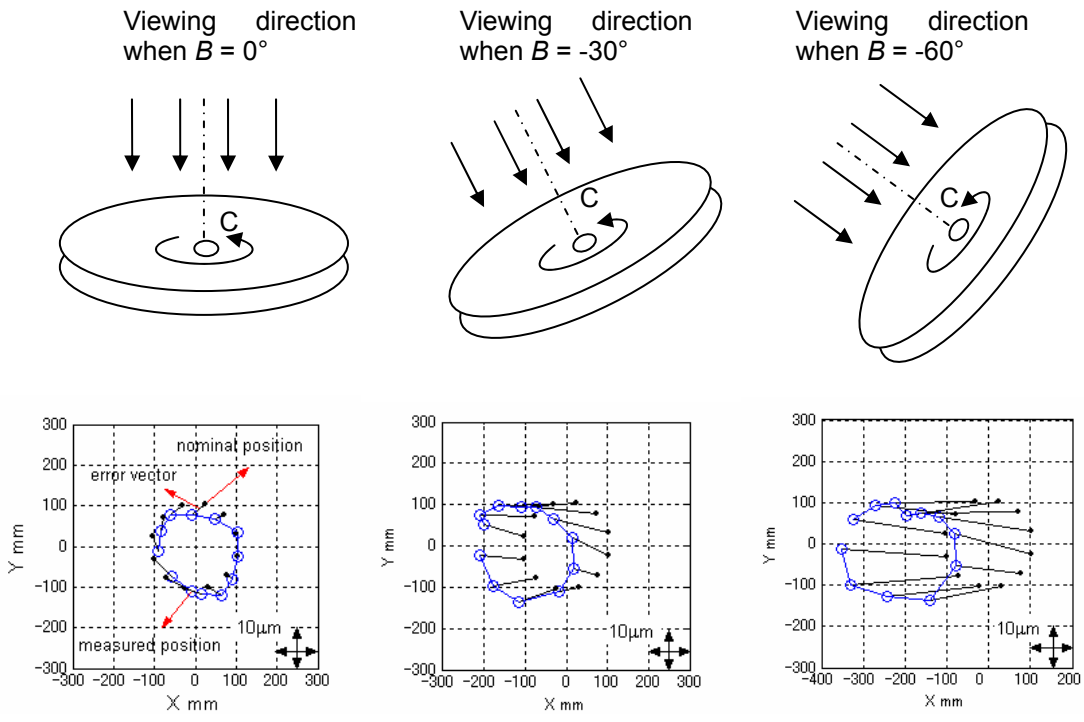

(a) $B = 0^{\circ}$ (b) $B = -30^{\circ}$ (c) $B = -60^{\circ}$

Fig. 6-10 Motion error profile of C-axis in different rotation angle of B-axis in the B-coordinate system.

6.7 Conclusion

Although a five-axis machine tool has many potential error sources related to its rotary axes, some of them impose a significant influence on a cone frustum machining test, while others have only negligibly small influence on it. This

section presented the sensitivity analysis of the circularity of the machined cone frustum test piece to major error motions. The sensitivity of each error to the circularity of test piece is computed by using statistic simulations.

The present analysis results show that:

(1) The influence of the gravity-induced deformation of a rotary axis to -Z direction, and the periodic pure radial error motion or periodic conical tilt error motion of C-axis with constant amplitude, has relatively small influence on the circularity of test piece.

(2) The enlargement of periodic pure radial error motion and periodic tilt error motion, caused by the gravity influence, can be a potentially critical error factor for cone frustum machining test.

(3) The case $\varphi>\psi$ (φ=75°, ψ=30°), the circularity of cone frustum is more sensitive to error motions, such as angular positioning error of a rotary axis, and the periodic pure radial error motion or periodic conical tilt error motion of B- axis.

Based on present error sensitivity studies, the experimental case study demonstrated the measurement of the change in error motion of C-axis depending on the B-axis position by using the R-test. The enlargement of periodic pure radial error motion (or tilt error motion) of C-axis, were clearly observed, and it was verified by simulation that they are dominant error causes for the circularity error in a cone frustum test.

The cone frustum machining test is just an example of machining applications. Analogous error sensitivity analysis methodology presented in this chapter can be straightforwardly applied to any machining applications in general.

Chapter 7
Conclusions

For many latest commercial small-sized five-axis machine tools, observation and calibration of *position-dependent geometric errors*, or component errors in ISO 230-7 [ISO 230-7, 2006] becomes important to understand *how error motion changes with the rotation of a rotary axis*. However, most of the researches in the literature focused only on calibration of location errors (i.e. position-independent geometric errors), which represents only "average" position and orientation of an axis of rotation.

Therefore, in this thesis, an indirect measurement method to calibrate geometric errors (particularly position-dependent geometric errors) of multiple rotary axes on five-axis machine tools was proposed. The conclusions and main contributions in each chapter are as follows:

1) In Chapter 3, a new algorithm to analyze a profile of sphere displacement measured by the R-test to numerically calibrate error motions of two rotary axes at various angular positions was proposed. While the R-test device itself was proposed in the previous work [Weikert, 2004], original contributions of this chapter is as follows:
    a. An intuitive, graphical presentation method of R-test measurements to understand how error motions of rotary table changes in three-dimensional space depending on the swiveling angle was proposed.
    b. A scheme to separate squareness errors of linear axes by performing a set of R-test measurement cycles with different sphere positions was proposed, assuming that squareness errors of linear axes are the dominant error factors in the linear axes.
    c. Identification method of position-dependent geometric errors of a rotary axis by static R-test was presented.
2) In Chapter 4, a method to calibrate thermally induced geometric errors of the

rotary was proposed. Unlike conventional thermal tests described in ISO 230-3 [ISO 230-3, 2007], where only thermal influence on positioning accuracy is evaluated, the presented thermal test clarified how error motions of the rotary table change with the reciprocating movements of B-axis. It is the application of the R-test analysis methodology presented in Chapter 3 to thermal tests. In the experimental demonstration, the proposed R-test cycle clarified that the temperature rise of B-shaft mainly caused a gradual position shift of C-axis average line in Y-direction.

3) In Chapter 5, a non-contact R-test by using laser displacement sensors, particularly for dynamic measurement on five-axis machine tools, was proposed.
    a. The measurement accuracy of four laser displacement sensors with different measuring principles was experimentally investigated for profile measurement of a sphere surface. The performance of the four laser displacement sensors in the application to the non-contact R-test was studied. As a result, specular reflection type laser displacement sensor (LK-G10 from Keyence) was selected as the sensors for the developed non-contact R-test prototype.
    b. A new algorithm was proposed to estimate the three-dimensional displacement of sphere center by using a non-contact type R-test with laser displacement sensors. It shows that the algorithm should consider the measurement uncertainty caused by the inclination of the target surface.
    c. The measuring performance of the developed non-contact R-test was investigated compared with the contact-type R-test. Experimental comparison showed that: 1) in the static measurement to calibrate an error map of rotary axes, measurement results showed a good agreement between both R-test devices. Both of them exhibited good repeatability; 2) in the dynamic measurement to observe synchronous error of a rotary axis (C-axis) and linear axes (XY-axes), different result was obtained in the tangential direction to the C-axis rotation. Possibly,

the dynamics of the contact-type R-test may be an error factor, while its exact cause should be clarified in the future.

d. The prototype non-contact R-test device developed in this chapter is subjected to high-frequency noise of the amplitude about 2 μm due to the speckle noise in laser beam. When a laser displacement sensor of different measuring principle (e.g. the spectral interference type laser displacement sensor, studied in this chapter) is used, this noise may be significantly reduced, although the measurable range may become smaller.

4) In Chapter 6, a methodology to quantitatively evaluate the sensitivity of various error motions of rotary axes on the geometric accuracy of the machined workpiece was proposed. As an illustrating example, the statistical analysis of the cone frustum machining test is presented. The sensitivity of typical error motions of rotary axes to the circularity of test piece is computed by using Monte Carlo simulations. In this particular application example to cone frustum machining tests, based on the analysis methodology presented in this chapter, critical error motions for the circularity of the machined cone frustum workpiece are clarified as follows:

(1) The influence of the gravity-induced deformation of a rotary axis to -Z direction, and the periodic pure radial error motion or periodic conical tilt error motion of C-axis with constant amplitude, has relatively small influence on the circularity of test piece.

(2) The enlargement of periodic pure radial error motion and periodic tilt error motion, caused by the gravity influence, can be a potentially critical error factor for cone frustum machining test.

(3) Based on presented error sensitivity studies, the experimental case study demonstrated the application of the R-test to observe the change in error motion of C-axis depending on the B-axis position. The enlargement of periodic pure radial error motion (or tilt error motion) of C-axis, were clearly observed, and it was verified by simulation that

they are dominant error causes for the circularity error in a cone frustum test.

This thesis focused on the application of the R-test to observe geometric errors caused by the error sources of kinematic errors, thermal errors, and dynamic errors depending on velocity. For the future work, the non-contact R-test for dynamic measurement of synchronous error of rotary and linear axes must be improved.

Acknowledgements

I would like to express my deepest and sincere thanks to my supervisor, Associate Professor Soichi Ibaraki and Professor Atsushi Matsubara, Department of Micro Engineering, Kyoto University, for their constant and invaluable guidance, and continuous assistance throughout the entire research work, as well as the indispensable comments for this thesis.

I am grateful for the indispensable helps, especially from Dr. Yamaji and Mr. Koike, during the construction of the contact-type R-test device and the non-contact R-test device. I am really thankful to Assistant Professor Dr. Kono, Dr. Yamaji, Mr. Fujita, and Mr. Koike for their indispensable helps in experimental techniques.

Special thanks to Keyence Co. Ltd. for renting the four laser displacement sensors used in Chapter 5.

My deepest appreciation goes to the MONBUKAGAKUSHO: MEXT (Ministry of Education, Culture, Sports, Science, and Technology), Japan, for the Japanese Government Scholarship.

I would like to express my gratitude to all the members of the servo research meeting for their invaluable comments for this research.

I am thankful to all the members of the Machining, Measurement, and Control Laboratory for the events and moments during my 3.5 years' study in Kyoto University.

Finally, I would like to express my thanks to my dear son and wife, my family, as well as my friends for their continuous supporting.

Reference

[Abbaszaheh-Mir, 2002] Y. Abbaszaheh-Mir, J. R. R. Mayer, G. Clotier, C. Fortin, Theory and simulation for the identification of the link geometric errors for a five-axis machine tool using a telescoping magnetic ball-bar, International Journal of Production Research, 40-18: pp.4781-4797, 2002.

[Bossoni, 2007] S. Bossoni, and J. Cupic, Test piece for simultaneous 5-axis machining. Laser metrology and machine performance VIII, pp. 24-33, 2007.

[Bringmann, 2006] B. Bringmann, W. Knapp, Model-based 'Chase-the-Ball' calibration of a 5-axis machining center, Annals of the CIRP, 55-1, pp.531-534, 2006.

[Bringmann, 2007] B. Bringmann, Improving geometric calibration methods for multi-axes machining centers by examining error interdependencies effects, 2-664, Fortschritt-Berichte VDI, Dűsseldorf, 2007.

[Bringmann, 2009] B. Bringmann, W. Knapp, Machine tool calibration: Geometric test uncertainty depends on machine tool performance, Precision Engineering, 33, pp.524-529, 2009.

[Dasssanayake, 2007] M. Dasssanayake, M. Tsutsumi, K. Higashiyama, and K. Yamamoto, An approach to estimate the inherent deviations by means of simultaneous five-axis motion, Proc. of the 4th Int'l Conf. on Leading Edge Manufacturing in 21st Century (LEM21), pp.423-428, 2007.

[Erkan, 2010] T. Erkan and J. R. R. Mayer, A cluster analysis applied to volumetric errors of five-axis machine tools obtained by probing an uncalibrated artefact, CIRP Annals - Manufacturing Technology, 59-1, pp. 539-542, 2010.

[Erkan, 2011] T. Erkan, J. R. R. Mayer, and Y. Dupont, Volumetric distortion assessment of a five-axis machine by probing a 3D reconfigurable uncalibrated master ball artefact, Precision Engineering, 35, pp.116-125, 2011.

[Fidia] Fidia: http://www.fidia.it.

[Hayashi, 2005] T. Hayashi, X. Liu, Y. Kiyoshi, K. Yamazaki, and M. Mori, Laser-CCD Based Measurement System for Angular Motion of Integrated Machine Tools, in Proc. of Int'l Conf. on Leading Edge Manufacturing in 21st century (LEM21), pp. 85-90, 2005.

[Heidenhain] www.heidenhain.co.jp.

[Hong, 2011] C. Hong, S. Ibaraki, and A. Matsubara, Influence of position-dependent geometric errors of rotary axes on a machining test of cone frustum by five-axis machine tools, Precision Engineering, 35-1, pp. 1-11, 2011.

[Ibaraki, 2009] S. Ibaraki, C. Oyama, H. Otsubo, Measurement and compensation of motion errors on 5-axis machine tool by R-test (First report) - Procedure of R-test measurement and identification of geometric errors on 5-axis machine tool, Proceedings of the 2009 Fall JSPE semiannual meeting, pp. 843–844, 2009.

[Ibaraki(1), 2010] S. Ibaraki, M. Sawada, A. Matsubara, and T. Matsushita, Machining tests to identify kinematic errors on five-axis machine tools, Precision Engineering, 34-3, pp. 387-398, 2010.

[Ibaraki(2), 2010] S. Ibaraki, Y. Kakino, T. Akai, N. Takayama, I. Yamaji, and K. Ogawa, Identification of Motion Error Sources on Five-axis Machine Tools by Ball-bar Measurements (1st Report) - Classification of Motion Error Components and Development of the Modified Ball Bar Device (DBB5), J. of the Japan Society for Precision Engineering, 76-3, pp.333-337, 2010. (in Japanese)

[Ibaraki, 2011] S. Ibarali, C. Oyama, H. Otsubo, Construction of an error map of rotary axes on a five-axis machining center by static R-test, Int. J. of Machine Tools and Manufacture, 51, pp.190-200, 2011.

[Ibaraki, 2012] S. Ibaraki and W.Knapp, Indirect Measurement of Volumetric Accuracy for Three-axis and Five-axis Machine Tools: A Review, to appear in International Journal of Automation Technology, 6-2, 2012.

[IBS] IBS Precision Engineering: http://www.ibspe.com.

[Ihara, 2005] Y. Ihara, K. Tanaka, Ball bar measurement equivalent to cone frustum cutting on multi-axis machine: comparison of ball bar measurement with cutting test on spindle-tilt type 5-axis MC. J Jpn Soc Prec Eng. 71-12, pp.1553-1557, 2005 (in Japanese)

[Inasaki, 1997] I. Inasaki, K. Kishinami, S. Sakamoto, N. Sugimura, Y. Takeuchi, F. Tanaka, Shaper generation theory of machine tools -- its basis and applications, Yokendo, Tokyo, 1997. (in Japanese)

[Iritani, 2010] T. Iritani, S. Ibaraki, and T. Matsushita, Error calibration for 5-axis controlled machine tools based on on-machine geometric measurement of artifact, Proc. of the 2010 Spring JSPE Semiannual Meeting, pp.1023-1024, 2010. (in Japanese)

[ISO 230-1, 1996] ISO 230-1, Test code for machine tools -- Part 1: Geometric accuracy of machines operating under no-load or finishing conditions, 1996.

[ISO/FDIS 230-1, 2011] ISO/FDIS 230-1:2011, Test code for machine tools -- Part 1: Geometric accuracy of machines operating under no-load or quasi-static conditions, 2011.

[ISO 230-2, 2006] ISO 230-2, Test code for machine tools -- Part 2: Determination of accuracy and repeatability of positioning numerically controlled axes, 2006.

[ISO 230-3, 2007] ISO 230-3, Test code for machine tools -- Part 2: Determination of thermal effects, 2007.

[ISO 230-4, 2005] ISO 230-4, Test code for machine tools -- Part 4: Circular tests for numerically controlled machine tools, 2005.

[ISO 230-7, 2006] ISO 230-7, Test code for machine tools -- Part 7: Geometric accuracy of axes of rotation, 2006.

[ISO/CD 10701-7, 2011] ISO/CD 10701-7:2011, Test conditions for machining centres - Part 7: Accuracy of a finished test piece, 2011.

[ISO 10791-1, 1998] ISO 10791-1, Test conditions for machining centres -- Part 1: Geometric tests for machines with horizontal spindle and with accessory heads (horizontal Z-axis), 1998.

[ISO/CD 10791-6, 2011] ISO/CD 10791-6.2:2010, Test Conditions for Machining Centers -- Part 6: Accuracy of Speeds and Interpolations, 2010.

[ISO 10360-3, 2000] ISO 10360-3:2000, Geometrical Product Specifications (GPS) - Acceptance and reverification tests for coordinate measuring machines (CMM) -- Part 3: CMMs with the axis of a rotary table as the fourth axis, 2000.

[JCGM 100, 2008] JCGM 100: 2008, Evaluation of measurement data - Guide to the expression of uncertainty in measurement (GUM), 2008.

[Kakino, 1993] Y. Kakino, Y. Ihara, and A. Shinohara, Accuracy Inspection of NC Machine Tools by Double Ball Bar Method, Hanser Publishers, 1993.

[Kakino, 1994] Y. Kakino, Y. Ihara, H. Sato, and H. Otsubo, A Study on the motion accuracy of NC machine tools (7th report) - Measurement of motion accuracy of 5-axis machine by DBB tests, J. of Japan Society for Precision Engineering, 60-5, pp.718-723, 1994. (in Japanese)

[Keyence] Keyence: http://www.keyence.co.jp.

[Khan, 2010] A. W. Khan and W. Chen, A methodology for systematic geometric error compensation in five-axis machine tools, International Journal of Advanced Manufacturing Technology, 53-5/8, pp. 615-628, 2010.

[Kimura, 2011] Y. Kimura, A. Matsubara, Y. Koike, Analysis of Measurement Errors of a Diffuse-Reflection-Type Laser Displacement Sensor for Profile Measurement, to be presented at the 6th Int. Conf. on Leading Edge Manufacturing in 21st Century (LEM21), 2011.

[Kohama, 2008] A. Kohama, R. Mori, S. Komai, M. Suzuki, S. Aoyagi, J. Fujioka, and Y.Kamiya, Calibration of kinematic parameters of a robot using neural networks by a laser tracking system, Proc. of 7th Int'l Conf. on Machine Automation, pp.251-256, 2008.

[Lau, 1986] K. Lau, R. Hocken, and W. Haight, Automatic laser tracking interferometer system for robot metrology, Precision Engineering, 8-1, pp. 3-8, 1986.

[Lee, 2009] D. Lee, Z. Zhu, K. Lee, S. Yang. Identification and Measurement of

Geometric Error of 5-axis Machine Tool with Tilting Head using Double Ball Bar. In: the 3rd International Conference of Asian Society for Precision Engineering and Nanotechnology, 2009.

[Lei, 2002] W. T. Lei and Y. Y. Hsu, Accuracy test of five-axis CNC machine tool with 3D probe-ball. Part II: errors estimation, Int'l J. of Machine Tools and Manufacture, 42-10, pp. 1163-1170, 2002.

[Lei, 2007] W. Lei, M. Sung, W. Liu, and Y. Chuang, Double ballbar test for the rotary axes of five-axis CNC machine tools, Int'l J. of Machine Tools and Manufacture, 47-2, pp. 273-285, 2007.

[Li, 2003] Z. Li, Y. Kakino, A. Kawashima, Y. Ihara, I. Yamaji, and M. Wakizaka, Diagnosis of Motion Errors of the Rotary Axes in 5-axis Machining Center (1st Report) - The Procedure for Diagnosis of Angular Error Sources, J. of the Japan Society for Precision Engineering, 69-5, pp.703-709, 2003. (in Japanese)

[Mahbubur, 1997] R. M. Mahbubur, J. Heikkala, K. Lappalainen, and J. A. Karjalainen, Positioning accuracy improvement in five-axis milling by post processing, Int'l J. of Machine Tools and Manufacture, 37-2, pp. 223-236, 1997.

[Matano, 2007] K. Matano, Y. Ihara, Ball bar measurement of five-axis conical movement, In: Laser Metrology and Machine Performance VIII, 2007.

[Matlab, 2002] Matlab, User's Guide: Optimization Toolbox for Use with Matlab, 2002.

[Matsushita, 2008] T. Matsushita, T. Oki, A. Matsubara, The accuracy of cone frustum machined by five-axis machine tool with tilting table, J. of the Japan Society for Precision Engineering, 74-6, pp.632-636, 2008. (in Japanese)

[Matsushita, 2010] T. Matsushita and T. Oki, Identification of Geometric Errors in Five-axis Controlled Machine Tool with Touch Trigger Probe, Proc. of the 2010 Spring JSPE Semiannual meeting, pp.1105-1106, 2010. (in Japanese)

[Matsushita, 2011] T. Matsushita and A. Matsubara, Identification and

compensation of geometric errors in five-axis machine tools with a tilting rotary table using conic trajectories measured by double ball bar, J. of the Japan Society for Precision Engineering, 77-6, pp.594-598, 2011. (in Japanese)

[Mori Seiki] Mori Seiki: www.moriseiki.com.

[NAS 979, 1969] NAS 979, Uniform cutting test - NAS series. Metal cutting equipments, 1969.

[Oyama, 2009] C. Oyama, S. Ibaraki, H. Otsubo, Measurement and compensation of motion errors on 5-axis machine tool by R-test (Second report) - Identification and compensation of component errors on rotary axes, Proceedings of the 2009 Fall JSPE semiannual meeting, pp.845–846, 2009.

[Ramesh, 2000] R. Ramesh, M.A. Mannan, A.N. Poo, “Error Compensation in Machine Tools -- a Review Part II: Thermal Errors”, Int. J. of Machine Tools and Manufacture, 40, pp.1257-1284, 2000.

[Renishaw] www.renishaw.jp.

[Sakamoto, 1997] S. Sakamoto, I. Inasaki, H. Tsukamoto and T. Ichikizaki, Identication of alignment errors in five-axis machining centers using telescoping ballbar, Trans. of the Japan Society of Mechanical Engineers (C), 63-605, pp.262-267, 1997. (in Japanese)

[Sartori, 1995] S. Sartori and G. Zhang, Geometric Error Measurement and Compensation of Machines, CIRP Annals: Manufacturing Technology, 44-2, pp.599-609, 1995.

[Schwenke, 2005] H. Schwenke, M. Franke, J. Hannaford, and H. Kunzmann, Error mapping of CMMs and machine tools by a single tracking interferometer, CIRP Annals - Manufacturing Technology, 54-1, pp. 475-478, 2005.

[Schwenke, 2008] H. Schwenke, W. Knapp, et al., Geometric Error Measurement and Compensation of Machines --An Update, Annals of the CIRP, 57-2, pp.560-575, 2008.

[Schwenke, 2009] H. Schwenke, R. Schmitt, P. Jatzkowski, and C. Warmann,

On-the-fly calibration of linear and rotary axes of machine tools and CMMs using a tracking interferometer, CIRP Annals - Manufacturing Technology, 58-1, pp. 477-480, 2009.

[Seshagiri, 2000] S. Seshagiri, H.K. Khalil, Output Feedback Control of Nonlinear Systems Using RBF Neural Networks, IEEE Transaction on Neural Network, 11-1, pp.69-79, 2000.

[Slamini, 2010] M. Slamini, J.R.R. Mayer, M. Balazinski, S.H.H. Zargarbashi, S. Engin, C. Lartigue, Dynamic and geometric error assessment of an XYC axis subset on five-axis high-speed machine tools using programmed end point constraint measurements, International Journal of Advanced Manufacturing Technology, 50, pp.1063-1073, 2010.

[Slocum, 1992] AH. Slocum, Precision Machine Design. Englewood Cliffs: Prentice-Hall, 1992.

[Soons, 1992] J.A.Soons, F.C.Theuws, P.H.Schllekens, Modeling the errors of multi-axis machines: a general methodology, PrecisionEngineering, 14-1, pp.5–19, 1992.

[Srivastava, 1995] A.K. Srivastava, S.C. Veldhuis, M.A. Elbestawit, “Modeling Geometric and Thermal Errors in a Five-axis CNC Machine Tool”, Int. J. of Machine Tools and Manufacture, 35-9, pp.1321-1337, 1995.

[Takatsuji, 1999] T. Takatsuji, M. Goto, S. Osawa, R. Yin, and T. Kurosawa, Whole-viewing-angle cat’s eye retroreflector as a target of laser trackers, Measurement Science and Technology, 10-7, pp.87-90, 1999.

[Takeuchi, 2010] K. Takeuchi, S. Ibaraki, T. Yano, T. Takatsuji, S. Osawa, and O. Sato, Estimation of Three-dimensional Volumetric Errors of Numerically Controlled Machine Tools by a Laser Tracker, Proc. of 14th International Conference on Mechatronics Technology (ICMT2010), pp. 3-7, 2010.

[Tsutsumi, 2003] M. Tsutsumi, A. Saito, Identification and compensation of systematic deviations particular to 5-axis machining centers, International Journal of Machine Tools and Manufacture, 43, pp.771-780, 2003.

[Tsutsumi, 2004] M. Tsutsumi and A. Saito, Identification of angular and

positional deviations inherent to 5-axis machining centers with a tilting-rotary table by simultaneous four-axis control movements, Int'l J. of Machine Tools and Manufacture, 44-12/13, pp. 1333-1342, 2004.

[Tsutsumi, 2008] M. Tsutsumi, Y. Ihara, A. Saito, N. Mishima, S. Ibaraki, M. Yamamoto, M. Kobayashi, T. Yonetani, Standardization of testing methods for kinematic motion of five-axis machining centers -- Draft proposal for ISO standard, In: Proceedings of the 7th Manufacturing and Machine Tool Conference, pp 95-96, 2008. (in Japanese)

[Uddin, 2009] M. S. Uddin, S. Ibaraki, A. Matsubara, and T. Matsushita, Prediction and compensation of machining geometric errors of five-axis machining centers with kinematic errors, Precision Engineering, 33-2, pp. 194-201, 2009.

[US Patent, 2007] US Patent, US 7278222, Method for measuring a program-controlled machine tool, 2007.

[Veldhuis, 1995] S. C. Veldhuis and M. A. Elbestawi, A Strategy for the Compensation of Errors in Five-Axis Machining, CIRP Annals - Manufacturing Technology, 44-1, pp.373-377, 1995.

[Weikert, 2004] S. Weikert, R-Test, a New Device for Accuracy Measurements on Five Axis Machine Tools, Annals of the CIRP, 53-1, pp.429-432, 2004.

[Yamamoto(1), 2011] T. Yamamoto, T. Hasebe, and M. Tsutsumi, Development of testing method for five-axis machining centers by thin groove cutting, J. of the Japan Society for Precision Engineering, 77-4, pp.405-410, 2011. (in Japanese)

[Yamamoto(2), 2011] T. Yamamoto, T. Hasebe, and M. Tsutsumi, Development of five-axis machining center geometric errors estimation method by thin groove cutting, J. of the Japan Society for Precision Engineering, 77-8, pp.776-780, 2011. (in Japanese)

[Yamamoto(3), 2011] T. Yamamoto and M. Tsutsumi, Determination of axis of rotation of rotary table for five-axis machining centers, J. of the Japan Society for Precision Engineering, 77-3, pp.301-305, 2011. (in Japanese)

[Yano, 2006] T. Yano, T. Takatsuji, S. Osawa, T. Suzuki, Y. Motomura, and T.

Itabe, Development of a Small Two Axis Spherical Motor Type Laser Tracker with Submicron Measurement Accuracy, IEEJ Trans. on Sensors and Micromachines, 126-4, pp.144-149, 2006. (in Japanese)

[Yumiza, 2007] D. Yumiza, S. Yoshinobu, M. Tsutsumi, K. Utsumi, and Y. Ihara, Measurement method for motion accuracies of 5-axis machining centers (2nd report) - influence of geometric deviations on finished cone frustums, Proc. of 2007 JSPE Spring Annual Conf., pp.191-192, 2007. (in Japanese)

[Zargarbashi, 2006] S. Zargarbashi and J. Mayer, Assessment of machine tool trunnion axis motion error, using magnetic double ball bar, Int'l J. of Machine Tools and Manufacture, 46-14, pp. 1823-1834, Nov. 2006.

[Zargarbashi, 2009] S.H.H. Zargarbashi, J.R.R. Mayer, Single Setup Estimation of a Five-axis Machine Tool Eight Link Errors by Programmed End Point Constraint and On-the-fly Measurement with Capball Sensor, International Journal of Machine Tools and Manufacture, 49-10, pp.759-766, 2009.